A PARAMETRIC FINITE ELEMENT ANALYSIS STUDY OF A LAB-SCALE ELECTROMAGNETIC LAUNCHER

A Thesis
Presented to
The Academic Faculty

by

Edward Sun Kimn

In Partial Fulfillment
of the Requirements for the Degree
Master of Science in the
School of Mechanical Engineering

Georgia Institute of Technology
May 2011

A PARAMETRIC FINITE ELEMENT ANALYSIS STUDY OF A LAB-SCALE ELECTROMAGNETIC LAUNCHER

Approved by:

Dr. Itzhak Green, Advisor
School of Mechanical Engineering
Georgia Institute of Technology

Dr. Scott Bair
School of Mechanical Engineering
Georgia Institute of Technology

Dr. Richard S. Cowan
Manufacturing Research Center
Georgia Institute of Technology

Dr. Richard W. Neu
Mechanical Engineering
Georgia Institute of Technology

Date Approved: January 20, 2011

ACKNOWLEDGEMENTS

I would like to thank Dr. Itzhak Green and Dr. Richard Cowan for their continued guidance and leadership throughout my study and work. I would also like to thank my fellow researchers and graduate students who helped support my work.

Finally, I would like to thank my parents, my brother, and my friends for their moral support during this time.

This research is supported in part through the Department of Defense Multidisciplinary Research Program of the University Research Initiative as Office of Naval Research Grant N00014-04-1-0601, entitled "Friction & Wear under Very High Electromagnetic Stress." Dr. P. Peter Schmidt serves as Program Officer. Information conveyed in this thesis does not necessarily reflect the position or policy of the Government, and no official endorsement should be inferred.

TABLE OF CONTENTS

LIST OF TABLES

Page

LIST OF FIGURES

Page

LIST OF SYMBOLS AND ABBREVIATIONS

A	Contact area
$\vec{B}$	Magnetic field
E	Modulus of elasticity
$\vec{E}$	Electric field
$\vec{F}$	Force
P_c	Contact pressure
T	Temperature
k	Thermal conductivity
q	Electric charge of the particle
t	Time
$\vec{v}$	Instantaneous velocity
η	Heat partition
μ	Coefficient of friction

EMAG	Electromagnetic
EML	Electromagnetic Launcher
FEA	Finite Element Analysis

SUMMARY

An electromagnetic launcher (EML) accelerates an armature up to several kilometers per second using the electromagnetic (EMAG) forces created by high electrical currents. Specifically, a large current is passed through a copper rail which travels through the aluminum armature into another copper rail, thus completing the circuit. This high current creates a magnetic field around the rails and the armature. That magnetic field has a Lorentz force associated with it, which accelerates the armature.

In the use of the EML, several different trends affect the performance of the EML. The structural and thermal aspects of the system are analyzed to better understand the effects of each on the performance of the EML. The motivation of this work is to better understand the variables that may improve the useful life of the rails through modifications of the armature to reduce melt-wear and arcing. Melt-wear occurs when the armature reaches its melting temperature as it slide through the rails and the resulting melted material bonds to the rails. That bonded material reduces the useful life of the rails and degrades the EML performance.

In order to better understand the factors that affect melt-wear and arcing, the armature design, compliance layer, and armature materials are varied. All variations are explained further below. The resulting changes in the structural, thermal, and electromagnetic analyses help us better understand melt-wear and arcing. The analyses were performed using a finite element analysis (FEA) program. The geometric change made was to reduce the taper in the armature leg from approximately 1.0° to approximately 0.5°. The taper is used to create a wedge between the two rails while still allowing the armature to be propelled. The materials are varied in every analysis to see the effects of each material's properties on the resulting analyses. All analyses were performed uncoupled in order to view the factors individually. By varying the parameters in the simulation, a better understanding of the factors affecting melt wear can be better understood.

A 2-D structural analysis is used to determine the structural deformation, contact area, contact pressure, and von Mises stress that occur during the initial contact of the

armature to the rail. Also modeled and varied, was a compliance layer which is an artificial structural layer that accounts for the deformation differences between the modeled parts versus the actual manufactured parts that exists in the lab-scale EML which is in the Laboratory for Extreme Tribology.

An electromagnetic analysis was performed to determine the EMAG forces that result from the electric field. The 3-D EMAG analysis assumed a perfect contact between the rail and the armature and was a quasi-static analysis. The analysis was performed with two armature materials (aluminum and molybdenum) and with both designs (original and modified). A current curve versus time used in the lab-scale launcher was applied to the EMAG model.

The contact results from the structural analysis are applied to the thermal analysis. The thermal analysis consists of two parts, the frictional heating and the Joule heating. Frictional heating occurs when the armature slides and the two surfaces sliding against each other generates heat. Joule heating occurs from the high current used in the launching and the resistance of the materials. To compare the materials, the coefficient of friction was held constant and the heat partition was based on theoretical speeds of the different material armatures. An onset velocity for melting was estimated in order to compare the materials and models to each other. For Joule heating, the same current load used in the lab-scale launcher was applied to the model with specific contact conductance values.

The final analysis performed was the 3-D modal analysis which determined the mode shapes and period of the armature designs and different material armatures. The modal analysis is necessary because it can help determine if on-off contact might occur during launching. On-off contact can cause arcing which creates crater imperfections in the rail, thus reducing its useful life. Both, a stressed and pre-stressed model, are analyzed because the armature is under a stressed state when placed in between the two copper rails.

For the structural analysis, at the lab-scale interference the von Mises stress in both of the aluminum armature designs and the copper rails do not reach the yield strength of the weaker material, aluminum. In order to compare the materials to each other, a baseline was created which was to find the interference where the maximum

contact pressure occurred. Based on this criterion, and the structural analysis results, the contact areas and pressures were found and applied in the thermal analysis.

For the EMAG analysis, because the current load is given and the material resistivity is not high, the total EMAG forces resulting from the electric field did not vary. Therefore, the only results that could be obtained from this analysis was the theoretical duration of time it would take for the armature to exit the launcher. The acceleration found from the EMAG analysis was integrated to find the velocity and integrated again to find the displacement with respect to time.

The thermal results show that because of the very high current, melting occurs almost immediately. However, based on the estimated melting velocities, the choice of material of the armature should be the tungsten modified (reduced taper) design with a harder compliance layer because it allows higher velocities before melting. Also, apparent in the results and from previous studies, the Joule heating is the more prominent factor in the melting of the armature than frictional heating.

From the modal analysis and the calculated exit times, the armature has a possibility for on-off contact with the rails. This means that arcing can occur.

Summarizing, the purpose of this research was to develop a tool to better understand how varying parameters affect the different aspects of the EML. This tool allows the user to relatively quickly vary parameters such as material properties or armature geometry.

CHAPTER 1: INTRODUCTION

The electromagnetic launcher (EML) is a technological development that allows an armature to travel along rails without using a combustible element. It uses an electric power source to generate a high electromagnetic (EMAG) force propelling the armature up to several kilometers per second. The schematic diagram and principles behind the EML are shown in Figure 1.

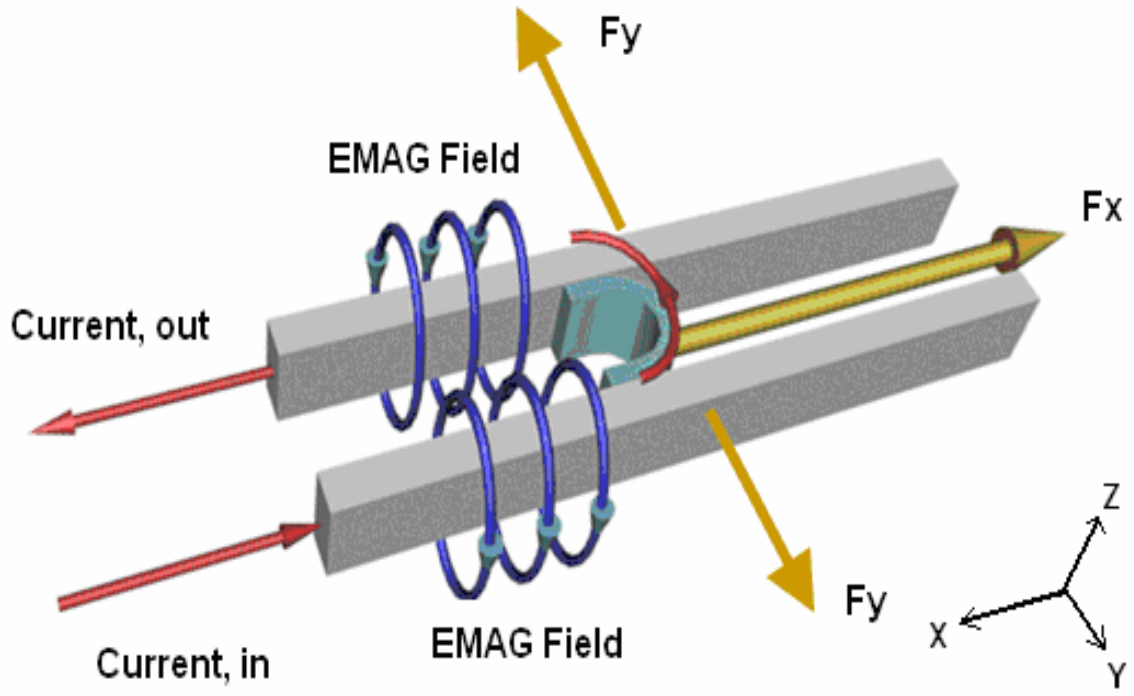

Figure 1. Schematic diagram and principles of an electromagnetic launcher

As seen in Figure 1, the current enters in the negative x-direction into the lower rail, travels through the armature between the rails, and out the other rail in the positive x-direction. The high current creates an EMAG field around the rails. That EMAG field coupled with the current generates the EMAG force to drive out the armature at high velocities in the negative x-direction. The rails are pushed away from each other according to the EMAG forces in the y-direction but are limited by the structure of the

EML apparatus (not shown in Figure 1). The armature is generally a C-shaped design allowing the legs of the armature to be separated by the EMAG forces in the y-direction. The separation of the legs is desired because it helps the armature maintain contact with the rails.

A common occurrence in the EML is melting of the rails due to the high currents and velocities. The high current generates a lot of heat which causes melting at the interface between the armature and rails. Melting of the armature can result in loss of material which can reduce contact. It can also leave molten pieces on the rail which reduces the useful life of the rails. However, molten material is a potential lubricant between the rail and armature.

The significance of using an EML is the potential advancement in weaponry. Current projectiles use combustible elements to propel them, but with EMLs, that need for a potentially volatile fuel is eliminated. The major downfall to an EML is the energy required to propel the armature to high velocities. In the lab-scale EML at the Extreme Tribology Research Facilties at the Georgia Institute of Technology, the capacitors are capable of generating several kilo-Joules of energy to launch the armature. The EML used there is shown in Figure 2.

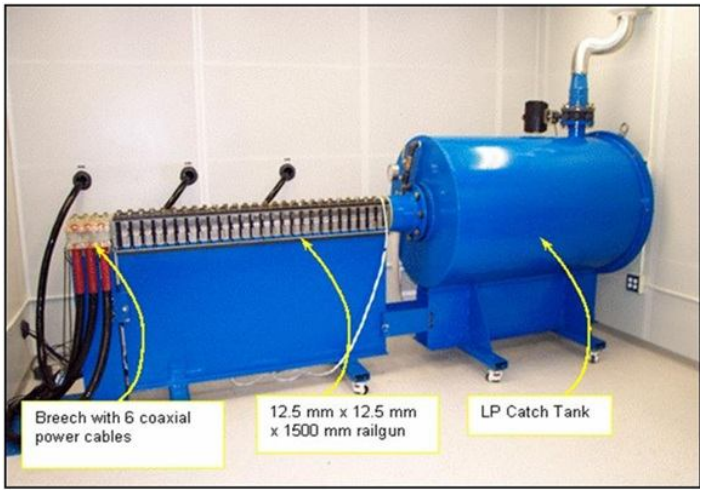

Figure 2. Picture of the lab-scale EML at the Georgia Institute of Technology

Due to the EML technology being a fairly recent development, research is being conducted to make the process more efficient. A lot of the research revolves around the melting of the armature and rails. As stated before, with melting, pieces of the armature can weld itself to the rails which reduces the useful life of the rails. Due to the very high forces involved, the armature can accelerate to very high speeds very quickly. This high acceleration means that the armature exits the barrel of the EML very quickly. Due to the fast exit speed and the necessity to maintain contact, research has been conducted on the modal aspects of the armatures used in EMLs.

A diagram of the cross-section of the lab-scale EML is shown in Figure 3. The dimensions of the barrel for the armature are approximately 12.5W x 12.5H x 1500L mm. Currently, for the lab-scale EML, the armature material used is aluminum 6061 T-6. The rails are made of copper C110 and stretch the length of the barrel. Encasing the EML are thin steel plates stacked vertically side by side. The steel plates are bolted from top to bottom to keep the armature encased in the barrel. Between the rails and the steel encasement, are two different types of insulators. There is a G10 insulator and then a thin sheet of Mylar insulator between the copper rails and the steel casing. At the end of the barrel is the catch tank for launched armatures. Outside of the EML chamber is the high capacity pulse discharge power supply (PDPS). The PSDS supplies electric current through the wall using six coaxial cables attached to six different power supply modules. Each module is capable of storing up to 13.5 kJ and dispersing them according to the user.

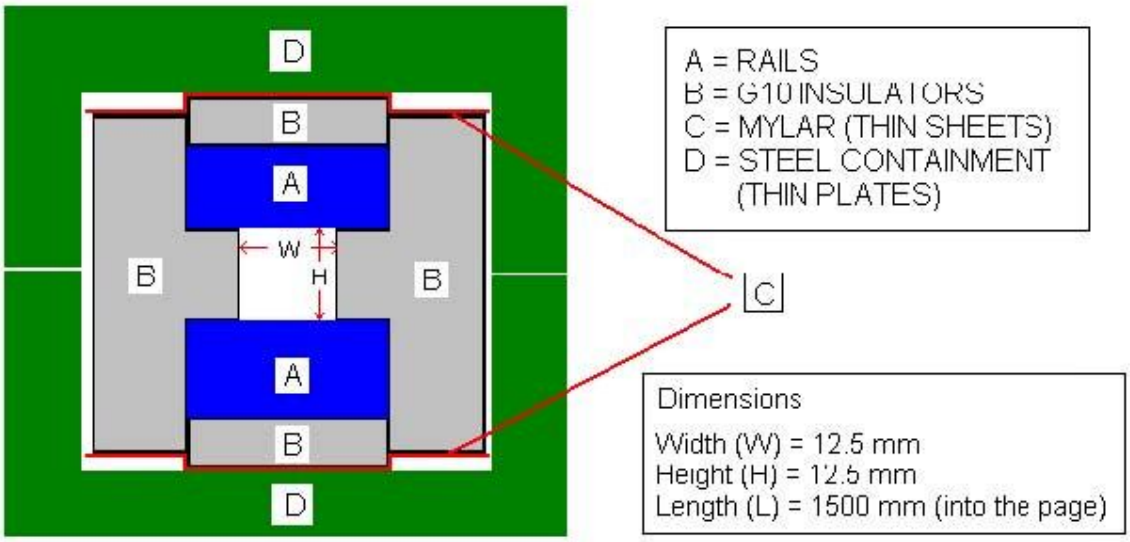

Figure 3. Diagram of the cross-section of the lab-scale EML

The study conducted in this work is theoretical based using finite element analysis (FEA) and the lab-scale EML. The study consists of four sections with each section analyzing different parameters to better understand factors of melting. The four sections are shown in Figure 4. The structural analysis revolves around the initial loading and interference fit of the armature between the rails. It also provides load data for the thermal analysis and modal analysis. The EMAG analysis focuses on the EMAG forces that result from the current load used for the lab-scale EML. The thermal analysis is a study of the friction heating from the high velocities obtained from the EML and the heat generated by the high current used, also referred to as Joule heating. The final focus of this work is the modal analysis which determines whether intermittent contact is a possibility as the armature is launched.

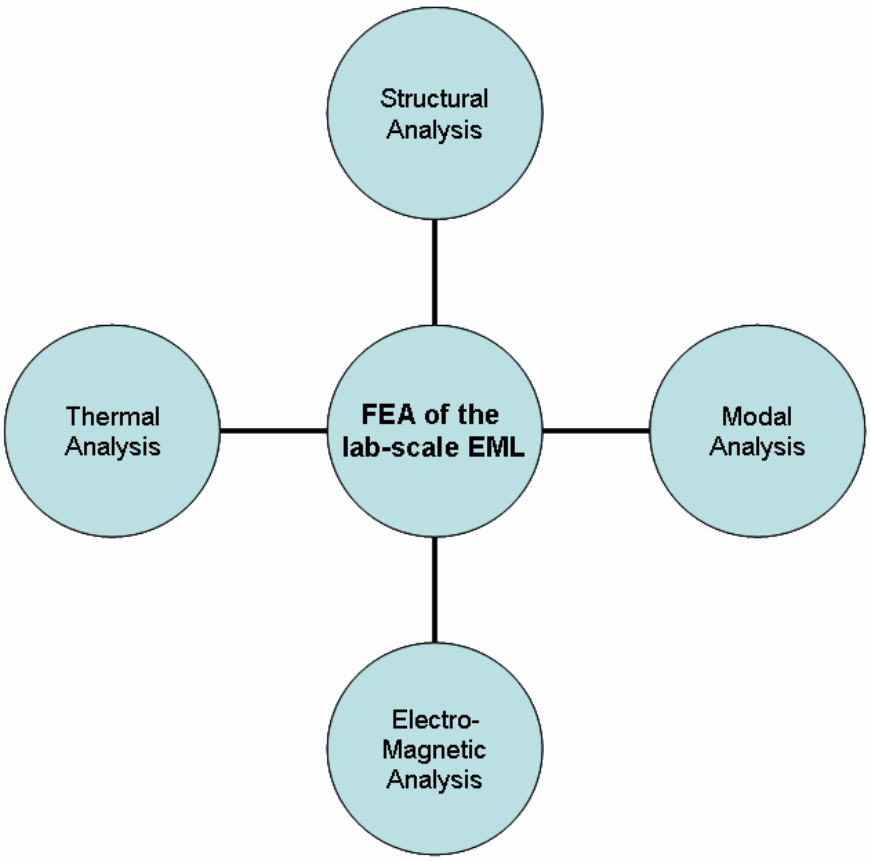

Figure 4. Different sections included in the FEA study

For all the analyses, none of them were coupled due to computational hardware limitations and the complexity of the problem. Realistically, each analysis should be coupled because each aspect involves the other. The amount of structural loading affects the amount of friction between the armature and rail, while the EMAG analysis also provides forces that are unaccounted for in the structural analysis. Also, the armature is under a load from the structural and EMAG portion which affects the modal analysis. As melting occurs, material is removed or is not capable of load bearing, which would affect all three of the other analyses. However, since coupling all four analyses would be computationally time intensive and complex, the analyses were uncoupled and loads were based on the structural analysis of initial contact between the rail and armature.

The purpose of the study was not to couple the analyses together but to help understand factors that have a role in melting. Optimally, having no armature material remain on the rails would be desired because it means the effective life of the rails is lengthened. While reduction of melt-wear is desired, the effectiveness of the EML should not be sacrificed as well. Therefore, while some materials have a high melt temperature, it may also be a denser material which would slow the armature's flight which is undesired. The parameters varied in this study were armature designs, compliance layers, and armature materials.

This study first presents a literature review regarding previous research on existing EMLs and relevant fields of study. Chapter 3 presents the structural analysis of the initial contact between the rail and armature. The structural analysis is completed for two designs, two compliance layers and six different armature materials. Vital information for the following analyses, such as contact pressure and contact length, are presented in the structural portion. The next chapter provides the EMAG analysis of a stationary armature for both designs and two different armature materials. The reason for the limited studies is explained later. Using the loading conditions from the structural analysis, the thermal analysis is conducted in Chapter 5. The thermal analysis consists of a friction study followed by a Joule heating study. The friction heating study is a formulaic estimation, while the Joule heating study is FEA based. The friction heating analysis calculates a potential obtainable speed before melting occurs from friction alone. The Joule heating analysis calculates a thermal-electric temperature from the current into the rails. Both analyses are completed for each parametric variation. The final study is the modal analysis, presented in Chapter 6. This study analyzes an unstressed armature as well as a pre-stressed model based on the data from the structural loads. Again, this study considers all parametric variations. The final chapter is a presentation of the conclusions obtained from the study as well as potential future work.

CHAPTER 2: LITERATURE REVIEW

Many investigations of the EML have been conducted because of its potential contributions and advancement to future technology. Suggestions for use have ranged from space launchers to weaponry. Bolonkin and Krinker [1] propose a theory to build a method and facility to deliver payloads and people to outer space using an EML. The estimation is that it can launch objects at a cost of $3-$5/lb. Wetz et al. [2] also proposed a space launch that would need to be >1000 m long and capable of generating an acceleration >1000 G. Therefore, the launcher would only be able to propel objects capable of withstanding those forces.

Most focus has been on utilizing the launcher as a projectile weapon. Because there are many attributes that affect the performance, there is a wide scope of research. Since the focus of this study was an investigation of parameters that affect the useful life of the rails, previous studies on these aspects is presented in this section. Many studies have been conducted to better understand factors affecting EML performance. From their studies, the most prominent issue is the high current creating high temperatures. The high temperatures cause several problems with respect to structural loading and material loss. Since molten material cannot support any loads, the armature legs can lose contact with the rails thus causing arcing. The material loss usually ends with current crowding at the contact and molten material bonding to the rails.

Because the current is so important, many of the studies revolve around the high current used and the interaction between the armature and rail at the contact interface. The high current creates important effects at the contact interface between the armature rails. Merrill and Stefani [3] developed a one-dimensional stationary conductor model to better understand the melt-wave erosion wear from a stationary point. A melt-wave is the localized front of molten material that erodes around the perimeter of armature contact area. Their study found an expression for the velocity of the melt-wave front. From their

study, it was found that the moving melt-wave boundary had an insignificant effect on the melt-wave erosion in solid armature railguns. Stefani and Parker [4] conducted experiments to measure the wear in aluminum armatures and the conditions for wear. Their experiments found that at relatively low velocities (<1km/s) friction wear was small compared to Joule heating wear. They also confirmed that the melt-wave started around the perimeter of the contact and moved to the center. Watt and Stefani [5] wanted to confirm the theory that the melt wave erosion was proportional to velocity and to the square of current. By conducting a series of tests, they confirmed that the erosion rates were in reasonable agreement with the scaling relations. However, qualitatively, they found that the location of peak erosion depth was independent of current and velocity.

Angeli and Cardelli [6] conducted research of electro-thermal behavior of solid armatures in an EML. Their model showed that primary and secondary current paths would be the most common travel paths for the applied current. Drobyshevskii et al. [7] found that arc discharges occur due to large quantities of small heated particles, droplets, and vapor ejected from the armature in the railgun bore. The ejections from the armature are due to the high current generating melting temperatures in the armature. The ejections cause current crowding to occur which increases the temperature at those locations. Dutta et al. [8] also confirmed that Joule heating caused aluminum deposition on the rails. They conducted an experiment on a static setup by placing aluminum around quartz and contacting the aluminum with copper strips. From their results, they found that the aluminum would melt from the current and then travel along the negative rail.

Using computational models, He and Ovaert [9] studied the heat partition for sliding contacts. As surfaces slide across each other, the heat is partitioned between the two surfaces and depends on several factors. Their study concluded that the formulae used in their calculations agreed with their experimental data. They also concluded that to reduce maximum temperature in the contact area, either the velocity should be limited or choose a material with a high specific heat and/or thermal conductivity. Chen et al. [10]

found, through experimental studies, that the main cause of melting was due to the current crowding in the contact interface. Also, they found that electrical contact conductance was more important than thermal contact conductance. These parameters are values that simulate imperfect contact in FEA for electrical and thermal conductivity.

Regarding geometry changes to improve wear conditions, Rip et al. [11] modified the currently used C-shaped armature. The created a saddle shaped armature that helped change the peak current density location. It moved the location from the outer edge to the center. Also by introducing a leading leg to the C-shaped armature, they reduced the maximum temperature from Joule heating. Satapathy et al. [12] conducted further studies on the saddle shaped armature with a leading leg. This study used experimental data to justify the claims of the previous paper. Through experimental data, the claims were supported. The leading leg is expected to help reduce current arcing, which is when the current jumps a gap between two materials.

A study by James [13] proposes using a supported armature to help maintain contact pressure. Maintaining contact is the key to the EML and because molten material cannot support a load, the armature can lose contact with the rail. Therefore, the proposal was to use a supported multiple contact armature concept. James [14] also proposed a hybrid armature that would be mainly aluminum alloy but use a higher temperature low erosion rate metal for the contact surfaces.

Other studies to understand wear mechanics have involved using a lubricant at the contact interface. Merrill and Stefani [15] modeled melt-lubricant as turbulent flow. Their model was just to focus on mechanical wear and use melted armature material as a lubricant. They compared their model results with experimental results and found that there were differences in mechanical wear and speed not explained by their model. Ghassemi and Barsi [16] conducted an analysis on a new armature design and a liquid film used as lubrication. They used a liquid film of indium to not only improve electrical conductivity between the armature and rail, but also delay friction melting. However,

their redesign of the armature did not improve the maximum temperature locations. Another study by Singer et al. [17] used a solid lubricating interfacial compound (SLIC) to condition the rails and armature. For the EML, which was a low-speed launcher (100-140 m/s), the lubrication showed promise as it reduced armature damage and armature/rail arcing. It also improved launch reliability and increased projectile speed. Watt et al. [18] have found a consistent problem with damage to the copper rails close to the starting area of the armature. By observing the rails after extended use, damage occurred in the form of axial grooves along the path of the armature. The damage would start near the starting position of the armature and extended 30-100 cm. They also observed that the damage had a current threshold of 1 MA, while at currents of 1.4-1.7 MA, damage would occur. From the observations, it was hypothesized that the damage occurred from mechanical or chemical erosion and not from arcing or plasma because the groove damage did not display characteristics of melted copper and aluminum mixing together.

Another smaller, but still important focus, is on the vibration of the armature. Because contact is the most important key to the launching of a projectile, vibration or chatter is extremely undesirable. Watt and Fish [19] surmised that chatter was responsible for deformations in the rails. As the armature was launched, it was observed that chatter lines would appear in the rails. They believed that the lines would most likely appear from two sources: asperities plastically deforming as they slid past each other and the mode shape of the armature as it launched.

Due to the complexity of the EML, FEA is used to understand the different aspects involved (structural, thermal, EMAG, and modal). The largest problem that occurs with using FEA and the complexity of the EML, is the coupling of each field. Typically, many assumptions have to be made or a study has to focus on only a couple key points of the EML. As more research is conducted, the desire is to have a coupled analysis to view the affects each field has on the other. Hopkins et al. [20] study the

electrical and structural behavior of a C-shaped armature using FEA. They used a commercial EMAP3D program to analyze the electromagnetics and, the proprietary code used in DYNA3D to solve the dynamic response of the EML using the results from the EMAP3D simulation. Their simulation was limited to just armature behavior or armature/rail interaction at startup, but found the stresses and displacements of the armature and rail at startup and while applying a current to the rails. Newill et al. [21] also completed a coupled analysis going from a 2-D electromagnetics solution to a 3-D dynamic structural solution. They used the electromagnetic forces obtained from their 2-D analysis and applied it as a load in a 3-D structural analysis. The data from the electromagnetic analysis had to be extracted and assumptions were made as it was applied to the structural analysis. Liu and Lewis [22] modeled an electromagnetic transient analysis using an EMAP3D simulation. Their results also confirmed the locations of concentrated current densities.

Stankevich and Shvetsov [23] conducted an analysis to better understand the correlation between Joule heating and the armature shape. Their analyses were done using 2-D and 3-D FEA simulations. They concluded that the least wear would occur if the contact interface could be increased. Also, their simulations showed that the 2-D simulations closely matched their 3-D simulations. A parametric FEA study by Powell and Zielinski [24] focused on the heat generation in a double-taper sabot-armature. Their simulations found that temperatures would increase at the throat region of the armature, or the joining point of the armature legs, if the radius decreased due to electrical conduction around a convex region.

Watt and Bryant [25] used experimental data and FEA codes, EMAP3D and DYNA3D, to analyze the stresses generated at the throat region of the armature. Their simulations calculated stresses generated by magnetic forces, inertial loading, wear, and thermal expansions. The simulations provided evidence that thermal stresses were as

important as magnetic stresses for low-speed armatures. In addition to their FEA calculation, their experimental data supported their simulations.

Expanding on contact conditions and resistivity, Hsieh et al. [26] analyzed pressure-dependent contact resistivity using two types of models in EMAP3D. Their results showed that higher temperatures occur where higher current densities occur. Also, the effects of initial contact pressure distribution are overshadowed by the forces from the EMAG field increase. Merrill et al. [27] modeled the magnetic repulsive forces for armature contact to better understand the transition to arcing. They created 3-D models to analyze the repulsive contact forces resulting from perimeter erosion. The concern in the paper was that as the melt wave propagated inwards along the perimeter of the contact area, the current became more and more dense. As a result, repulsive magnetic forces were generated which resulted in unloading, or magnetic blowoff. Their simulations found that magnetic blowoff occurred when there was a loss of 98% of the contact area which did not occur in recovered armatures. Therefore, their results suggested that magnetic blowoff was not a result of the perimeter melt wave erosion.

The previous thesis written by Chung [28] covered an uncoupled FEA study of the lab-scale EML. This thesis is an extension of that study by using the core of Chung's analysis and applying new parameters. The purpose is to obtain a better understanding of the parameters that may affect melt-wear due to the use of the EML. As observed in other works, the largest challenge is to eliminate or delay arcing contact. To accomplish this, melt-wave erosion and current crowding needs to be addressed. Typically, as shown in other studies, both aspects can be addressed by examining the contact interface.

Chung's structural analysis took into account a compliance layer obtained from one set of data, while this paper analyzes the possibility of difference stiffness compliance layers. The different compliance layer data is taken from experimental data of different EMLs. The data is the analyzed to create lower and upper bound compliance layer values. Also, his structural analysis checked one design of the armature and one

material. In this work, two designs and six materials are analyzed to find contact pressures, forces, and stresses. The two designs are analyzed using both compliance layers and six different materials for armatures.

For the EMAG analysis, the work is similar, but this study analyzes two designs and all the materials for the armature. Using the forces from the EMAG analyses, armature speeds and distances traveled are estimated based on an experimental current load. By simulating the EMAG forces, the different speeds and travel distances can be estimated for each material armature to determine the most kinetically efficient material.

Chung estimated a friction heating analysis by displacing the armature over time. In this work, the friction heating analysis is completed by estimating velocities at which melting is expected to occur from friction alone. Because previous studies showed that Joule heating was the more important factor, more focus was placed on the Joule heating analyses. The Joule heating analysis is the same as Chung's except more scenarios are analyzed in this work, specifically, conditions obtained from the structural analysis for each material, compliance layer, and design.

For the modal analysis, an unstressed and pre-stressed armature is modeled, as it was in Chung's. However, the different scenarios obtained from the structural analysis are also applied to the pre-stressed models. The modal analysis provides insight on whether intermittent contact is possible.

As it was in Chung's work, these simulations are uncoupled from each other. Also, temperature dependent properties are not included. However, it should be noted that the purpose of this paper is not to create exact real world results, but to better understand the parameters affecting melt-wear.

CHAPTER 3: STRUCTURAL ANALYSIS

The initial armature-to-rail contact for the lab-scale EML is obtained by an interference fit as shown in Figure 5.

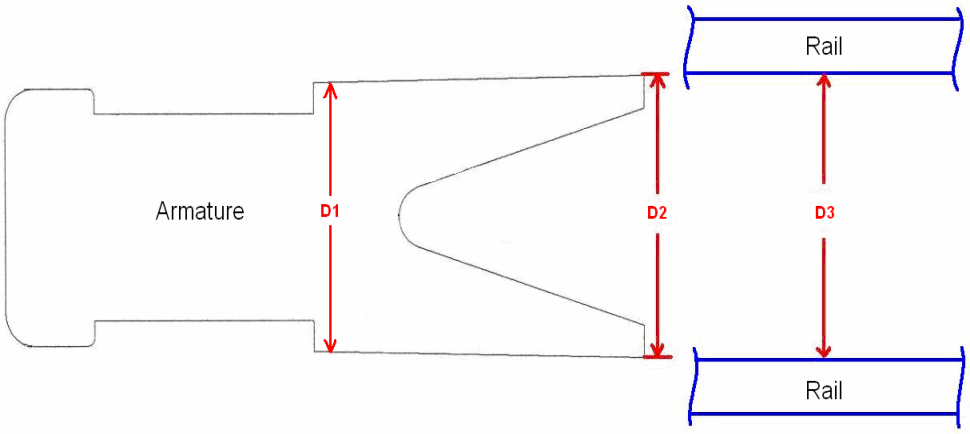

Figure 5. Schematic diagram of the armature and the rails

The dimension D2 is larger than D1 thus creating a taper to allow placement of the armature between the rails by pushing the armature into the rail opening at a dimension of D3, where D1<D3<D2. Because of the interference fit (D1<D2), the armature legs deform creating the contact area between the armature legs and the rails. In this portion of the analysis, a 2-D structural FEA of the lab-scale EML is performed to obtain certain aspects of the contact. The analysis results that were obtained or estimated were the initial contact area, the von Mises stresses in the rail and armature, the contact pressure, and the deformation shape of the armature given the interference used in the lab-scale EML. The von Mises stresses are important for material yielding and to maintain structural rigidity. Rail-to-armature contact is affected by the contact pressure and deformation shape.

Due to the symmetry of the setup, only half of the system was modeled in the FEA and therefore only half of the interference (i.e., ~0.12 mm instead of 0.25 mm) is applied and referred to as the half-interference for the rest of the chapter. Two designs on

the current armature are considered for this analysis. The first design is the original design and the second is a design where the D1 dimension is increased to reduce the angle of the inclination on the leg. The structural analysis is completed for the two different designs of the armature using aluminum as the material to compare the two models to each other.

The materials are then compared to each other using the different designs and a standard baseline. That baseline is to find the half-interference at which the maximum contact pressure between the armature and rail occurs. The purpose of finding the interference where the contact pressure reaches a maximum is that the asperities will go from the elastic regime to the plastic regime if the contact pressure is roughly equal to the hardness of the material. The significance of the value is to create a baseline to compare the materials to each other. The initial contact area and the contact pressure are also necessary in determining the appropriate conditions for frictional heating and Joule heating within the system.

Other materials are being investigated to determine how the material properties affect the melt-wear. The materials investigated are listed in Table 1. Also listed are the desired characteristics that are thought to affect melt-wear. Appendix A contains their full listing of material properties. All materials chosen were the pure elements and not alloys. A low density is desired because it will reduce the weight of the armature which allows for higher acceleration by the electromagnetic forces according to Newton's Second Law of Motion. A low resistivity is desired because it means there will be less resistance for the current to travel through, thus lowering the heat caused by electric conduction. A high melting temperature is desired because the purpose is to help reduce melt-wear.

Table 1. Armature materials investigated and desired characteristics

Material	Density (kg/m3)	Resistivity (μΩ-m)	Melting Temperature (°K)
Desired Characteristic	***Low***	***Low***	***High***
Aluminum	2700	0.040	925
Molybdenum	10220	0.057	2883
Niobium	8600	0.151	2741
Tantalum	16650	0.125	3269
Titanium	4500	0.554	1941
Tungsten	19300	0.055	3695

Low Medium High

This chapter starts with an analysis to complete an artificial layer to take into account the compliance of the lab-scale launcher. Then implementing the artificial layer, the structural analysis is completed for the two armature designs and the material comparison.

3.1. Compliance Layer

The lab-scale interference of 0.1232 mm is obtained from the CAD drawing of the lab-scale EML. Because the amount of interference is relatively small, any flexure within the physical system from manufacturing or component assembly must be taken into account in the FEA model. A compliance layer is used to account for this difference and its geometrical and material properties are selected to match experimental results (detailed later).

3.1.1. Geometry, Meshing, Boundary Conditions, and Element

The lab-scale EML is constructed using several materials that take into account electrical and structural properties due to the high currents and high electromagnetic forces.

Figure 6 shows the front view of the lab-scale EML with a symmetric plane along the left and bottom edges of the model.

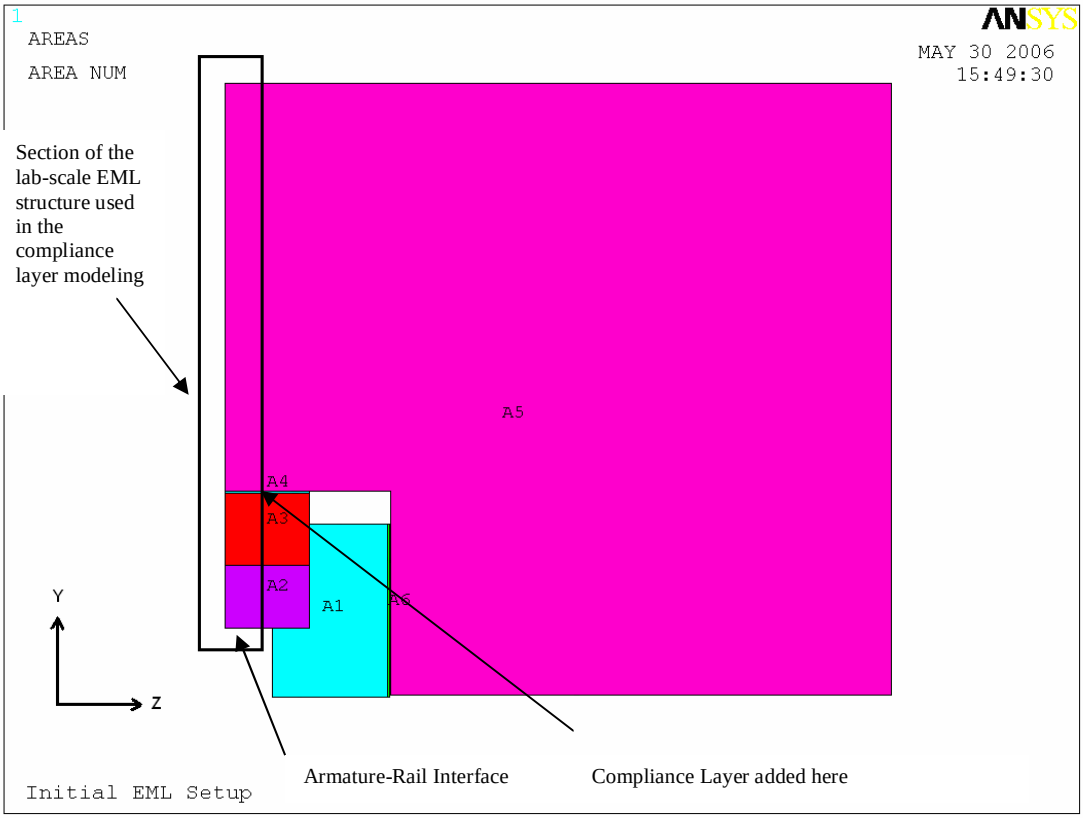

Figure 6. Front view of a quarter of the lab-scale EML without a compliance layer

Table 2. Corresponding area numbers for materials for Figure 6

Area Number	Material
A1	G10 Layer
A2	Copper Rail
A3	G10 Layer
A4	Mylar
A5	Steel Containment
A6	Mylar

Copper C110 is used for the rail because of its low resistivity. G10 and Mylar are chosen as the electric insulating materials to separate the copper rails from the steel. G10 is a glass cloth that is impregnated with an epoxy resin under pressure and heat. Mylar is one of several names used by the US and Britain for biaxial-oriented polyethylene terephthalate (boPET) polyester film. In Appendix A, the Mylar is given a value of 1 for heat capacity and thermal conductivity for FEA purposes because it is a very thin sheet and not expected to carry any thermal load. It is known for several factors, one of which is its electrical insulation properties. The steel containment is made from thin (in the x-direction or into the page of Figure 6) plates of UNS S30100 fully hardened stainless steel that are stacked and bolted together.

A lab-scale compliance test was conducted at the Extreme Tribology Research Laboratory of the Georgia Institute of Technology. The test was conducted to determine the amount of relative displacement between the rails when a force was applied to separate them. The test represents the material variability as the components are assembled. From experiments conducted, it was shown that the compliance layer can vary before shooting an armature and after shooting an armature. The data gathered from the compliance layer experiments is shown in Figure 7. These results were taken at three different times: 2005 before fire, 2006 after fire, and 2009 before fire.

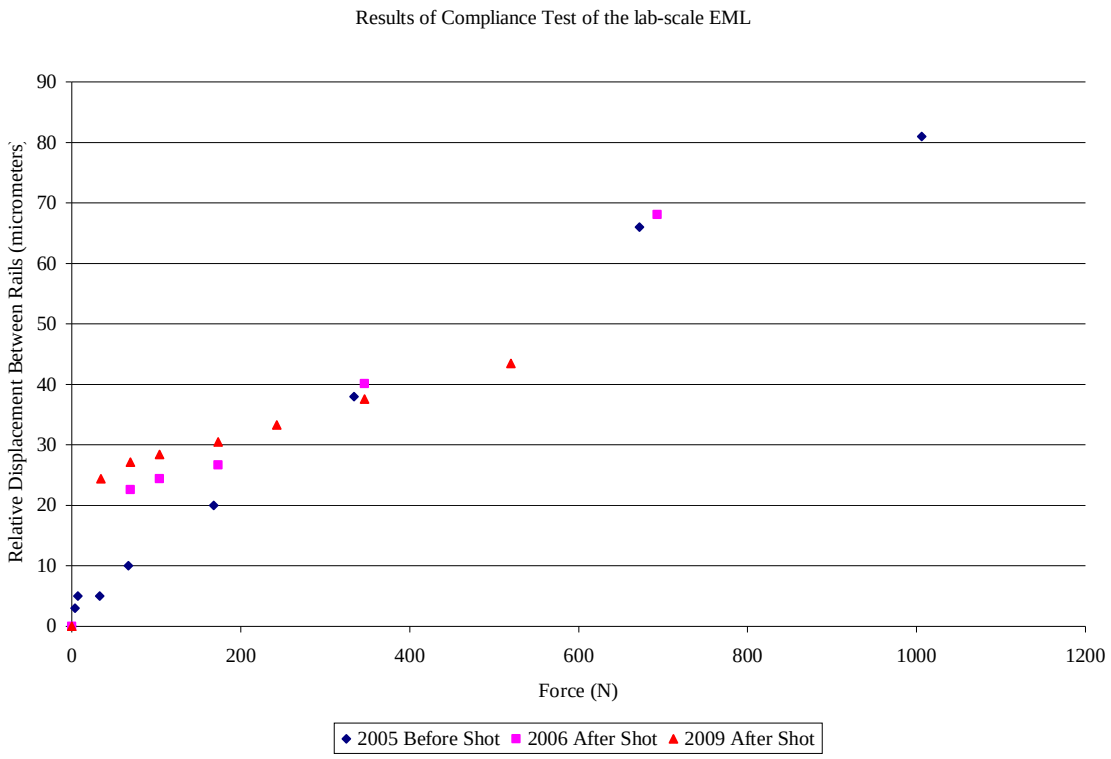

Figure 7. Results from lab-scale compliance test

From Figure 7, it is apparent that the slope of the data is steeper during the initial applied interference and then becomes less steep as more force is applied. These results imply that, initially, the forces are overcoming the free play in the system such as gaps and large asperity contact. As the force is increased and that free play is taken into account, the material flexure is represented by the more gradual slope. Therefore, when determining the FEA compliance layer, a linear regression was performed on the data where the data reflected the material stiffness dependence and not where the force was closing gaps. The data used to determine the compliance layer is shown in Figure 8.

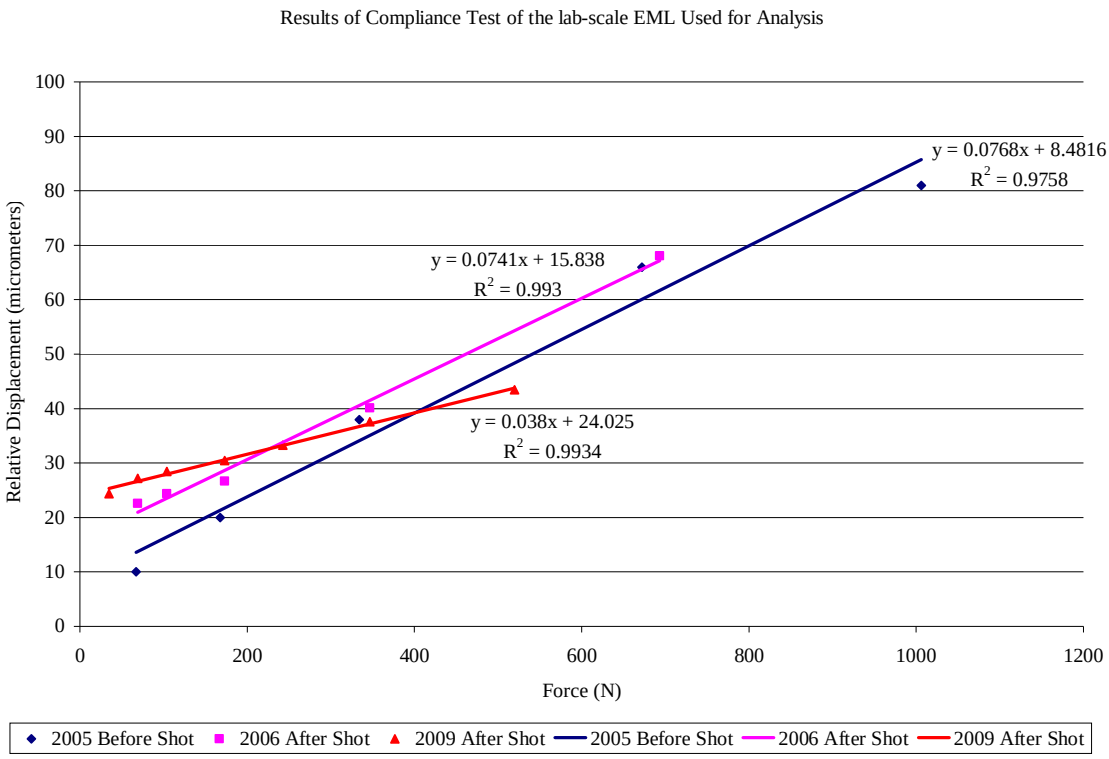

Figure 8. Compliance data used in FEA analysis with linear regression

Theoretically, the intercepts of the regression lines should be at zero when the force is equal to zero, but as stated before, the forces overcome the free play in the system and not the material stiffness. Therefore, the linear regression lines, where the material stiffness is taken into account, start after overcoming the free play, thus the nonzero intercept.

The FEA model incorporated an artificial, or compliance, layer that would account for this displacement as a force was applied to the rails. Figure 9 shows the geometry used to determine the material properties that would simulate a compliance layer.

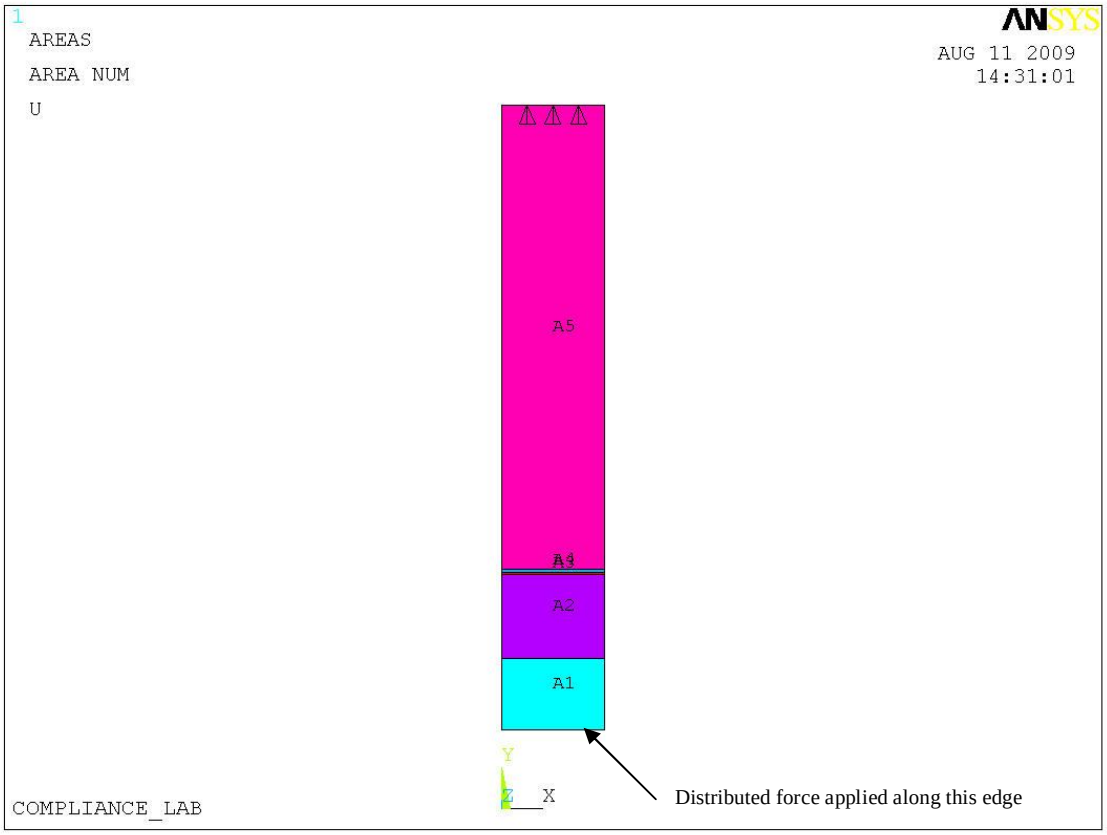

Figure 9. Geometry used in modeling the structural compliance layer

Figure 9 is the boxed section of Figure 6 with the compliance layer added between the steel and Mylar layers. The thickness of the compliance layer is 0.254 mm (0.01 inches) to keep the overall geometry of the system similar to the real launcher. The width of the rail and other layers shown in Figure 9 is 9.22 mm (0.363 inches) which is the width of the armature. Due to the symmetric geometry, only the upper rail and layers are modeled. The top edge is constrained from moving in the y-direction, while a force is applied in the upward direction on the bottom edge.

Because the length of the rail is much greater than the width, the problem is solved as a plane strain problem. A plane strain problem assumes that the displacement along the length of the rail is much smaller than the displacement in the cross-sectional area that is modeled.

Figure 10 shows the meshed FEA model used to determine the material properties of the compliance layer that would best simulate the lab-scale experiments. An element size of 0.20 mm was used. The forces from Figure 8 were applied as a distributed load on the bottom edge of the copper rail and the resulting displacement was recorded.

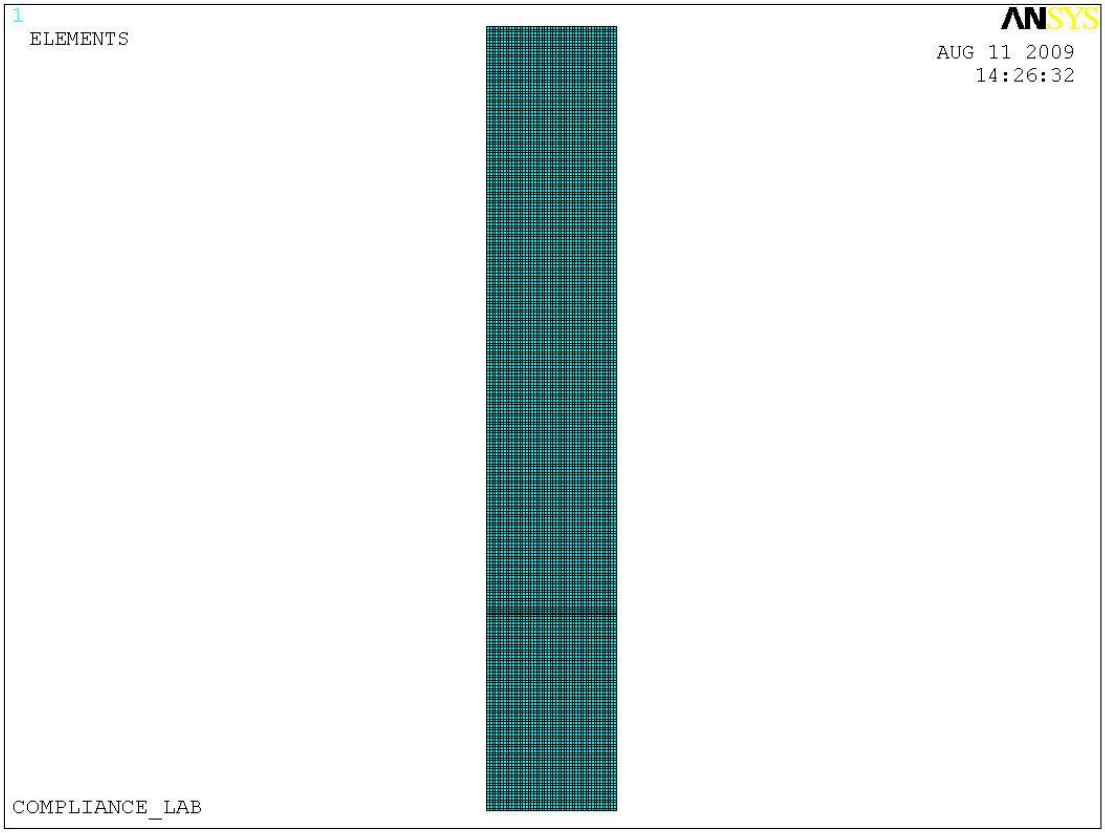

Figure 10. Mesh plot of the compliance layer FEA model

The element type used in the analysis was Plane 42 which is a 4 node 2-D element with displacement degrees of freedom: translations in the x- and y-directions. The structural solid element has the capabilities for plane stress, plane strain, or axisymmetric type problems. Figure 11 shows the schematic diagram of the Plane 42 element.

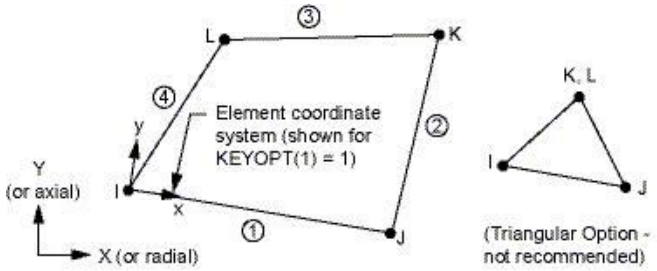

Figure 11. Diagram of the Plane 42 element [29]

3.1.2. Results and Discussion

Figure 12 shows the FEA model of displacement in y-direction as a force of 672 N is applied to the bottom edge of the rail. The force applied is based on the 2005 data for before shot measurements. The results are expected where the rail, G10, Mylar, and compliance layer, all displace while the steel remains stationary due to its larger modulus of elasticity. For this specific case, the bottom edge was displaced approximately 51.6 microns.

a)

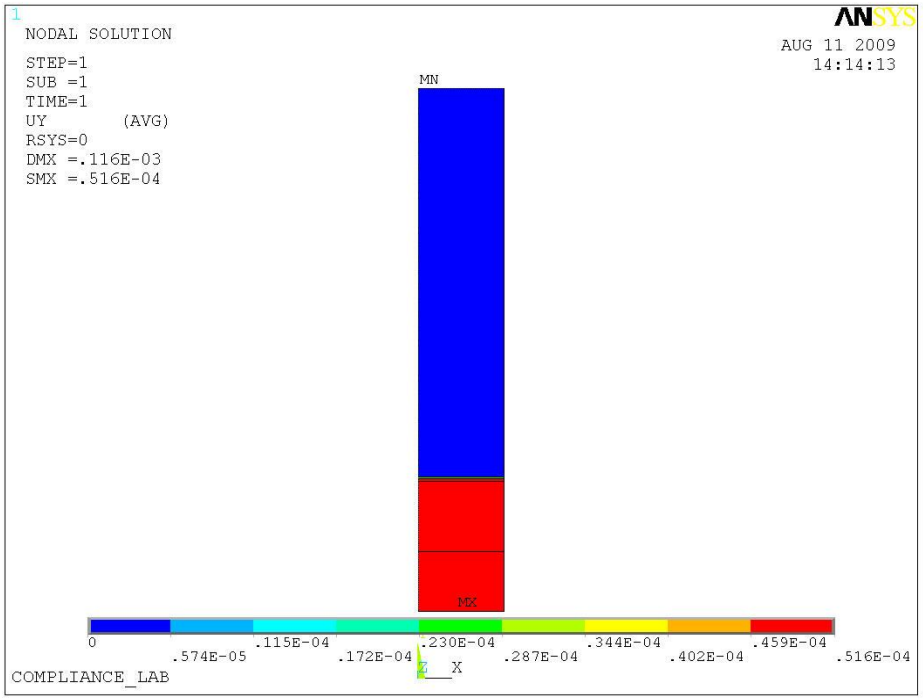

b)

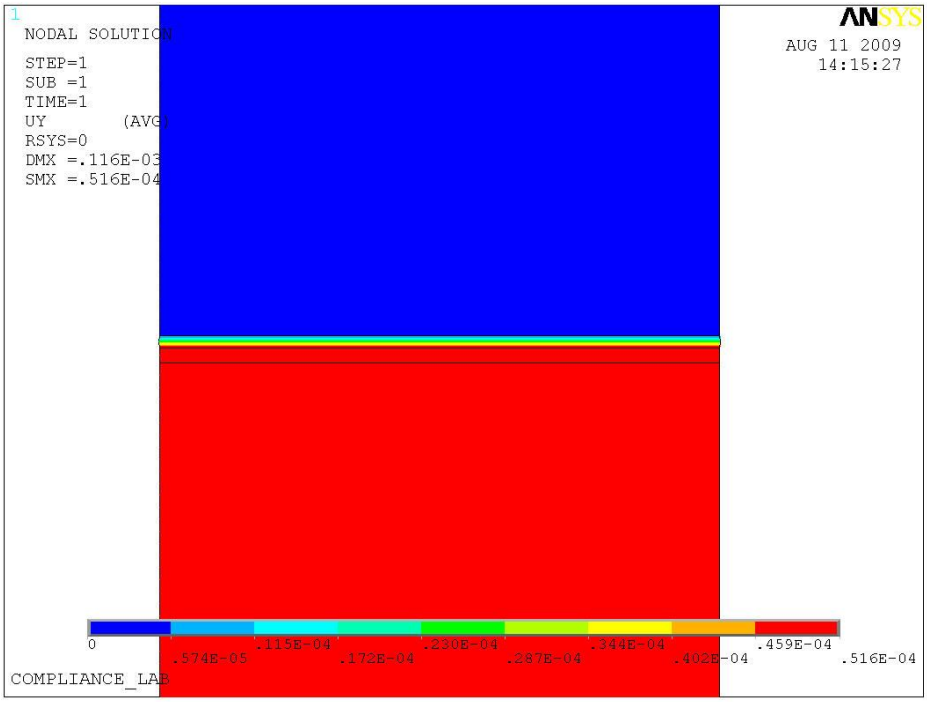

Figure 12. a) Overall and b) close-up views of displacement in the y-direction of the compliance layer with a load of 672 N for 2005 before shot

Since the materials are supposed to perform as linear elastic materials, the slope of the line as the force is applied is linear as shown in Figure 13 with an intercept at $y = 0$. Because the measured results from the lab did not perform perfectly linearly from $y = 0$, the slopes of the linear regression lines were matched instead of the relative displacement values. Essentially, it is assumed that the lab results were offset by the free play and then performed linearly elastically. Figure 13 shows just the results for measurements made before a shot in 2005.

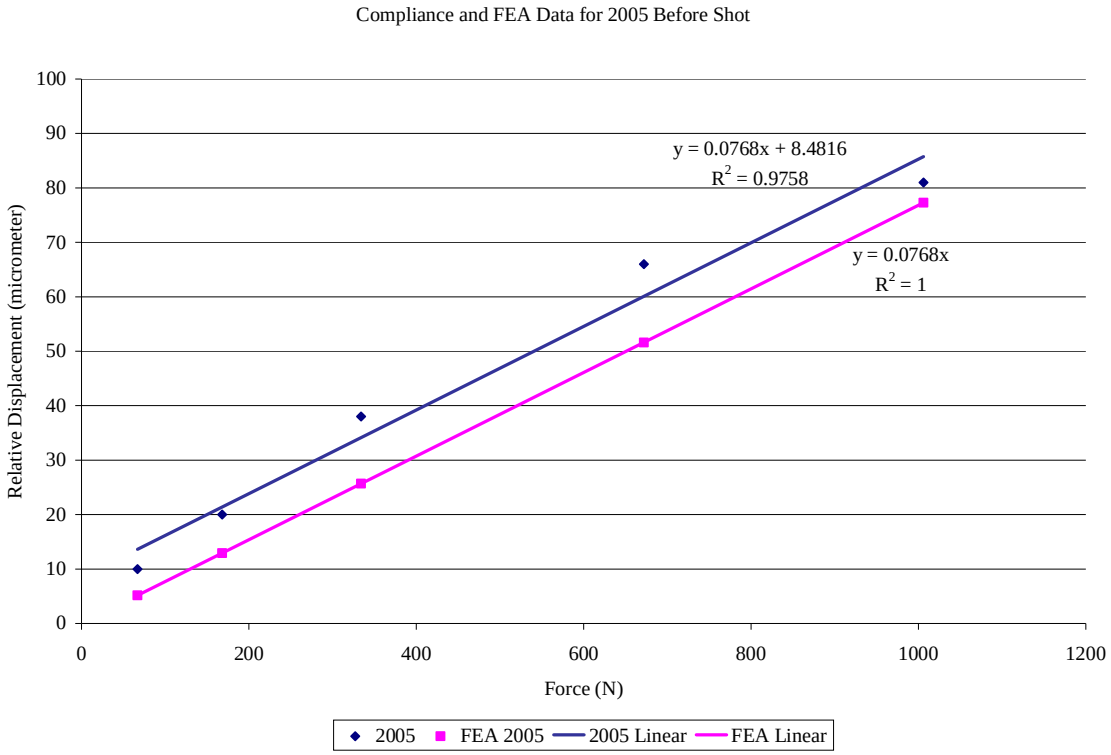

Figure 13. Compliance data and FEA results for 2005 before shot measurements

Figure 14 shows the results for the after shot measurements. Again, the intercepts for the FEA analysis were set at $y = 0$ because of the materials' linear elastic behavior. The FEA analysis was completed by varying the compliance layer's modulus of elasticity (E) and Poisson's ratio (v). Those values were varied in the FEA model until the slopes of

the FEA linear regression lines were similar to their corresponding lab measurement regression lines.

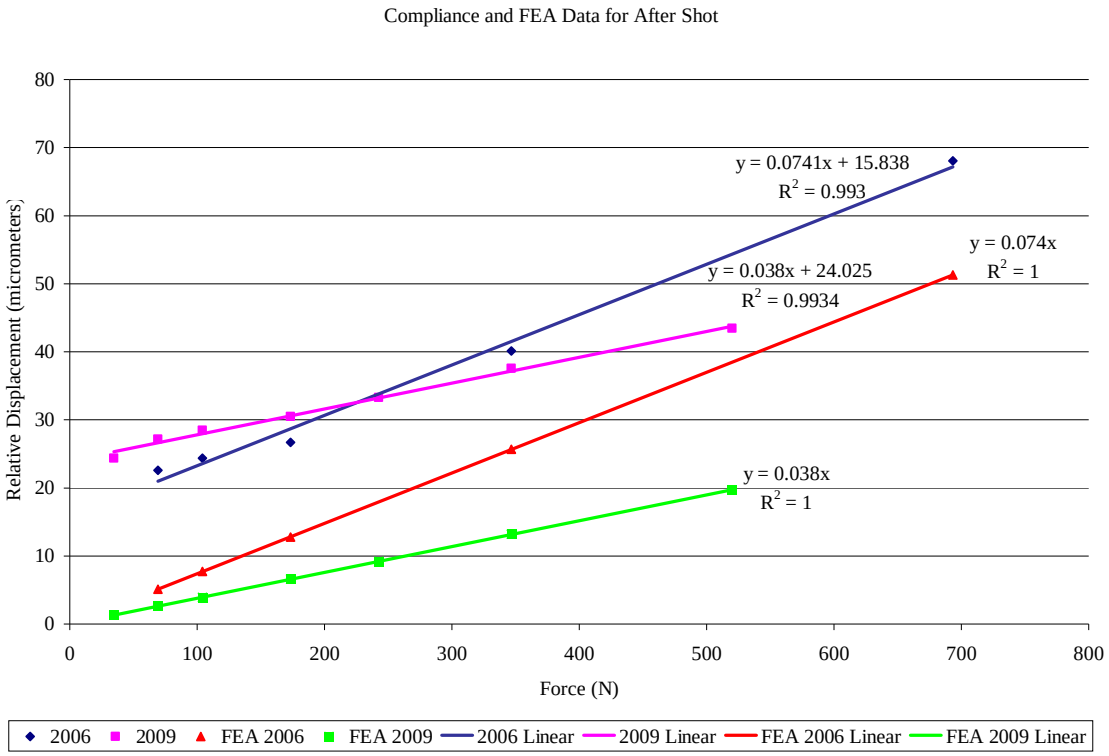

Figure 14. Compliance data and FEA results for 2006 and 2009 after shot measurements

Table 3 shows the material properties used for the compliance layer in the FEA model to give the appropriate slopes for each lab measurement sets of data. This range of values for the compliance layer was used as part of the parametric analysis to see the different effects on the analyses performed. Because of the lower values of the modulus of elasticity for the compliance layer relative to the values of the other materials, the most deformation occurs in that layer as evidenced by Figure 12.

Table 3. Compliance layer material properties determined from FEA results

Year	Modulus of Elasticity (MPa)	Poisson's Ratio
2005	0.290	0.27
2006	0.299	0.27
2009	0.584	0.27

In summary, an artificial layer was created in the FEA model to simulate the deformations brought about from manufacturing and component imperfections. Based on measurements completed on the lab-scale launcher, a range of Young's modulus values were found to range from 0.290 MPa to 0.584 MPa, while the Poisson's ratio stayed at 0.27. The initial contact analysis is performed for the softer (0.290 MPa) and harder (0.584 MPa) compliance layers for each armature design and all materials. Therefore, 4 sets of data were obtained.

3.2. Initial Contact

The interference of the lab-scale EML is 0.25 mm, obtained from the CAD drawings. As stated before, since only half of the system is modeled due to the symmetric geometry and thus the interference is set to 0.12 mm. Also, the compliance layers described in the previous section were added to account for the discrepancy between the FEA model and the lab-scale model.

As highlighted in Figure 15, currently, the taper on the legs is approximately 1.04°. The modification made to the geometry is to reduce that angle to approximately 0.5° by increasing the leading dimension that is also highlighted. This taper is what affects the contact area between the armature legs and the rail.

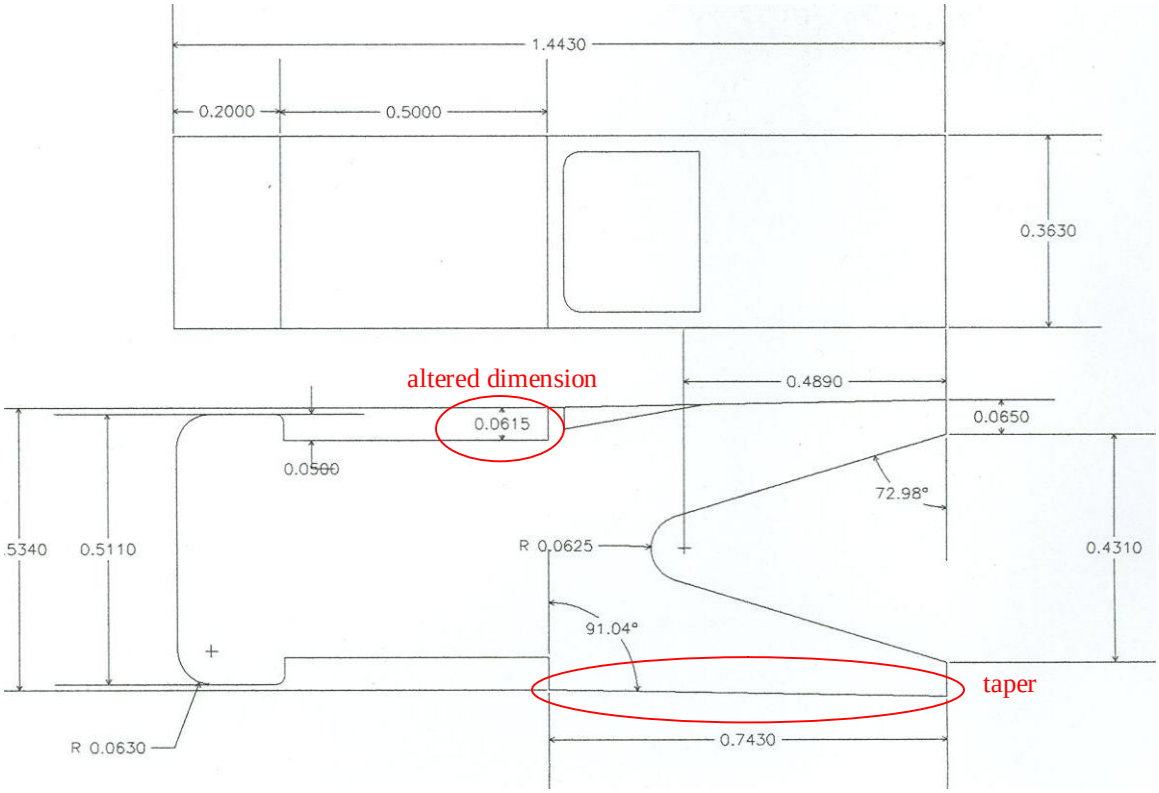

Figure 15. Armature geometry using in the lab-scale EML (all dimensions in inches)

The current armature material that is used in the lab-scale EML is Aluminum 6061-T651.

3.2.1. Geometry, Meshing, Boundary Conditions, and Element

The FEA model created simulates a gradual interference of the rail to the armature and is performed on a PC (Intel Xeon CPU 3.00 GHz, 8.00 GB of RAM). The simulation is run by moving the rail system towards the armature to simulate the interference. This movement, instead of sliding the armature into the rail, requires fewer steps for convergence, which shortens the simulation time.

Figure 16 shows the geometry used in the FEA model for the structural analysis for both of the armature designs. The difference in the models is not easily visible because the reduction in the angle is very small. Because the length of the rails relative to the armature size is so large, the extra length is insignificant for the initial contact

analysis. The concern is localized to the area around the armature and thus the rails are shortened to approximately 0.55 meters. As stated before, because of the symmetric geometry, only half of the lab-scale EML is modeled. This also reduced the amount of calculations necessary for a solution which allows for a finer mesh at the interface between the armature and rail. Also, the compliance layer mentioned before is added between the Mylar layer and the steel containment in the FEA model. The positive X and Y directions are defined to be to the right and to the top, respectively, and will be referenced as such through this chapter.

a)

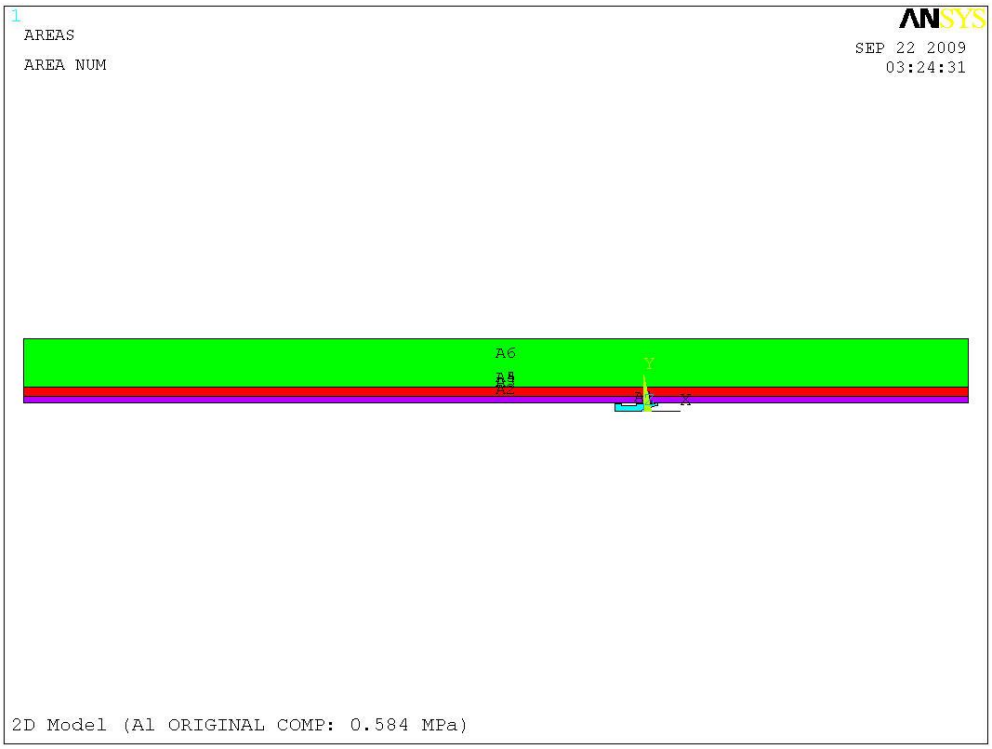

b)

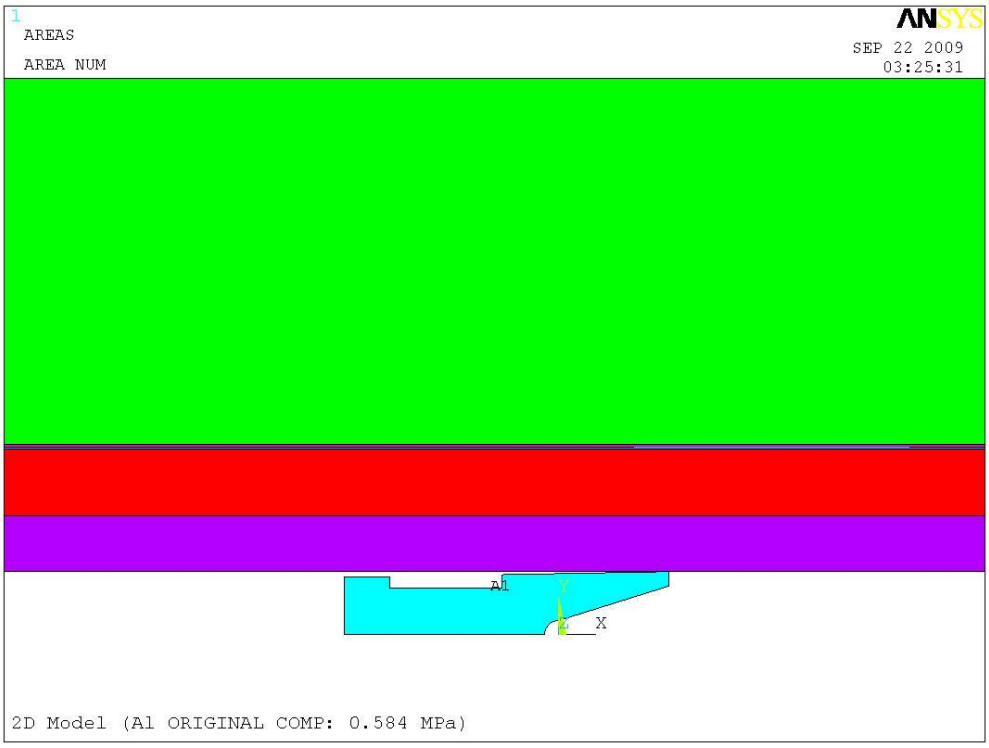

Figure 16. a) Overall and b) close-up views of the geometry of the FEA model used for the initial contact structural analysis

The left and right edges of the rail, not shown in Figure 16, are constrained so that motion in the X direction is not allowed. A symmetric boundary condition is placed along the bottom edge of the armature. The half-interference is applied by iterating a downward displacement on the top edge of the steel area. The downward displacement is iterated until the total displacement is -0.1232 mm. To constrain the armature, the keypoint at the leading edge of the armature is constrained of all movement. This allows the leg of the armature to freely flex while the armature body cannot slide along the rail.

Figure 17 shows a plot of the mesh used in the initial contact simulation. As shown, the mesh where the contact is expected to occur is refined to give a more accurate solution. The finer mesh is also applied at the bend between the legs because it acts as a stress concentration as well. The finer mesh size is approximately 0.524 µm by 0.449 µm.

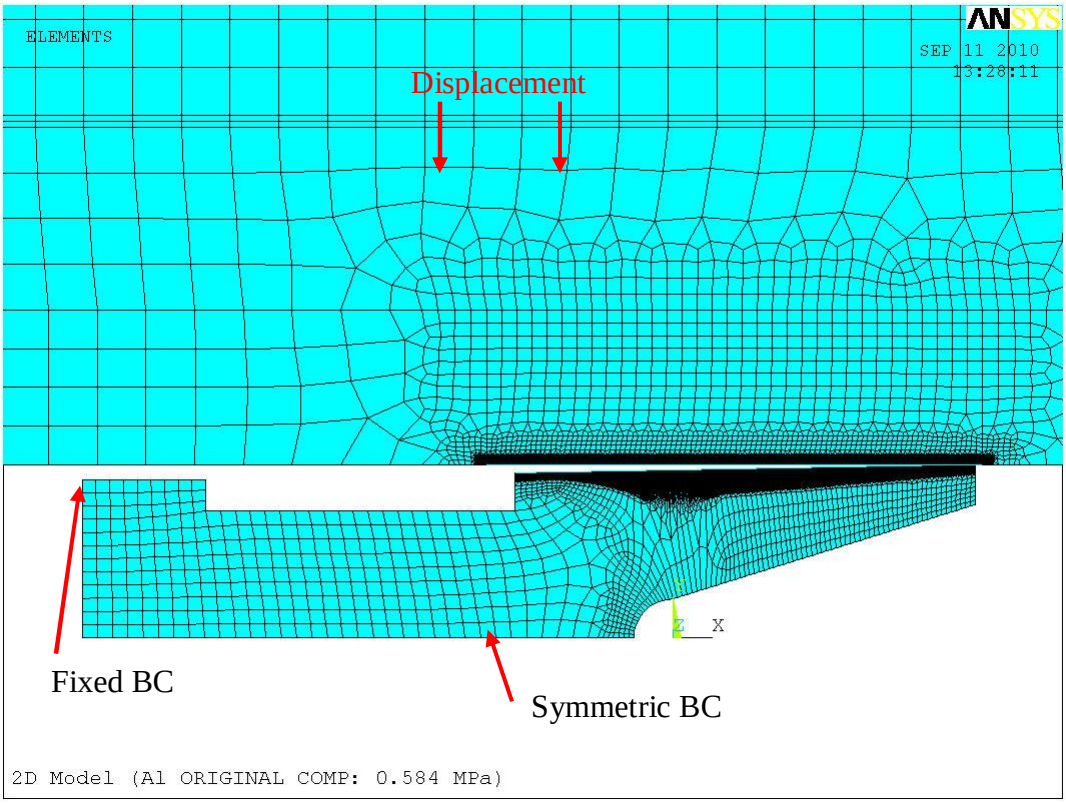

Figure 17. Mesh plot of the initial contact FEA model

The element used for this uncoupled analysis was the Plane 82 element, which is similar to the Plane 42 element that was used in the compliance layer FEA model. The Plane 82 element is an 8 node 2-D element instead of a 4 node 2-D element as show in Figure 18. The plane stress analysis option was used and a thickness of 9.22 mm was applied to the armature and a thickness of 12.5 mm was applied to the rail and above layers. The armature thickness is the thickness of the lab-scale armature currently used and 12.5 mm is the barrel depth into the page. Figure 19 shows the contact and target element pair used for the analysis. The elements used were CONTACT 172 and TARGET 169. The contact pair is used by the FEA program to treat two surfaces as impenetrable bodies. Instead of overlapping areas, the boundaries will remain and forces and stresses are calculated based on that principle.

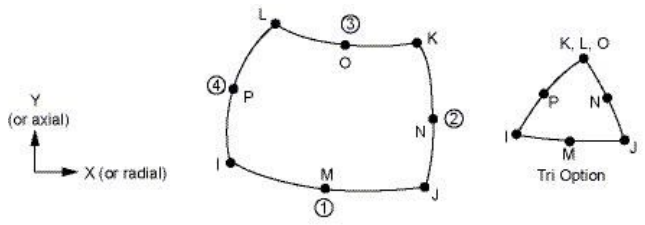

Figure 18. Diagram of the Plane 82 element [29]

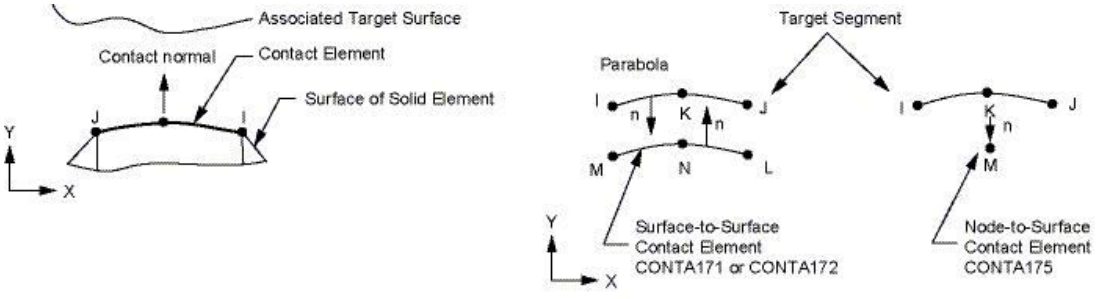

Figure 19. Diagram of the contact and target element [29]

3.2.2. Results and Discussion

The format of this section will compare the original design to the modified design at the lab-scale interference with aluminum as the armature material. The next section will compare the materials to each other for each design. Also, all comparisons will include the hard and soft compliance layer results. It should also be noted that the results given in this section are for the macro-scale system only and do not take into account any micro-scale aspects.

3.2.2.1 Design Comparison

As expected, the maximum tension of the armature from the half-interference of the rails occurs at the contact while the maximum compression occurs along the bottom edge of the legs. This applies to both designs of the armature. Figure 20 and Figure 21 shows the displacement results in the Y direction for both designs of the aluminum armature at the lab-scale interference of 0.1232 mm for the hard and soft compliance layers.

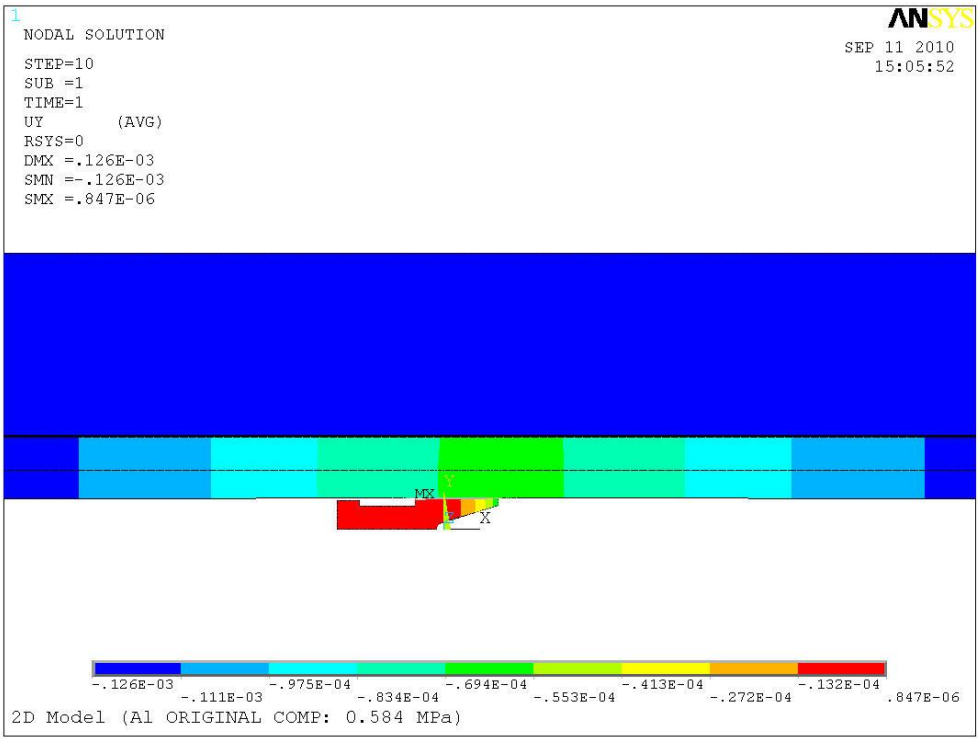

a)

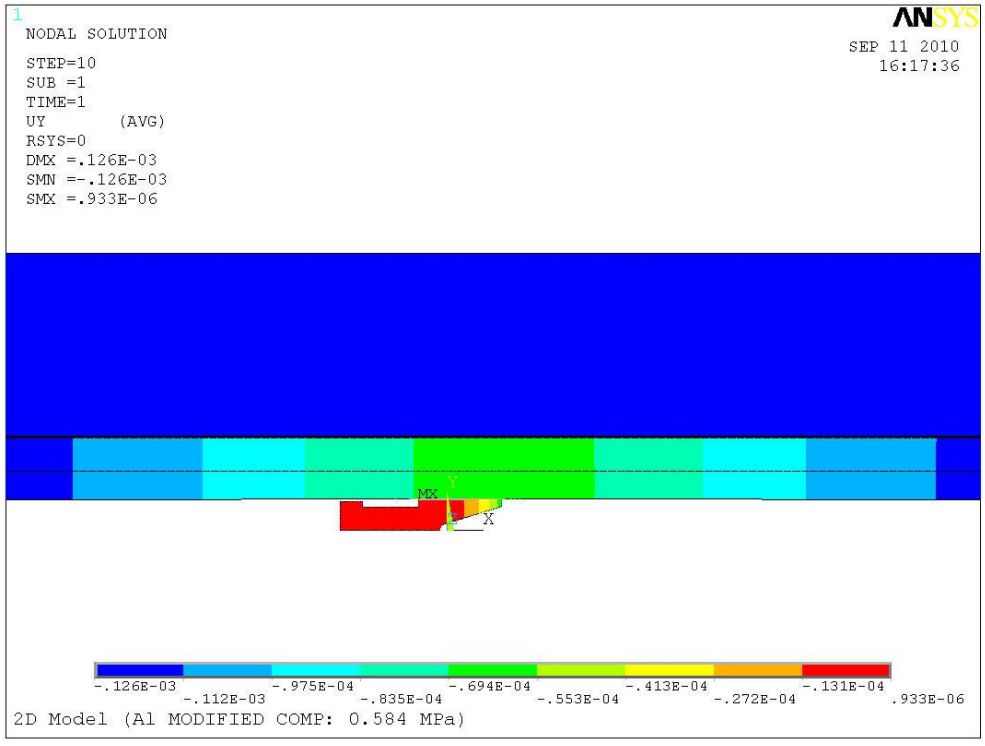

b)

Figure 20. Displacement distribution in the y-direction at an interference of 0.1232 mm for the a) original and b) modified design with the hard compliance layer

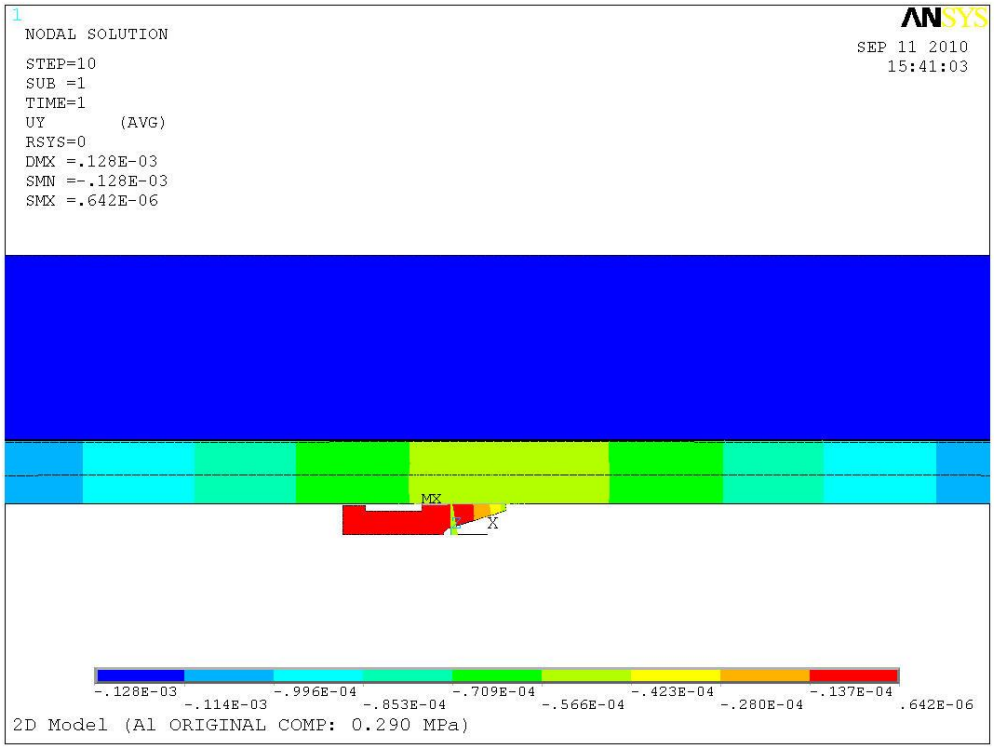

a)

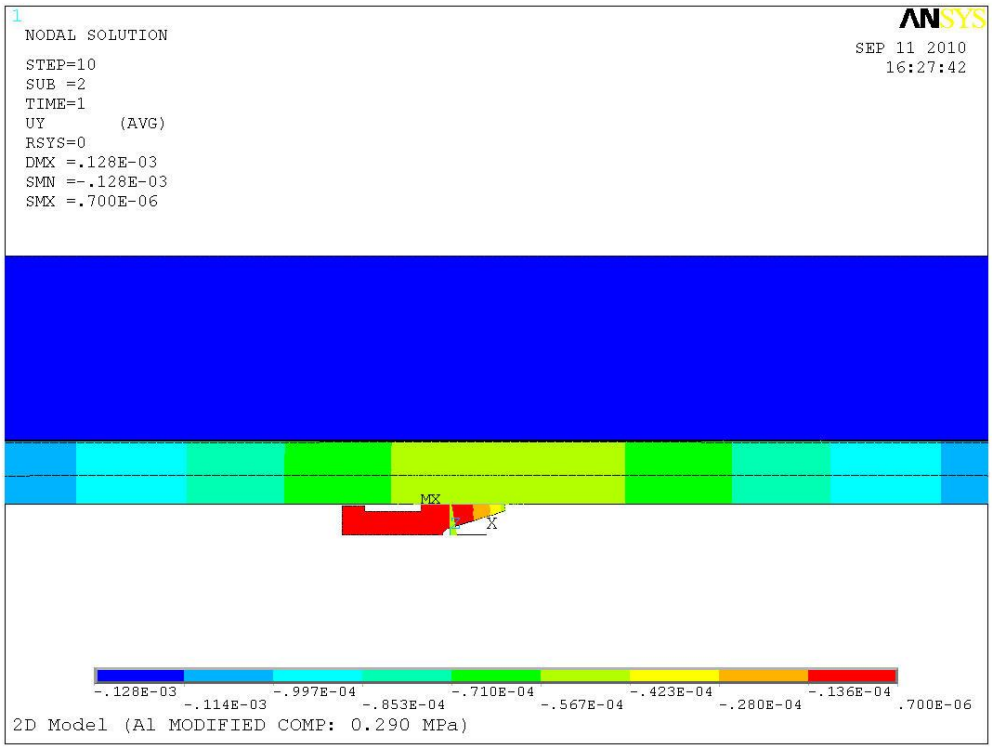

b)

Figure 21. Displacement distribution in the y-direction at an interference of 0.1232 mm for the a) original and b) modified design with the soft compliance layer

The maximum von Mises stress of both designs and both compliance layers throughout the system does not exceed the yield strength of the weaker material, aluminum (276 MPa), at the lab-scale half-interference. As seen in Figure 22 and Figure 23, the maximum stresses occur at the contact in the rail for the original design and the hard compliance layer with a von Mises stress value of 4.97 MPa. For the original design and soft compliance layer the maximum von Mises stress occurs at the contact in the armature with a value of 4.33 MPa. The maximum von Mises stress in the modified design and hard compliance layer occurs at the contact in the armature and is 1.08 MPa, while the modified design and soft compliance layer occurs at the contact in the rail with a value of 1.72 MPa. With both compliance layers, neither design exceeds the yield strength, so both designs are feasible. The von Mises stress values are summarized in Table 4 for both designs and both compliance layers. Structurally, the optimal design choice is indeterminate.

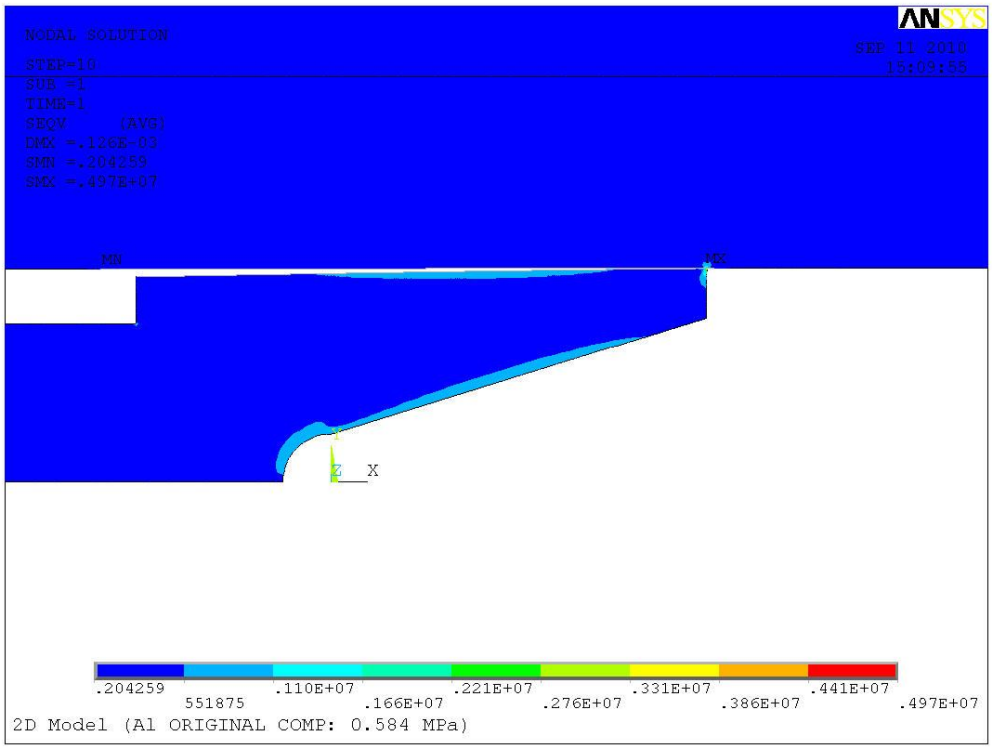

a)

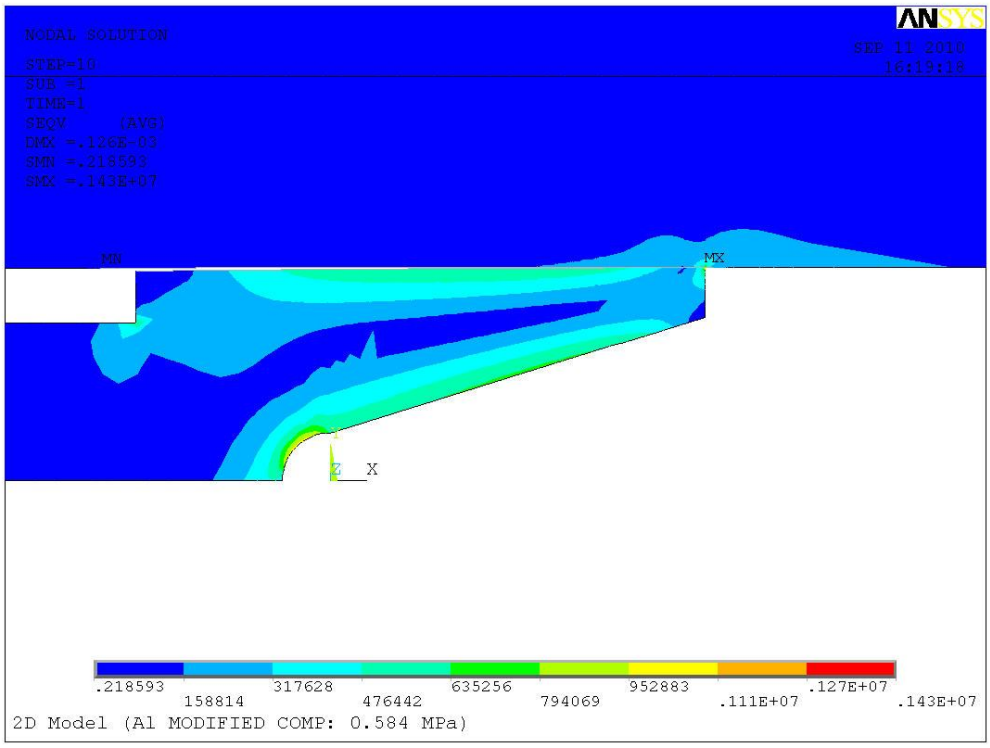

b)

Figure 22. The von Mises stress distribution at a half-interference of 0.1232 mm for the a) original and b) modified designs with the hard compliance layer

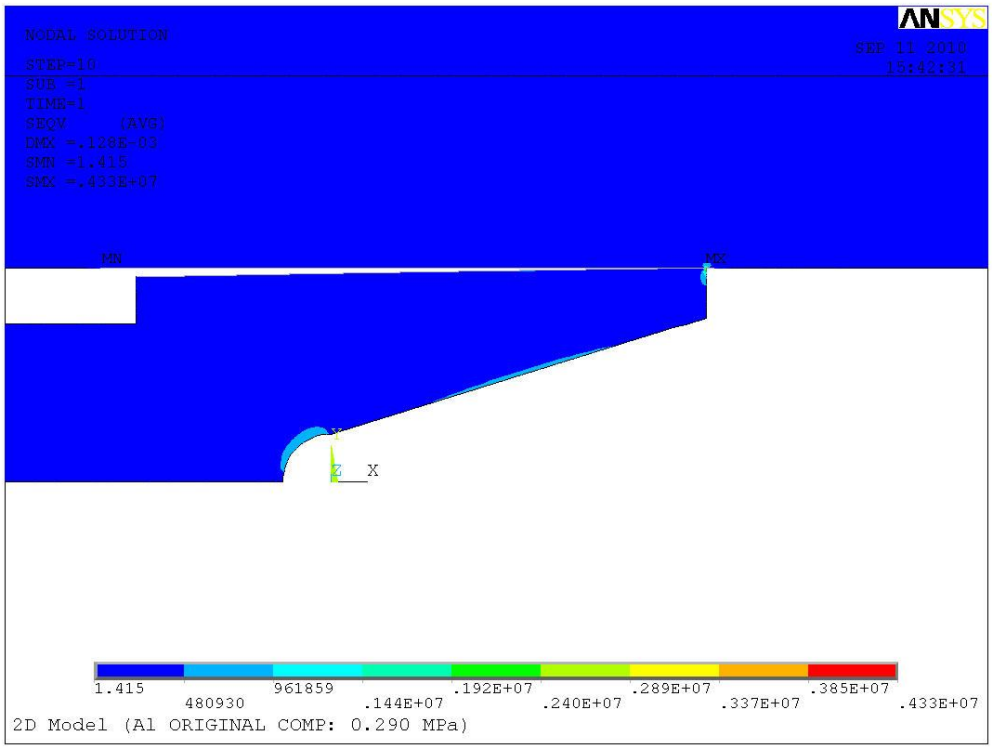

a)

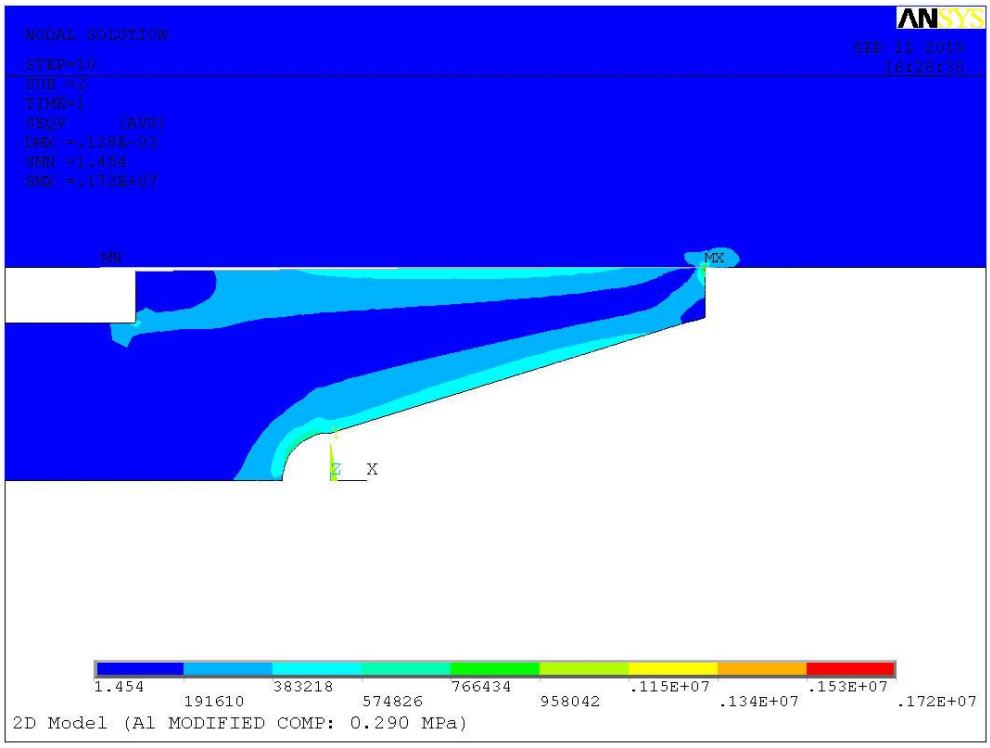

b)

Figure 23. The von Mises stress distribution at a half-interference of 0.1232 mm for the a) original and b) modified designs with the soft compliance layer

Table 4. von Mises stress values for the original and modified designs with the hard and soft compliance layers

	Bend Stress (MPa)	**Contact Stress (MPa)**
Original Hard	1.01	4.28
Original Soft	0.7629	4.33
Modified Hard	1.02	1.00
Modified Soft	0.7632	1.41

The contact pressure is also evaluated at the lab-scale half-interference for both designs and compliance layers. The contact pressure distribution is shown in Figure 24 and Figure 25.

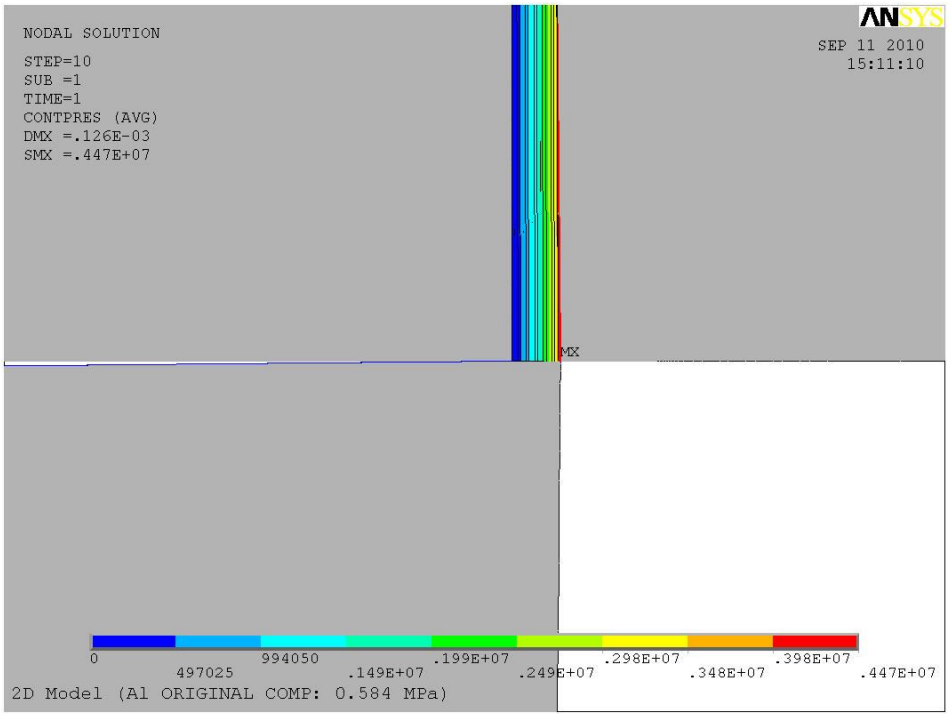

a)

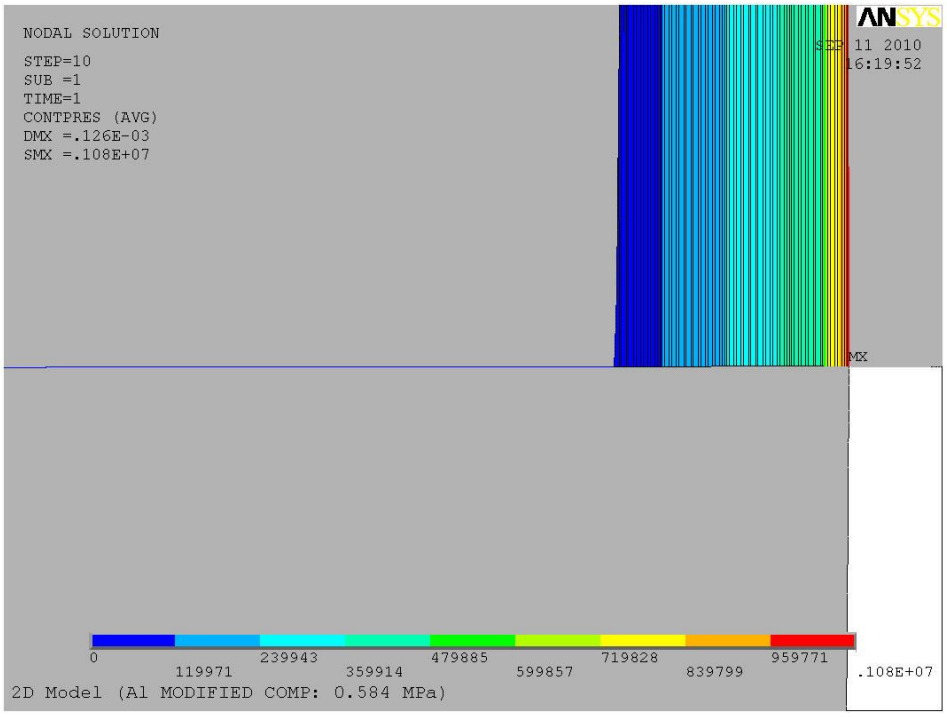

b)

Figure 24. Contact pressure at a half-interference of 0.1232 mm for the a) original and b) modified design with the hard compliance layer (different view scales)

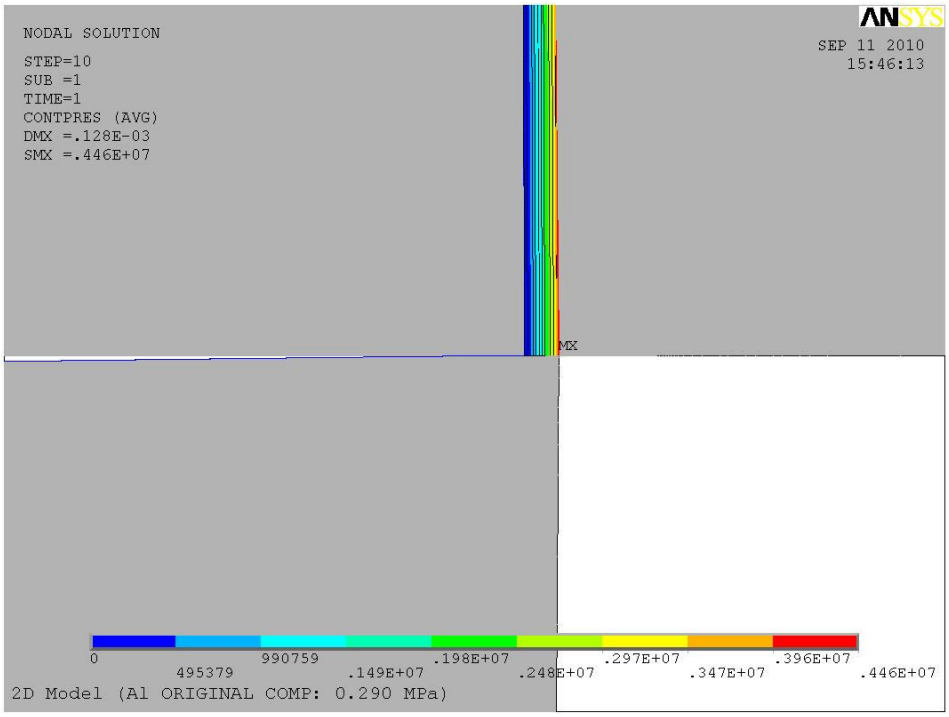

c)

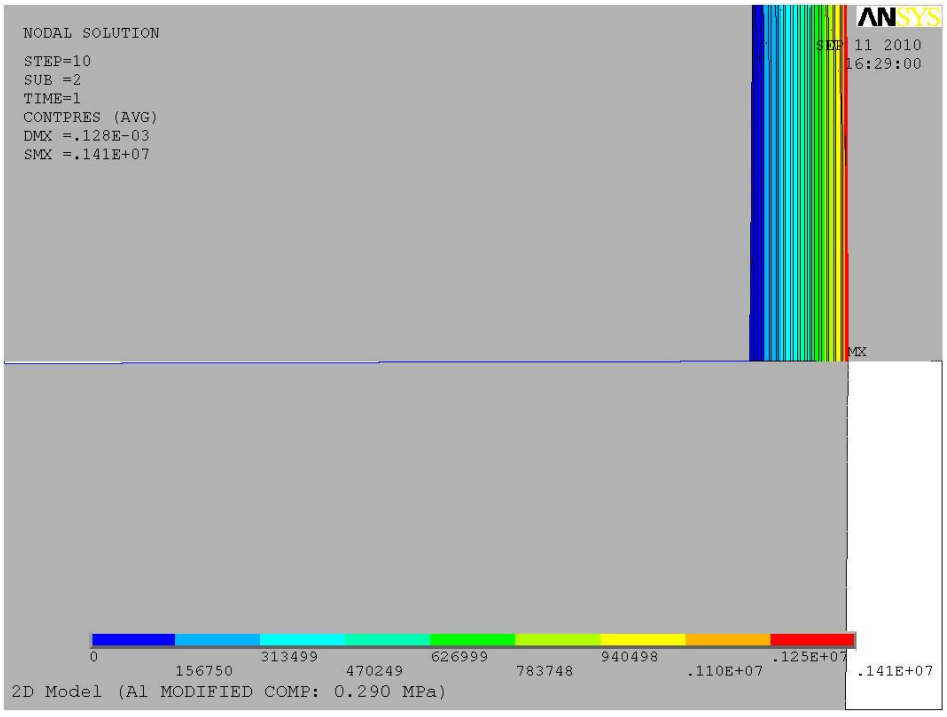

d)

Figure 25. Contact pressure at a half-interference of 0.1232 mm for the a) original and b) modified design with the soft compliance layer (different view scales)

The results of the FEA model, displayed in Figure 26 and Figure 27, show that as the interference increases, the maximum contact pressure between the armature and the rail will gradually increase but eventually decrease. For the original designs and both compliance layers the contact pressure gradually decrease after the pressure reaches a maximum. However, for the modified design and both compliance layers the contact pressure rapidly decreases after their maximums. This is likely due to the rapidly increasing area for the force to be spread over as the interference increases. It should also be noted that the scale of the interference is different between cases because some cases required more interference to have a maximum in the contact pressure.

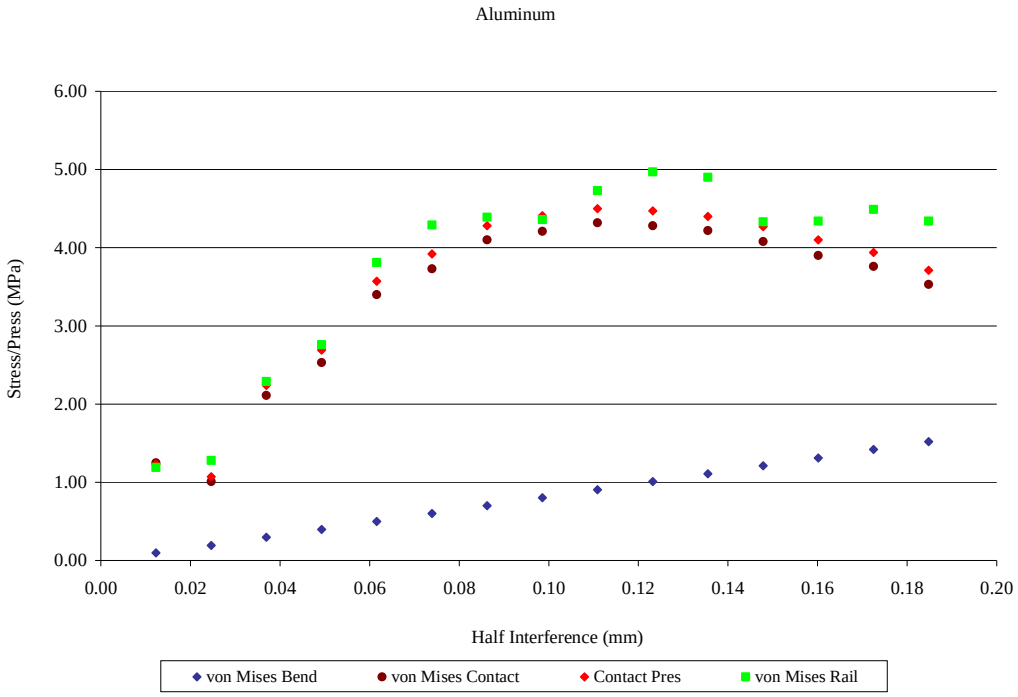

a)

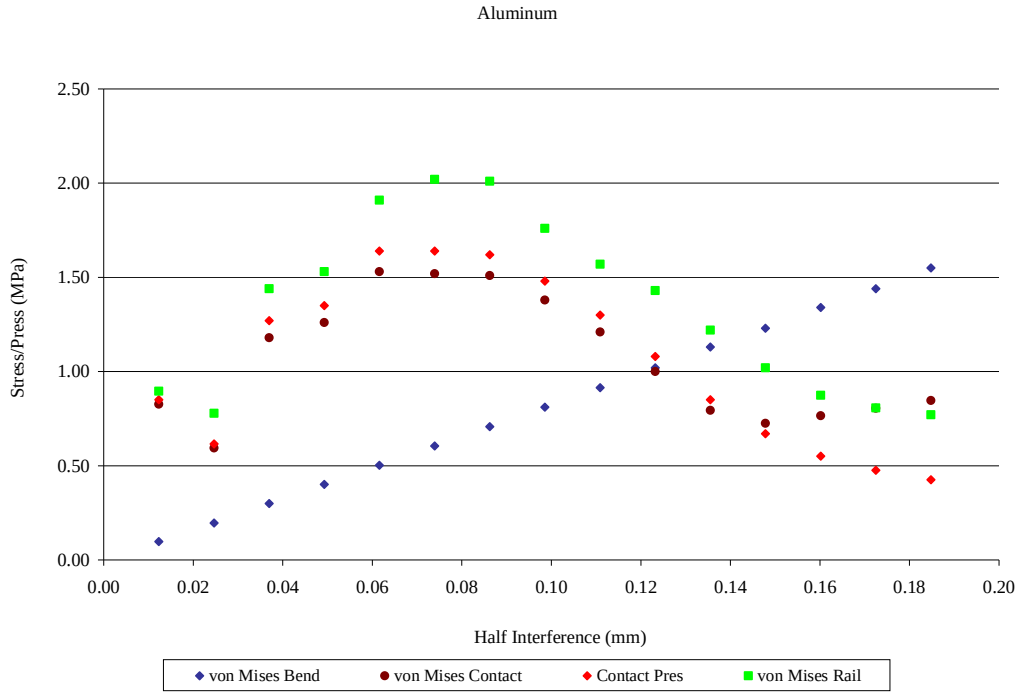

b)

Figure 26. The von Mises stresses and contact pressures for the a) original and b) modified design with the hard compliance layer

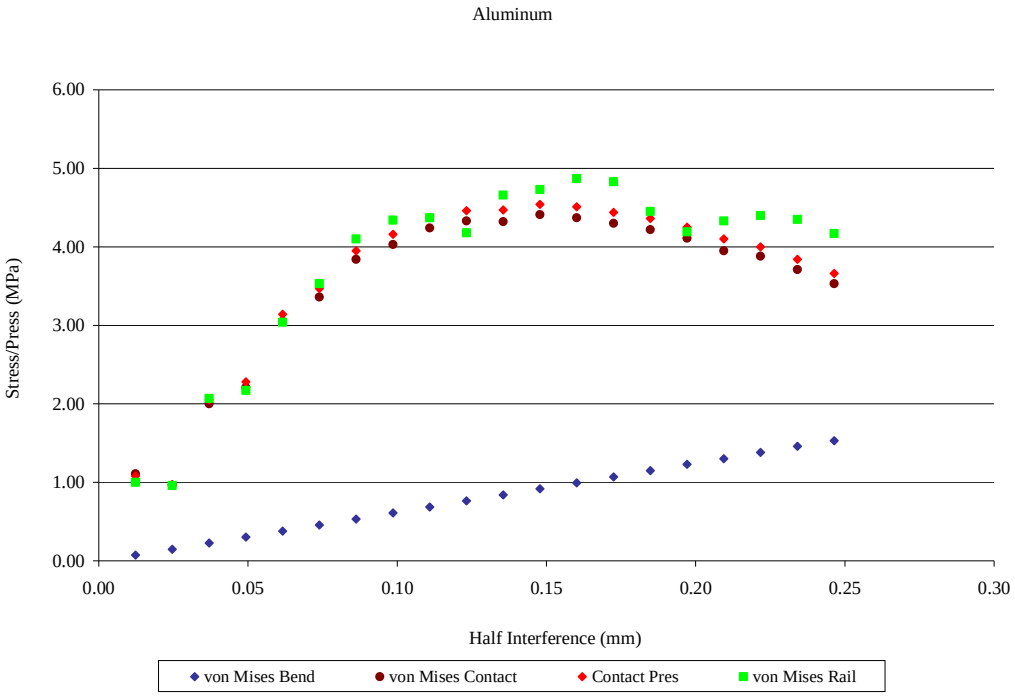

c)

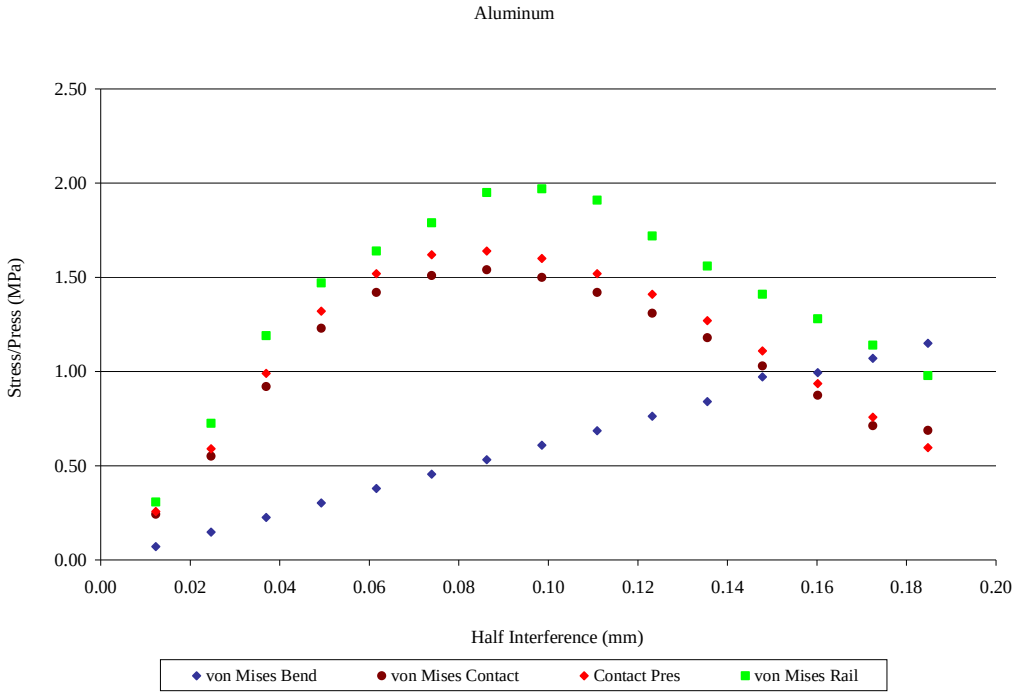

d)

Figure 27. The von Mises stresses and contact pressures for the a) original and b) modified design with the soft compliance layer

From Figure 26 and Figure 27, it is apparent that at a certain half-interference the contact pressure reaches a maximum. However, the maximum values are below the hardness (Appendix A) of either material and, therefore, do not deform plastically.

3.2.2.2. Material Comparison

Based solely on the lowest maximum von Mises stress value at the lab-scale interference, the material choice would be aluminum. However, to compare the materials to each other the maximum contact pressure criterion was found. The maximum contact pressure criterion is based on the interference when the maximum contact pressure between the rail and armature in the FEA model occurs. At that interference the force acting on the armature and contact area is found.

As stated before, the half-interference when the maximum contact pressure occurs is estimated (from figures such as Figure 26 and Figure 27) in order to compare the materials of the armature. Table 5 shows the values of the half-interference when the maximum contact pressure is obtained along with the corresponding contact lengths and forces. It shows the values for the hard and soft compliance layers. The contact length is measured using the contact status found by ANSYS and the geometry check feature.

Table 5. Half-interference, contact length, and force at which maximum contact pressure occurs for the a) hard and b) soft compliance layers

a)

Armature Material	Original Design			Modified Design		
	Half Interference (mm)	*Contact Length (mm)*	*Contact Force (N)*	*Half Interference (mm)*	*Contact Length (mm)*	*Contact Force (N)*
Aluminum	0.118	0.105	208	0.0706	0.173	128
Molybdenum	0.332	0.177	1021	0.182	0.237	565
Niobium	0.142	0.132	306	0.0892	0.205	196
Tantalum	0.199	0.136	530	0.124	0.204	335
Titanium	0.105	0.0706	237	0.0842	0.409	201
Tungsten	0.404	0.221	1287	0.146	0.689	502

b)

Armature Material	Original Design			Modified Design		
	Half Interference (mm)	*Contact Length (mm)*	*Contact Force (N)*	*Half Interference (mm)*	*Contact Length (mm)*	*Contact Force (N)*
Aluminum	0.150	0.0971	201	0.0864	0.176	118
Molybdenum	0.480	0.188	952	0.287	0.250	573
Niobium	0.0619	0.0401	95.2	0.119	0.200	188
Tantalum	0.392	0.147	553	0.173	0.188	316
Titanium	0.0547	0.0363	87.1	0.127	0.190	207
Tungsten	0.571	0.177	1158	0.332	0.252	677

Because the depth into the page is known to be 9.22 mm, which is the width of the armature, the contact area can be estimated for the half-interferences given in Table 5. A summary of the contact area and pressure is shown in Table 6. The average contact pressure is found by dividing the force required to displace the rails by the estimated contact area. The average contact pressure is used in the friction study for the thermal analysis, while the contact area is used in both the friction and Joule heating study.

Table 6. Estimated contact area and pressure for each half-interference that meets the maximum contact pressure criterion for the a) hard and b) soft compliance layers

a)

Armature Material	Original Design		Modified Design	
	Contact Area (mm^2)	*Contact Pressure (GPa)*	*Contact Area (mm^2)*	*Contact Pressure (GPa)*
Aluminum	0.965	0.215	1.60	0.0803
Molybdenum	1.63	0.626	2.18	0.259
Niobium	1.22	0.252	1.89	0.104
Tantalum	1.25	0.423	1.88	0.179
Titanium	0.651	0.365	3.77	0.0532
Tungsten	2.04	0.631	6.35	0.0790

b)

Armature Material	Original Design		Modified Design	
	Contact Area (mm^2)	*Contact Pressure (GPa)*	*Contact Area (mm^2)*	*Contact Pressure (GPa)*
Aluminum	0.896	0.225	1.63	0.0728
Molybdenum	1.73	0.550	2.31	0.249
Niobium	0.369	0.258	1.84	0.102
Tantalum	1.35	0.409	1.74	0.182
Titanium	0.335	0.260	1.75	0.118
Tungsten	1.63	0.710	2.33	0.291

The following is a summary of the results from the initial contact FEA analysis:

1. For the lab-scale half-interference, the magnitude of the maximum von Mises stress for both models does not reach the yield strength of aluminum (armature) for either armature design or compliance layer.

2. Structurally, either design of the armature is acceptable because neither design yields before the lab-scale half-interference. This applies to both compliance layers. However, the contact pressure for the original design (~4.5 MPa for both compliance layers) is higher than the contact pressure for the modified design (~1 MPa for both compliance layers).
3. Between the compliance layers, the behavior seen is that with the softer compliance layer, the rail gives more relief to the stress distribution in the armature at the bend. Therefore, the bending von Mises stress and contact pressure values for the softer compliance layer analysis were usually lower than the values for the harder compliance layer. However, the von Mises stress at the contact was higher for the softer compliance layer.
4. The maximum contact pressure criterion provides a baseline to compare the materials and obtain the corresponding contact pressures and estimated contact areas as summarized in Table 5 and Table 6.

The structural FEA results are not very conclusive when determining factors that affect melt-wear. However, the results are important in the calculations and analysis involving the thermal analyses. The contact pressure and area can vary the amount of heat generated by friction and electricity.

CHAPTER 4: ELECTROMAGNETIC ANALYSIS

The focus of this chapter is on the electromagnetic analysis portion of the study. The greatest advantage of using an EML is that combustible chemical ignitions are eliminated. The propelling force involved with an EML is the electromagnetic force generated from a high current as manifested by the Lorentz force. The physics of the Lorentz force, $\vec{F}$, acting on a particle is explained by Equation 4.1.

$$\vec{F} = q\left(\vec{E} + \vec{v} \times \vec{B}\right) \tag{4.1}$$

where

$q =$ electric particle charge [C]

$\vec{E} =$ electric field [V-m^{-1}]

$\vec{v} =$ velocity of the electric particle [m-s^{-1}]

$\vec{B} =$ magnetic field [T]

The driving electric force occurs from the high electric current that is conducted through the rails and armature. Because of the high current, electric and magnetic fields are created locally in the rails and accelerates the armature according to the principles of the Lorentz force.

4.1. Electromagnetic Analysis

For this analysis, the simulation was a 3-D model in a quasi-static condition. The armature is static in the simulation but the current is varied over time according to the lab current data. Also, due to the complexity of the analysis, this model is uncoupled from the structural, thermal, and modal analysis.

4.1.1. Geometry, Meshing, Boundary Conditions, and Elements

The 3-D model used in the analysis is shown in Figure 28. The model shows the two rails, the armature, and the air space surrounding the rails and armature. The air is modeled because the electric and magnetic fields reside within those elements. Since electric and magnetic fields are 3-dimensional, air must be modeled in a 3-D model.

As stated before, the armature is held stationary while the current changes over time. The magnitude of the EMAG force is calculated based on this quasi-static condition. Also, only approximately 0.2 m of length of the rails is modeled since the armature does not move. The contact of the armature with the rails occurs approximately in the center for the rail length to eliminate any possible variations from having the armature close to the current inlet and outlet. The interference is created by displacing the rails inwards towards the armature the lab-scale displacement of 0.1232 mm. For the purposes of making the EMAG simulation less complex, a perfect and continuous contact is assumed throughout the simulation. As labeled in Figure 28b, the current enters through the top rail and exits through the bottom rail by grounding that area.

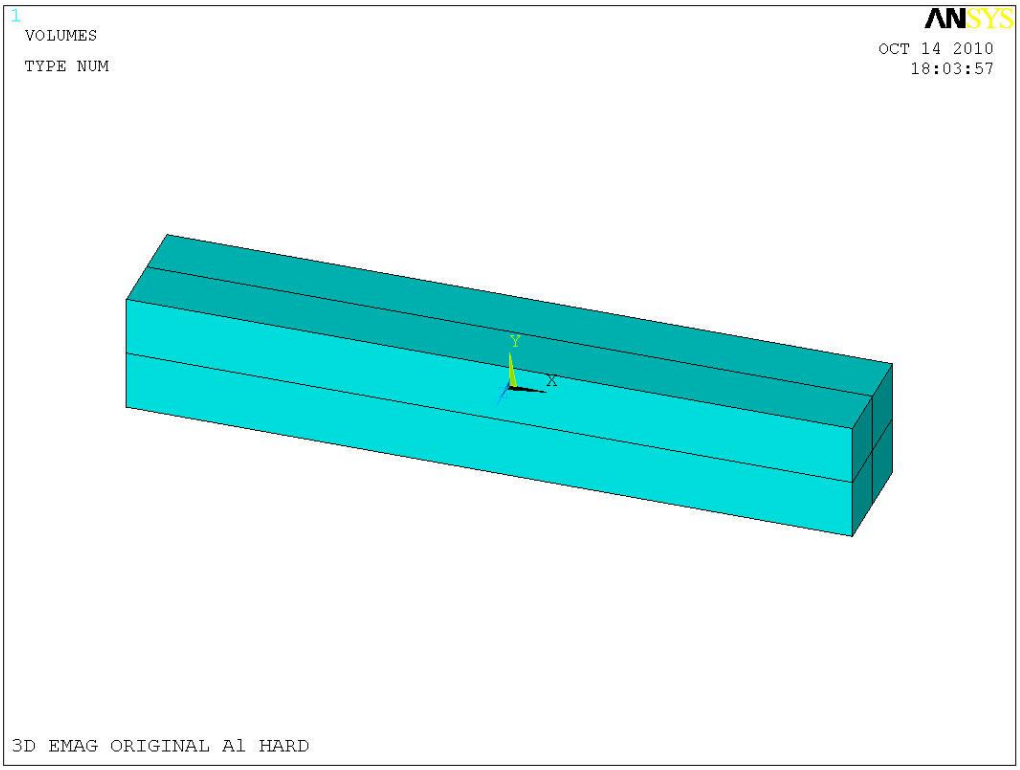

a)

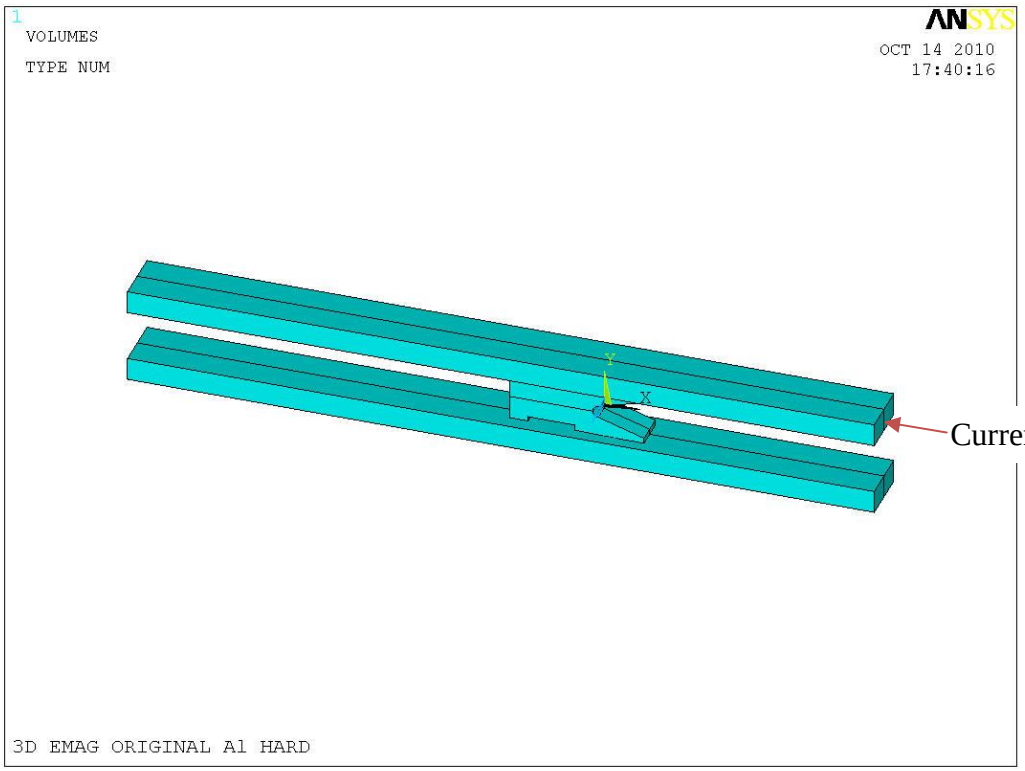

b)

Figure 28. 3-D model used for the electromagnetic FEA a) with air and b) without air

The transient current supplied to the top rail is based on lab-scale EML experimental data. The current curve is shown in Figure 29.

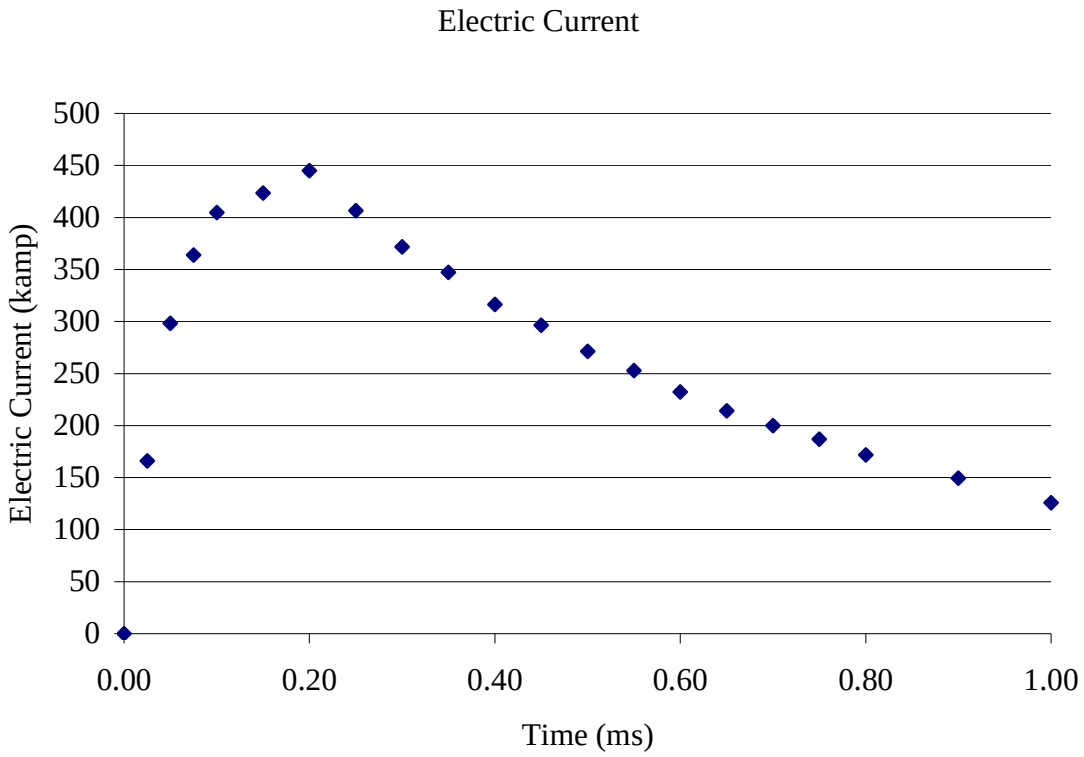

Figure 29. Plot of the applied electric current for the EMAG analysis

For the applied current, it should be noted the current loading can be varied for the lab-scale EML, but this model was chosen as the load to apply because it was used for lab-scale EML experimentation.

Figure 30 and Figure 31 shows the meshed plot of the EML 3-D model. The first plot shows the model encased in the modeled air. The second plot shows the air removed, leaving the upper and lower rails and the armature in between. A finer mesh density is used at the contact interface between the rails and the armature legs as well as the air between the gap.

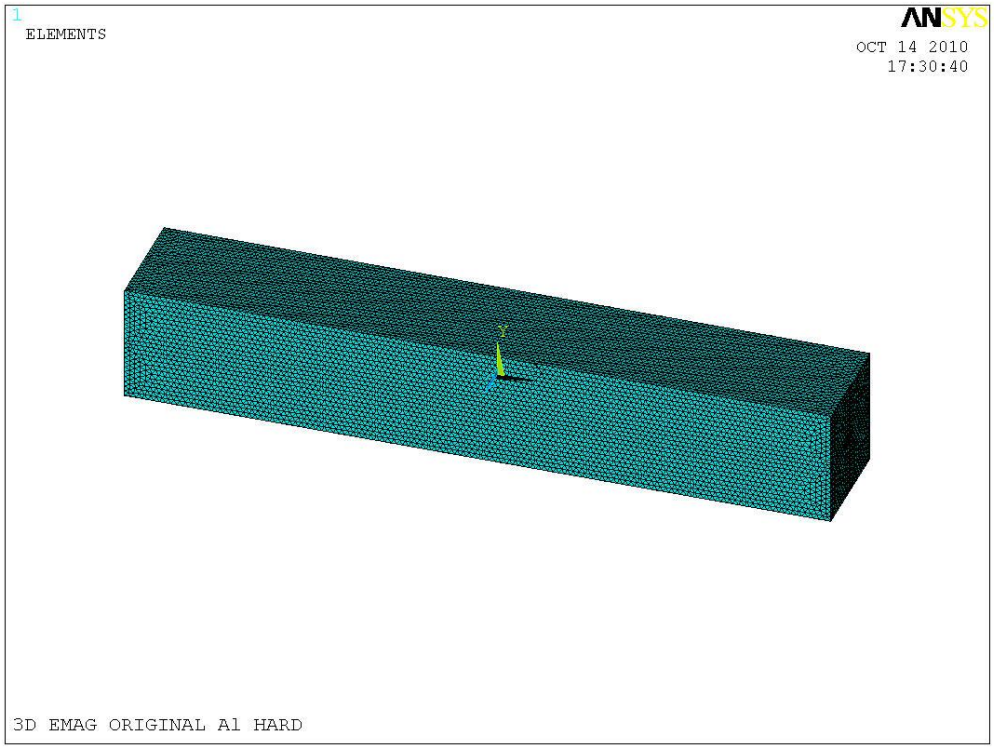

a)

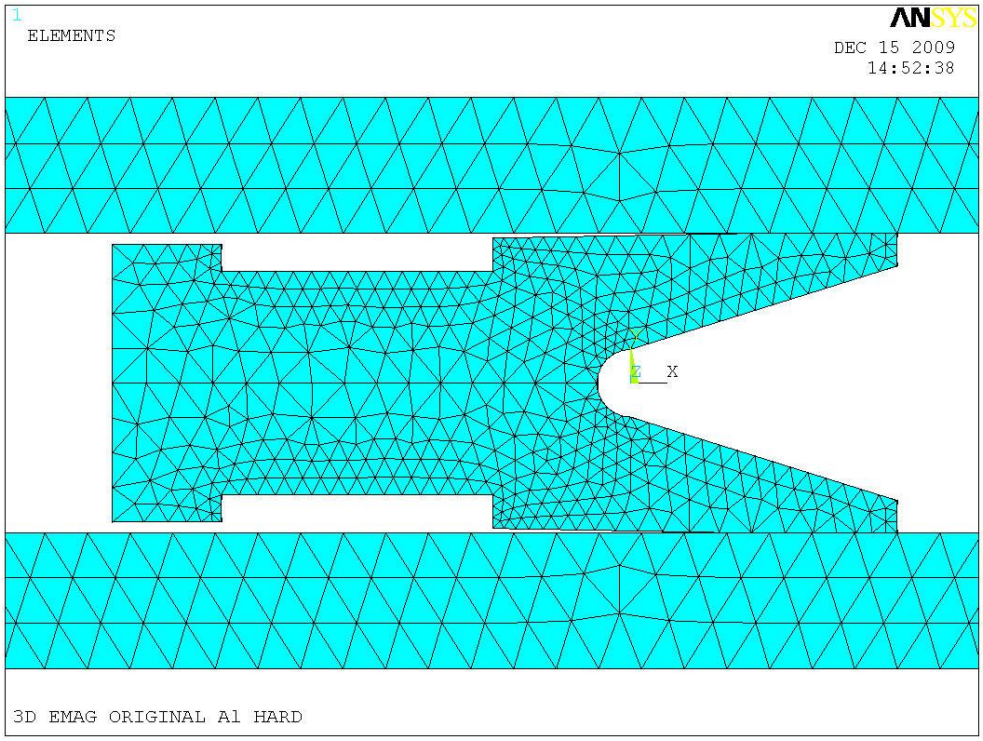

b)

Figure 30. Mesh plot of the 3-D EML model a) with air and b) without air

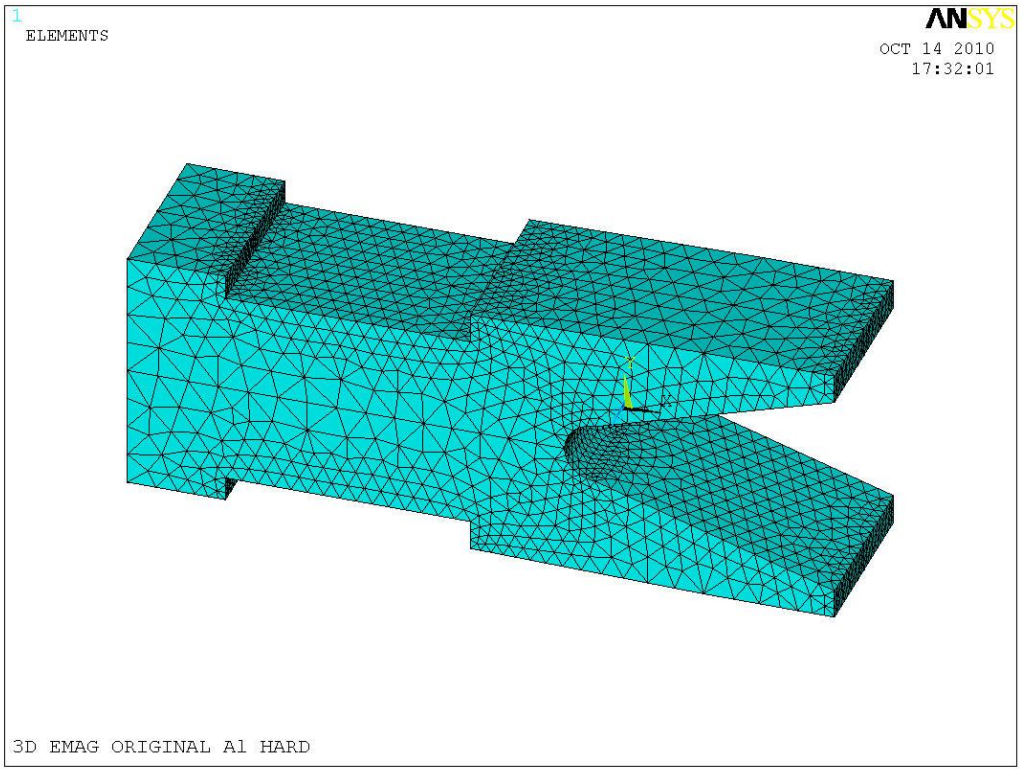

Figure 31. Mesh plot of the 3-D EML armature alone

The element type used in the analysis is Solid 97, which is a 3-D element with eight nodes as shown in Figure 32. The element has magnetic vector potential, time-integrated electric potential, electric potential, electric current, and electromotive force as its degrees of freedom. The element also has thermal capabilities.

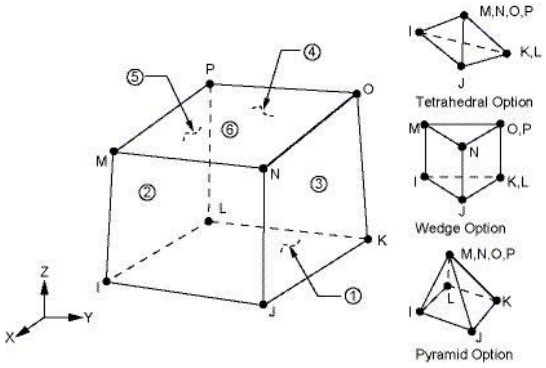

Figure 32. Diagram of the Solid 97 element [29]

4.1.2. Results and Discussion

The EMAG analysis was completed for three conditions: original aluminum armature, modified aluminum armature, and original molybdenum armature. The reason for the limited analysis was due to the amount of time required for the analysis as well as the results themselves. As shown in Table 7, the forces in the x-direction are very similar to each other despite the different parameters. The forces in the y-direction and z-direction are very low relative to the forces in the x-direction and are therefore negligible in this analysis. Also, the x-direction forces are negative due to the coordinate system used in the analysis where the negative x-direction is the desired direction of motion.

Table 7. EMAG forces from the FEA analysis for the three scenarios

Time (ms)	Current (Amps)	Original Aluminum			Modified Aluminum			Original Molybdenum		
		x-direction	*y-direction*	*z-direction*	*x-direction*	*y-direction*	*z-direction*	*x-direction*	*y-direction*	*z-direction*
0.00	0	0.00	0.00	0.00	0.00	0.00	0.00	0.00	0.00	0.00
0.03	165988	-2920.46	1.37	0.60	-2926.42	14.68	-41.40	-2987.04	0.10	-0.03
0.05	298098	-17460.40	13.00	-0.33	-17408.20	29.70	-309.15	-17616.10	8.21	-4.09
0.08	364017	-30977.60	20.67	2.95	-30657.70	11.69	-614.42	-31093.40	19.52	-1.27
0.10	404855	-40495.10	29.70	13.00	-39809.60	9.75	-384.30	-40603.20	28.49	11.69
0.15	423360	-48646.00	47.18	21.68	-47517.00	2.30	-1051.29	-48513.60	42.24	19.84
0.20	444809	-52859.80	55.49	17.43	-51098.40	8.34	-1149.49	-52789.00	43.59	16.87
0.25	406464	-50338.00	52.96	11.64	-48108.20	4.90	-1108.73	-50185.60	40.20	11.25
0.30	371716	-42211.30	40.32	5.51	-39833.00	6.60	-930.46	-42042.50	26.41	7.73
0.35	347224	-36708.30	30.07	3.21	-34052.00	4.91	-797.60	-36637.20	17.46	5.12
0.40	316526	-31613.20	22.65	1.50	-28886.70	2.55	-681.55	-31549.60	11.57	3.80
0.45	296319	-27321.90	15.55	2.17	-24597.50	1.88	-581.60	-27282.10	5.99	4.59
0.50	271350	-23659.80	12.20	1.32	-21033.50	0.79	-499.22	-23626.00	3.99	3.24
0.55	252812	-20362.70	8.33	1.62	-17896.40	0.49	-425.91	-20330.80	1.23	3.67
0.60	232381	-17584.70	6.60	1.13	-15303.10	0.04	-364.90	-17558.30	0.60	2.70
0.65	214269	-14999.70	4.46	1.11	-12939.10	-0.09	-309.57	-14968.90	-0.75	2.72
0.70	200041	-13003.90	3.53	0.84	-11131.70	-0.33	-266.07	-12985.70	-0.86	2.11
0.75	186802	-11384.30	2.61	0.87	-9690.73	-0.51	-231.90	-11367.80	-1.27	2.09
0.80	171794	-9814.00	2.05	0.69	-8315.20	-0.51	-199.37	-9794.24	-1.88	1.68
0.90	149369	-7631.23	1.11	0.49	-6415.35	-0.40	-154.19	-7612.76	-1.48	1.35
1.00	125828	-5623.42	0.66	0.22	-4695.81	-0.41	-113.11	-5606.37	-1.15	0.80

The electric current generates forces in the x-direction as high as approximately 50,000 N. Theoretically, the forces in the y-direction and x-direction should sum to zero due to the symmetric nature of the system. The x-direction EMAG force generation occurs in the legs of the armature. Figure 33 shows the iso-surface contour plots of the EMAG forces for the original aluminum armature.

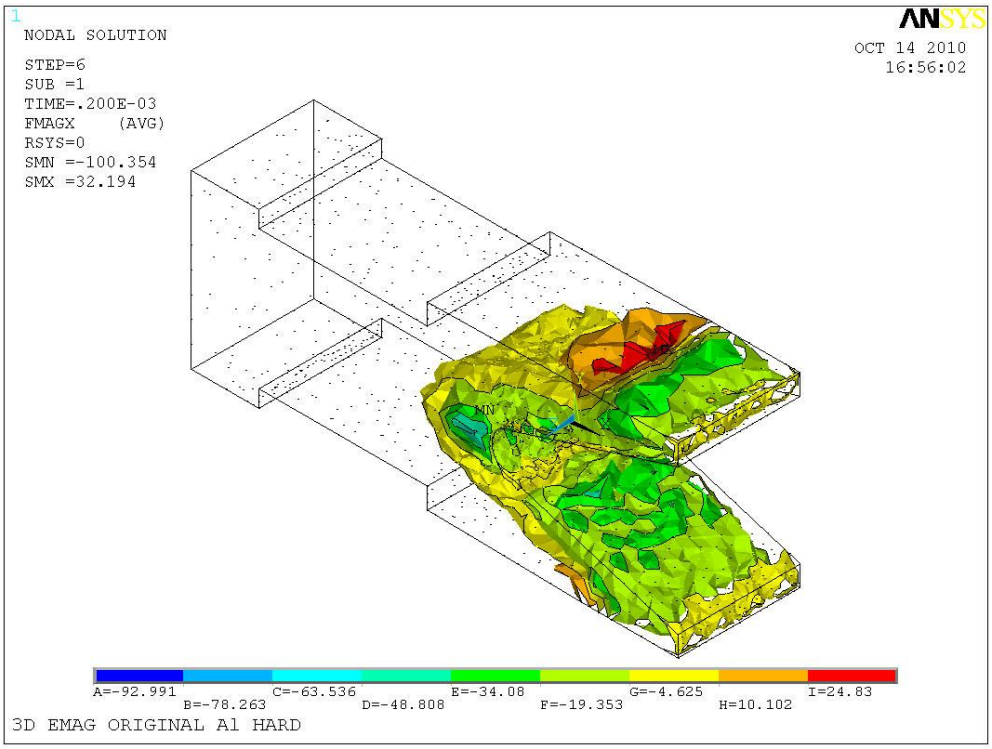

a)

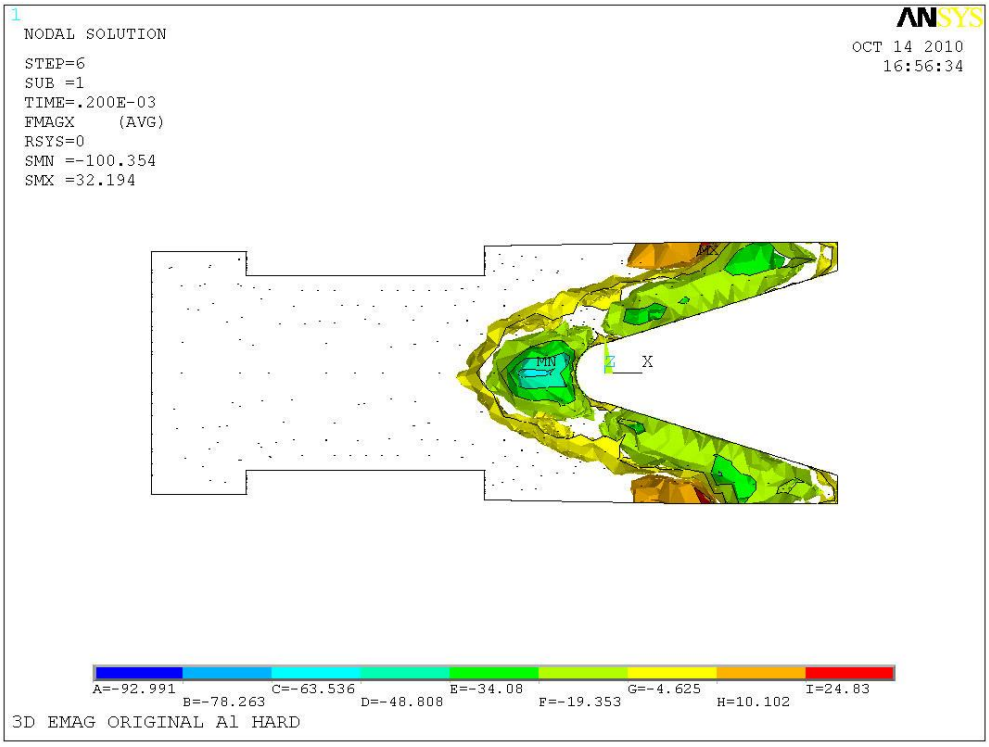

b)

Figure 33. a) Overall and b) side iso-surface contour plot of the EMAG forces in the x-direction for the original aluminum armature

While there are positive values for forces in the legs of the armature, the magnitude is much smaller than the forces in the negative x-direction. Therefore, the armature would still travel in the desired direction which is the EML barrel exit.

The y-direction EMAG forces are shown in the iso-surface contour plots in Figure 34. As it was for the x-direction forces, the y-direction forces are also in the legs. The upper leg has more positive value forces while the lower leg has more negative value forces. This causes the legs to separate from each other which has been observed in the lab-scale model. Also, this is a desired force direction because it helps the armature maintain contact with the rails. As stated before, the y-direction forces should sum to zero but the difference in magnitude can be attributed to rounding errors in the FEA or insufficient meshing.

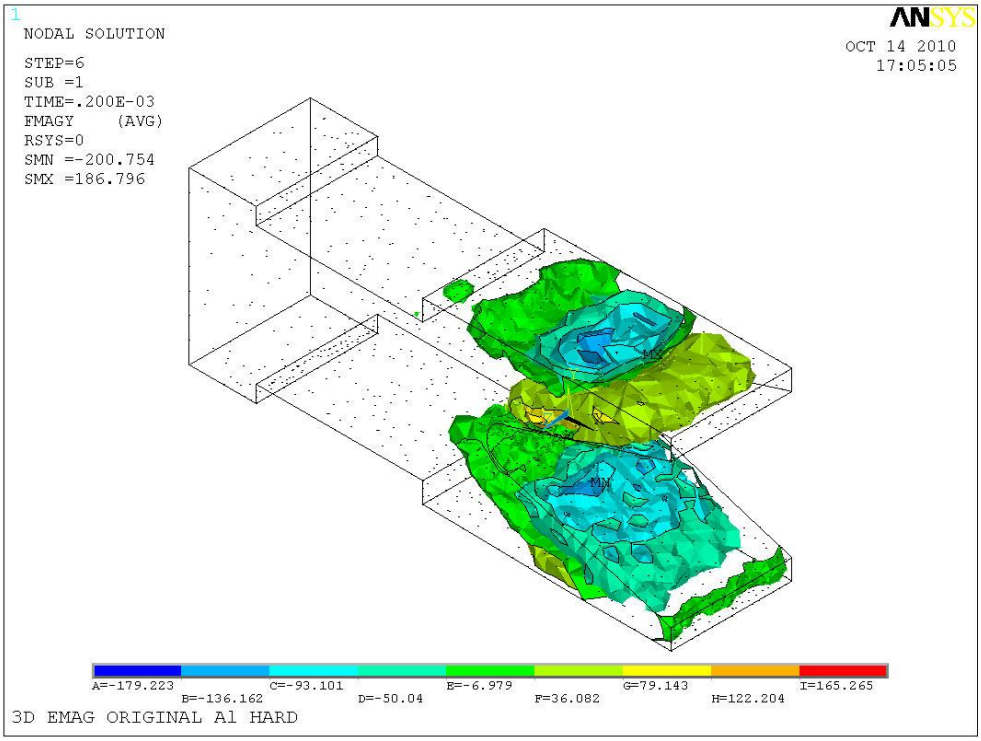

a)

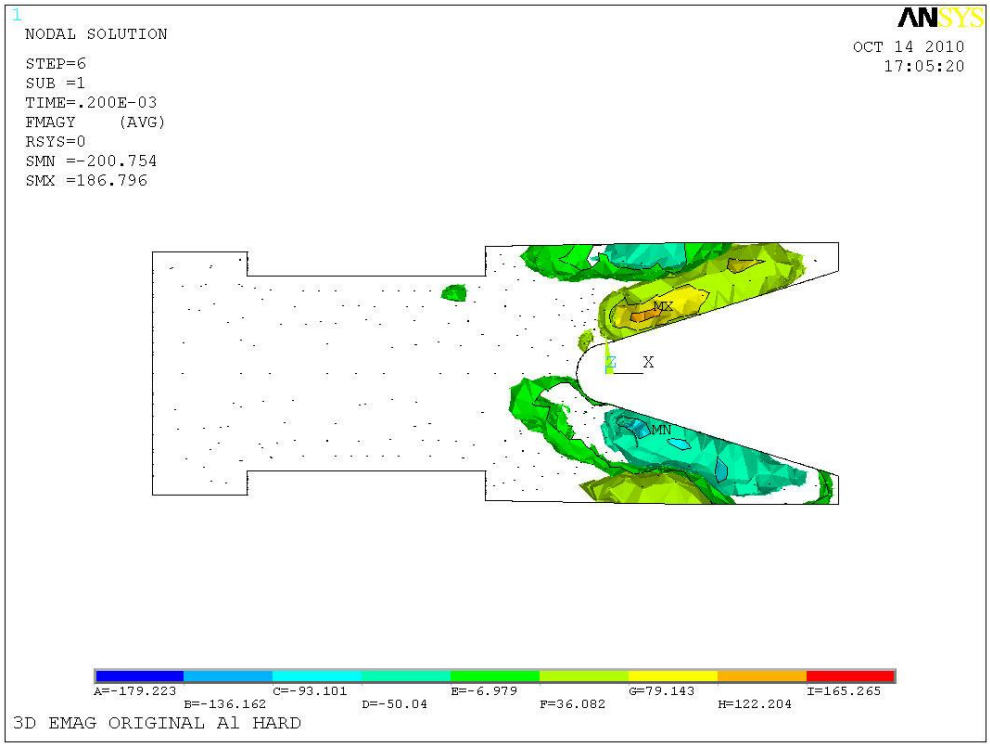

b)

Figure 34. a) Overall and b) side iso-surface contour plot of the EMAG forces in the y-direction for the original aluminum armature

The z-direction EMAG forces in the original aluminum armature are observed in the iso-surface contour plots shown in Figure 35. As evidenced in the plots, the z-direction forces tend to act on the sides of the armature. The forces create a tensile stress in the armature pulling the sides outward. Again, the imbalance in the magnitude of the forces is a result of rounding errors in the FEA or insufficient meshing.

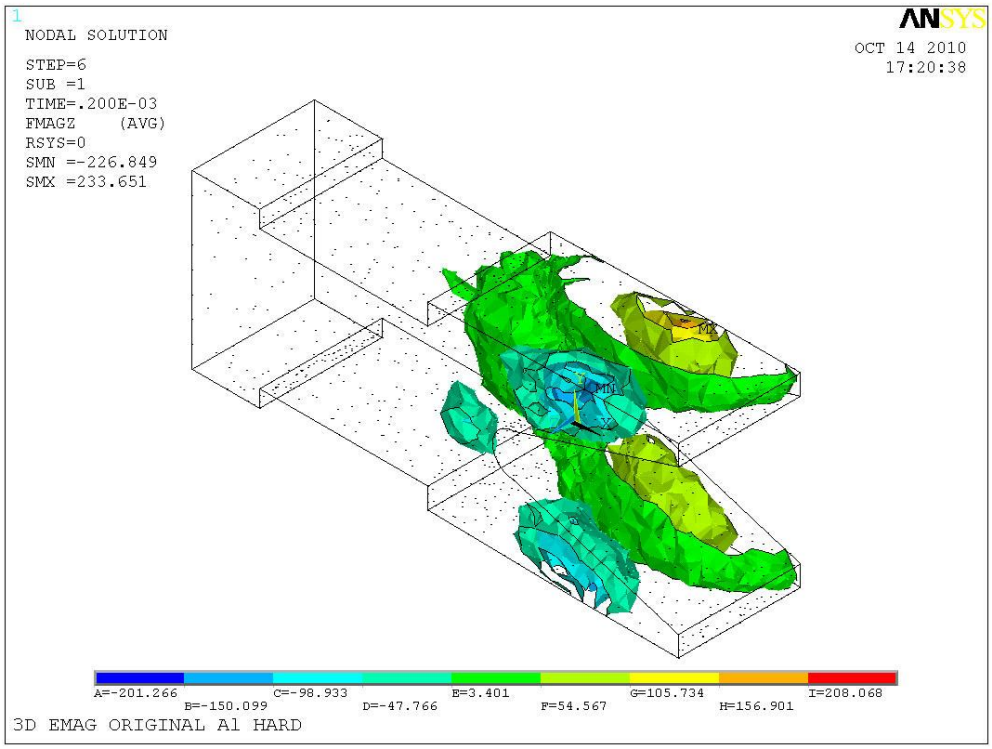

a)

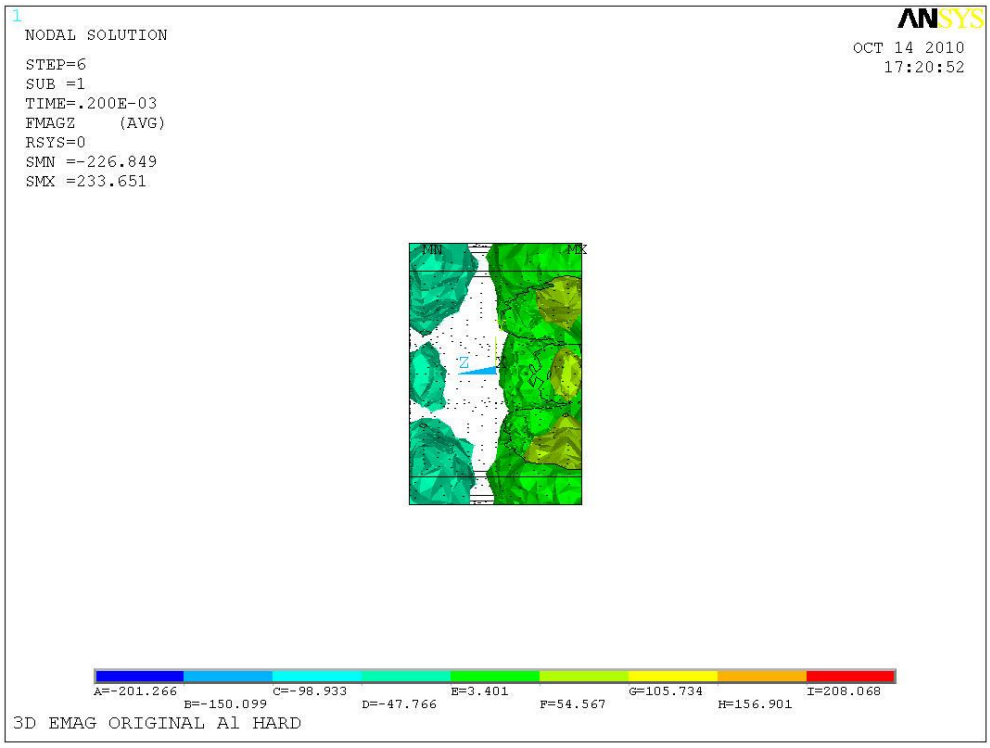

b)

Figure 35. a) Overall and b) side iso-surface contour plot of the EMAG forces in the z-direction for the original aluminum armature

Using the forces from Table 7 and Newton's second law of motion, the velocity and displacement can be estimated for each parametric condition. Equation 4.2 shows the basic principle of calculating the velocity and displacement.

$$\vec{F} = \frac{d}{dt} m\vec{v}_{arm} \tag{4.2}$$

where

$\vec{F} =$ EMAG force [N]

$m =$ mass of the armature [kg]

$\vec{v}_{arm} =$ velocity of the armature [m-s^{-1}]

The theoretical mass is determined using the density and volume. Finally, an exit time from the barrel is estimated using Equation 4.2. The frictional forces between the rail and armature were excluded.

4.1.2.1. Design Comparison

The speed is calculated by integrating Equation 4.2 once and the displacement is found by integrating again. The speed and displacement of the original and modified aluminum armature designs are shown in Figure 36 and Figure 37, respectively. Both simulations were conducted at the lab-scale interference.

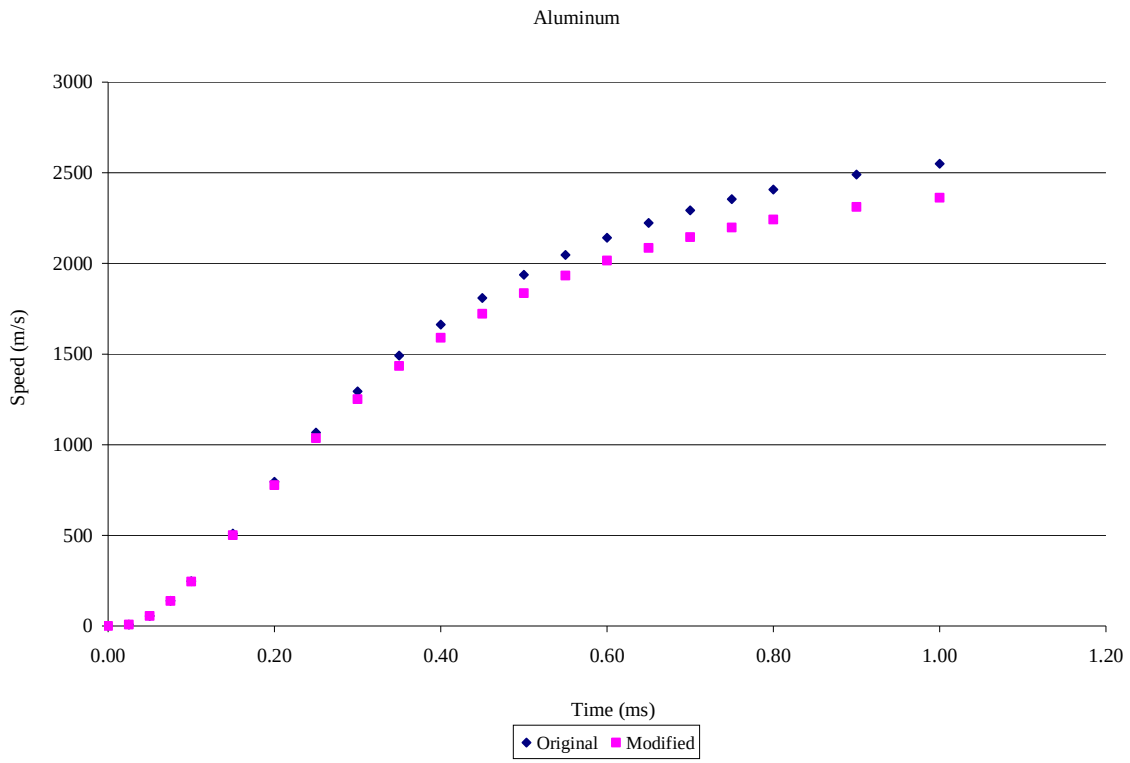

Figure 36. Speed of the original and modified aluminum armature designs

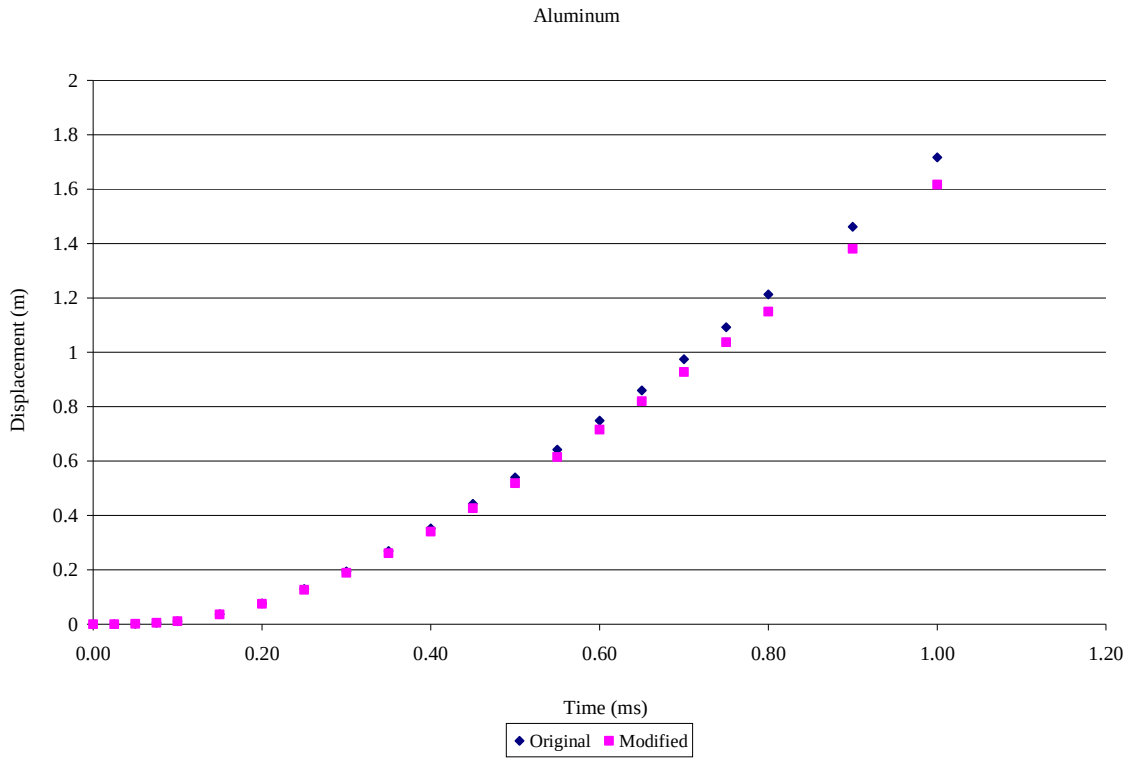

Figure 37. Displacement of the original and modified aluminum armature designs

From Figure 36, it is apparent that the original design reaches greater speeds than the modified design but not by much. The original design reaches a maximum speed of $v = 2550.36$ m/s while the modified design reaches a maximum speed of $v = 2362.06$ m/s which is only a 7.38% relative difference. The possible difference in speed is due to the difference in EMAG forces. The EMAG forces in the x-direction were consistently higher in the original design than the modified design. Because the original design reaches a higher speed faster than the modified design, it also displaces along the rails faster as evidenced in Figure 37. The calculated displacement of the original design, while under the current load, is $x = 1.717$ m, while the displacement of the modified design is $x = 1.617$ m. That is a 5.82% relative difference.

The possible reason for the better speed and displacement in the original design could be due to the slight difference in the designs. Since the modified design decreases the angle of inclination of the leg, there is more contact area for the current to pass through. By changing the contact area, the current density changes which affects the EMAG forces. As stated in Equation 4.1, the Lorentz force is dependent on the speed and direction of the current. Differences can also be attributed to a different mesh of the volumes. Because the volumes are different, the exact same mesh cannot be used and in an intensive FEA simulation, rounding errors can accumulate.

From Figure 37, a trend line is used to determine the approximate exit time of the armature from the barrel for the lab-scale EML and experimental current curve. The trend line determined from Figure 37 is shown in Equation 4.3a (original) and 4.3b (modified).

$$x = -1.134t^3 + 3.003t^2 - 0.145t \qquad 4.3a$$

$$x = -1.113t^3 + 2.872t^2 - 0.125t \qquad 4.4b$$

where

$x = \text{displacement [m]}$

$t = \text{time [ms]}$

These equations only apply for the case of the lab-scale EML and given the conditions for this simulation. Assuming that the armature travels the full 1.5 m of the EML barrel, the estimated exit time for the original armature is $t = 0.9099$ ms and $t = 0.9418$ ms for the modified armature.

4.1.2.2. Material Comparison

For the material comparison, not all the materials were analyzed. Only the aluminum and molybdenum original armatures are presented. The reason was, again, because of complexity and the time required for each analysis. Also, as shown in Table 7, the forces were very similar between the aluminum and molybdenum armatures. Therefore, it was assumed that all materials would perform with approximately the same EMAG forces and was confirmed with an analysis of the niobium armature which showed the same results as the aluminum and molybdenum armatures.

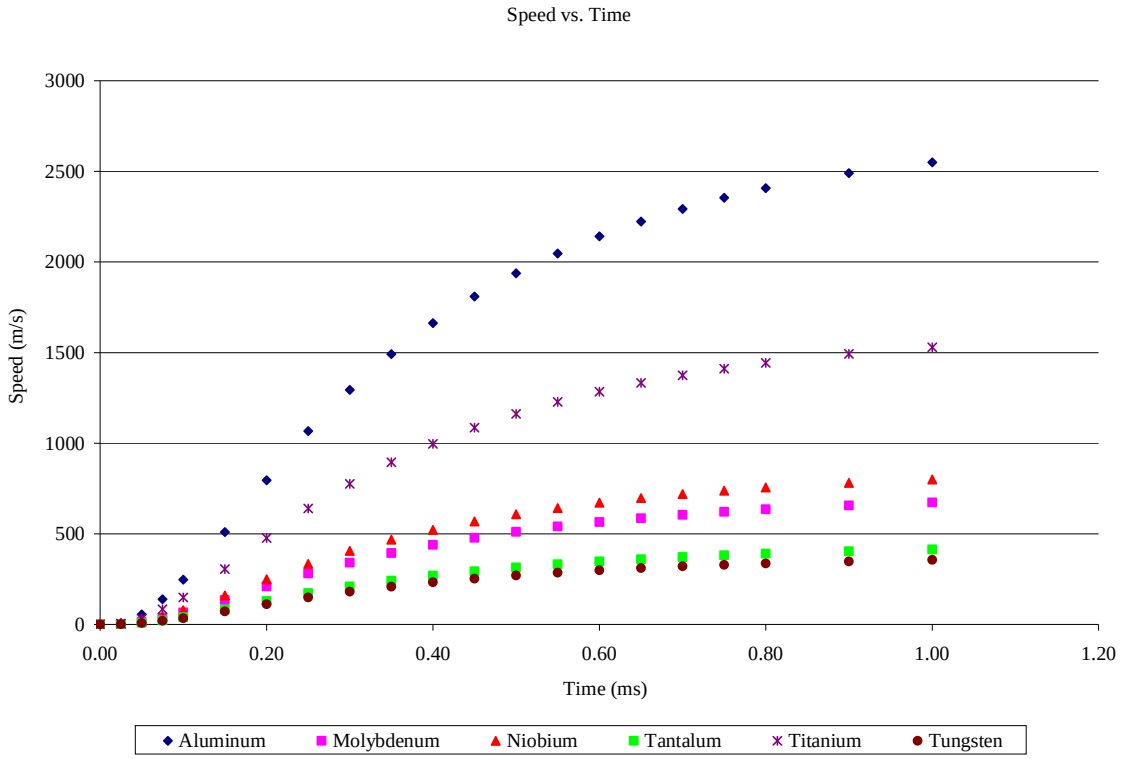

Figure 38. Speed of the original armature designs

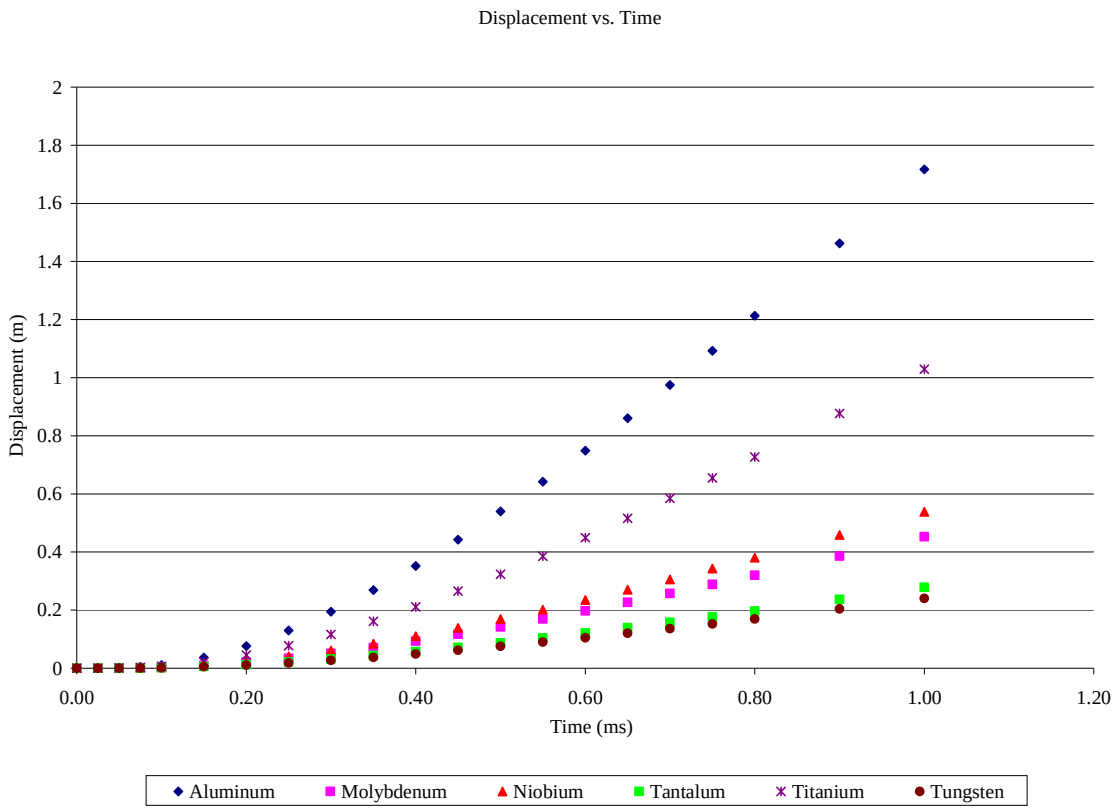

Figure 39. Displacement of the original armature designs

From Figure 38, the speeds of the different material armatures vary as time progresses. Figure 39 shows the corresponding displacement for each material armature analyzed and, like the speed, it varies with time. Each armature varies proportionally to the density of the armature material. Because the forces are approximately equal, as well as the armature design, the accelerations for each armature varies. Table 8 summarizes the velocities and displacements expected to occur during the duration of the applied current. According to Table 8, the aluminum armature obtains the highest speed and displacement, while the tungsten performs the poorest. These results are consistent with a constant force and the aluminum/tungsten armature having the lightest/heaviest mass.

Table 8. Summary of maximum velocities and displacements for each material armature

Armature Material	Velocity Max (m/s)	Displacement Max (m)	Rank
Aluminum	2550	1.72	1
Molybdenum	672.7	0.453	4
Niobium	800.1	0.539	3
Tantalum	413.3	0.278	5
Titanium	1529	1.03	2
Tungsten	356.5	0.240	6

In these simulations, the forces are likely very similar to each other due to the material resistance being very low for each material. Due to the very low resistivity and short travel distance, the current distribution is likely very similar for each material. The slight variation in the values can be attributed to the different resistivities. As before, rounding errors can also attribute to the variations.

For the exit times of the different material armatures, because the forces are very similar and mass dependent, the denser material (tungsten) performs the poorest, while the lightest material (aluminum) performs the best. This applies to both the original design and the modified design for each material. The following is a summary of results from the EMAG analysis:

1. The x-direction forces experienced in the original design armature are higher than the forces experienced in the modified design armature. This is likely due to the increased contact area for the current to travel through in the modified design which can affect the current distribution.
2. Due to the difference in mass for the armatures of each material and the consistent current density, a lighter armature should be chosen to increase speed capabilities.
3. The exit of the armature from the EML barrel, solely from EMAG forces, is $t = 0.9099$ ms for the original design armature and $t = 0.9418$ ms for the modified design armature.

4. The friction forces that would occur at the lab-scale interference are very low based on the normal force applied by the initial contact. The friction force is two orders of magnitude smaller when compared to the EMAG forces the armature experiences.

The exit time of the armature calculated in the EMAG analysis can be used in the modal analysis to determine if intermittent contact is possible. In terms of the thermal aspect of the EML, the exit time determines whether melting occurs before the armature leaves the barrel.

CHAPTER 5: THERMAL ANALYSIS

The focus of this chapter is on two separate thermal analyses. The first section of this chapter develops a range of values used by the FEA program in the thermal analyses. These values are estimations of what the thermal and electric conductance is at the contact interface. The effects of friction heating from the high velocities are investigated in the following section. The last section focuses on the effects of Joule heating caused by the high current used in the lab-scale EML.

5.1. Electrical and Thermal Contact Conductance

For a thermal analysis using ANSYS, a contact pair must be defined to give appropriate contact characteristics between two materials. In this case, the contact pair is between the rail and armature and uses the elements CONTACT 172 and TARGET 169. The contact pair accepts a value for electrical contact conductance (ECC) and thermal contact conductance (TCC). The values simulate the effects of surface roughness on the electrical conductance and thermal conductance between the two materials. If the two materials were completely smooth and a perfect contact was made, the conductance values would be very high, meaning very low resistance. However, realistically, the surface roughness between the materials causes there to be a drop of voltage and temperature across the contact.

5.1.1. Electrical Contact Conductance

The surface roughness of the two materials causes a voltage drop across the contact because the voltage can only travel through the asperities. Equation 5.5 4.2 calculates the theoretical ECC [S-m^{-2}] value [29].

$$ECC = \frac{\sigma_c}{d} \qquad 5.5$$

where

σ_c = average electrical conductivity [S-m^{-1}]

d = planar thickness or depth into page [m]

However, because this equation does not account for surface roughness, resistance measurements were taken using an experimental setup. The underlying principle of the setup is that the material resistance is much lower than the contact resistance. By measuring the voltage drop between the rail and the armature and comparing to the voltage supply, a resistance can be estimated which correlates to the contact resistance. Because ECC should vary with respect to the contact asperities, the voltage drop is measured as the interference increases giving an idea of how the resistance will be affected with respect to interference. Also, voltage drops for different metal (aluminum and steel) armatures were measured to estimate the effect of material properties on the ECC. A basic schematic of the experimental setup is shown in Figure 40. A summary of the results is shown in Figure 41 that shows the ECC value versus interference for the aluminum and steel armatures on the copper rails.

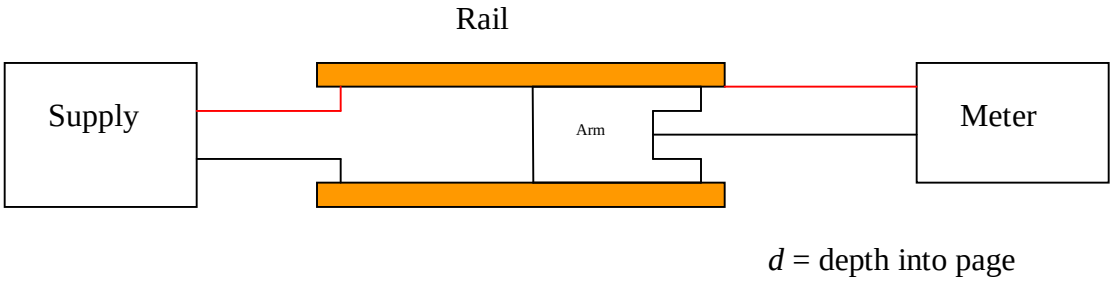

Figure 40. Basic schematic of experimental setup to determine ECC

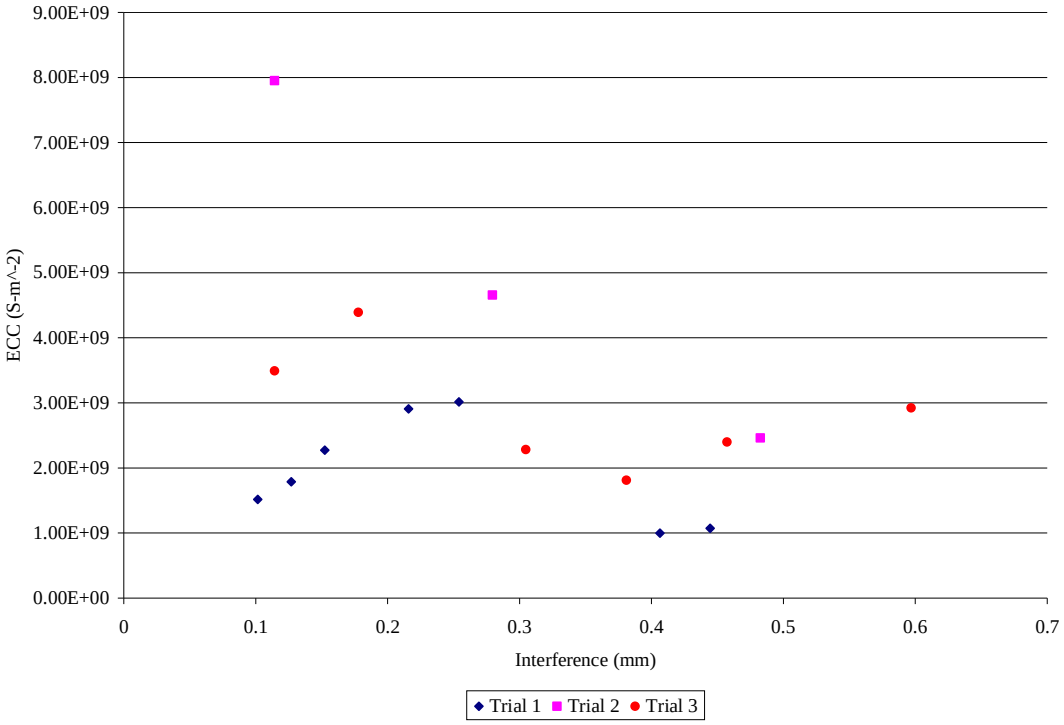

a)

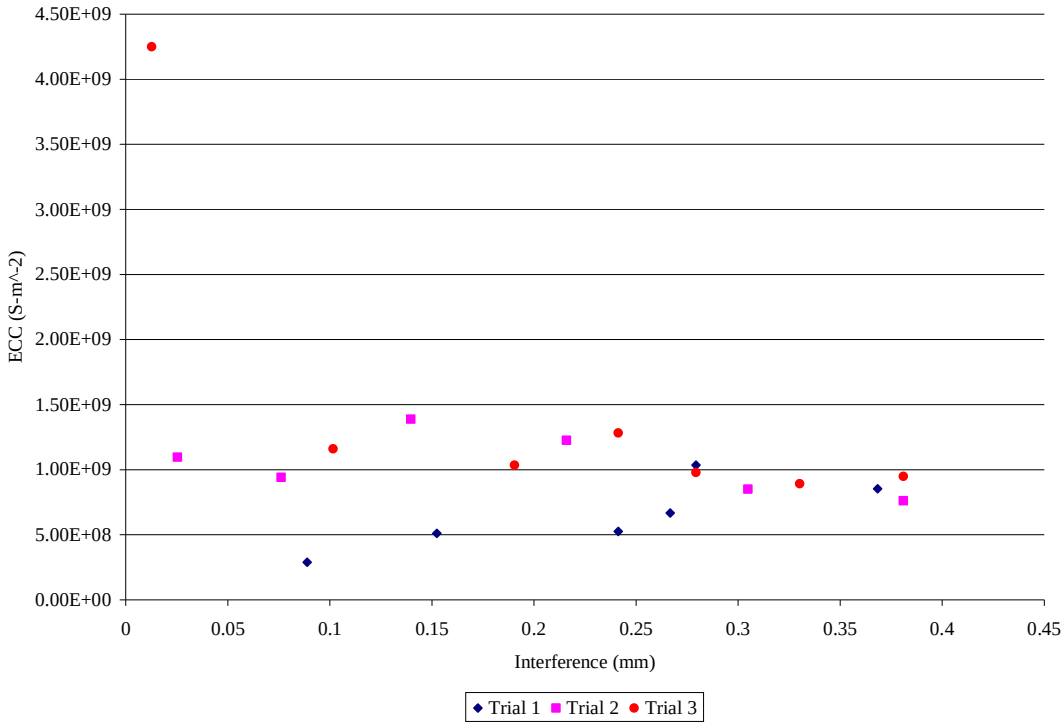

b)

Figure 41. Plot of ECC versus interference for a) aluminum and b) steel on copper

From Figure 41, ECC values are approximately on the order of magnitude of 10^8 to 10^9 for both metals. Therefore, it was assumed that all metals would perform in the same manner with an average ECC value of 2.00E+09 S-m^{-2}.

5.1.2. Thermal Contact Conductance

A previous study, conducted by Yeh and Lin [30], resulted in an equation to approximate thermal contact resistance which is the inverse of TCC. Equation 5.6 expresses the relationship between material properties, contact pressure, and the thermal contact resistance.

$$\frac{\Omega_c k_m}{\left(R_c / \tan\theta_c\right)} = 1.08 \bullet 10^{-8}\left(\frac{P_c}{E'}\right)^{-3.0} \qquad 5.6$$

where

Ω_c = thermal contact resistance [°K/W]

$k_m = \dfrac{2k_{mat}k_{cu}}{\left(k_{mat}+k_{cu}\right)}$ = average thermal conductivity [W/m^2-°K]

$R_c = \sqrt{R_{mat}^2 + R_{cu}^2}$ = combined surface roughness [m]

$\tan\theta_c = \sqrt{\tan\theta_{mat}^2 + \tan\theta_{cu}^2}$ = combined absolute asperity slope [rad]

P_c = contact pressure [Pa]

$\dfrac{1}{E'} = \dfrac{1-\nu_{mat}^2}{E_{mat}} + \dfrac{1-\nu_{cu}^2}{E_{cu}}$ = combined modulus of elasticity [Pa]

mat = material of interest

Absolute asperity slope is average surface roughness of the asperities of a material. Because the surface roughness and absolute asperity slope was not known for

all the materials, that parameter was kept at the same value for each material. Also, it should be noted that from a previous study done by Chen et al. [10], it was shown that because the magnitude of the current passing through the system in such a short time, Joule heating is the more contributing source of melting than friction heating. This means that the ECC is a more contributing property than the TCC because the ECC is current calculated while the TCC is thermal property calculated. Table 9 shows the averaged and combined material properties used to calculate the TCC for each armature to rail pairing.

Table 9. Average and combined material properties used in TCC calculations

Armature Material	**k_m (W/m^2-K)**	**R_c (m)**	**tan θ_c**	**E' (GPa)**
Aluminum	233.3	1.253E-06	0.2062	49.30
Molybdenum	203.5	1.253E-06	0.2062	99.32
Niobium	92.15	1.253E-06	0.2062	10.76
Tantalum	95.39	1.253E-06	0.2062	82.87
Titanium	32.57	1.253E-06	0.2062	66.79
Tungsten	229.7	1.253E-06	0.2062	103.6

Table 10 is a summary of the TCC values calculated depending on the material, design, and compliance layer. From the tables, the TCC values change very little between the hard and soft compliance layers. Between designs, there is a higher change in TCC because of the differences in contact pressure. For every material and both compliance layers, the modified designs have lower TCC values than the original designs of that same material and compliance layer. These values are used for the thermal FEA when attributing factors to the contact pair between the armature and rail.

Table 10. Contact pressures and TCC values for the original and modified designs with the a) hard and b) soft compliance layers

a)

Armature Material	Original Design		Modified Design	
	Contact Pressure (GPa)	***TCC (W/°K)***	***Contact Pressure (GPa)***	***TCC (W/°K)***
Aluminum	0.215	2.97E+08	0.0803	1.54E+07
Molybdenum	0.626	7.78E+08	0.259	5.48E+07
Niobium	0.252	1.80E+10	0.104	1.25E+09
Tantalum	0.423	1.94E+08	0.179	1.46E+07
Titanium	0.365	8.10E+07	0.0532	2.51E+05
Tungsten	0.631	7.90E+08	0.0790	1.55E+06

b)

Armature Material	Original Design		Modified Design	
	Contact Pressure (GPa)	***TCC (W/°K)***	***Contact Pressure (GPa)***	***TCC (W/°K)***
Aluminum	0.225	3.37E+08	0.0728	1.14E+07
Molybdenum	0.550	5.27E+08	0.249	4.87E+07
Niobium	0.258	1.93E+10	0.102	1.20E+09
Tantalum	0.409	1.75E+08	0.182	1.54E+07
Titanium	0.260	2.94E+07	0.118	2.74E+06
Tungsten	0.710	1.13E+09	0.291	7.76E+07

5.2. Friction Heating Analysis

The friction heating analysis was not done with FEA but by formulaic estimation. As stated before, the EMAG analysis produced the same EMAG forces despite differences in contact area because of the forced current. Therefore, in order to compare the materials and designs, estimations were made on the velocity the armature could reach before melt-wear occurred. These calculations do not take into account any EMAG forces.

Based on the principle of power being force times velocity [31] and by knowing the contact pressure, P_c, associated with each design, material, and compliance layer, the armature velocity, V_m, at which melt-wear occurs due to friction, was estimated from Equation 5.7 as shown below

$$V_m = \frac{Q}{\mu P_c A} \tag{5.7}$$

where

$Q =$ power dissipated to overcome friction [W]

$\mu =$ coefficient of friction

$P_c =$ contact pressure [Pa]

$A =$ contact area [m^2]

The coefficient of friction is determined from Bansal and Streator's work [32] where the coefficient of friction between copper and the other materials was determined to average at approximately 0.35. The contact pressure and areas are from the previous structural results using the maximum contact pressure criterion.

Equation 5.8 estimates Q based on common conduction heat transfer principles as shown in [33].

$$\eta Q = \frac{kA}{L}(T_m - T_0) \tag{5.8}$$

where

$\eta =$ heat partition value

$k =$ thermal conductivity [W/m^2-°K]

$A =$ contact area [m^2]

$L =$ penetration depth [m]

$T_m =$ melting temperature of armature material [°K]

$T_0 =$ ambient temperature [°K]

The penetration depth was assumed to be $L = 1.00\text{E-}04$ m which was an estimated value of how much the heat would penetrate into the material. The heat partition value is based on Jaegar's work [34] and represents the percentage of heat entering an armature

depending on armature speed. From the study, it was found that percentage of heat entering the armature, η, ranges from 3% to 45%, with the former associated with relative velocities on the order of 10^3 m/s or more. The latter generally occurring when the contacting bodies are stationary or moving at relative velocities on the order of 100 m/s. By using linear interpolation and the range for the heat partition, the velocities were found by combining Equation 5.7 and Equation 5.8 into

$$V_m = \frac{k}{\eta \mu P_c L}\left(T_m - T_0\right) \tag{5.9}$$

5.2.1. Results and Discussion

By using different values for the heat partition to calculate the possible melt-wear velocities and comparing to the linear interpolation of the heat partition ranges from the previous study, it was found that all the armatures (both designs, all materials, and both compliance layers), except two cases, would perform with a velocity less than 100 m/s. Therefore, a standard heat partition value of 45% was used for all melt-wear velocity calculations except for the one exception. The first exception was the lab-scale interference of the aluminum armature and modified design. The velocity was between 100 and 1000 m/s and so an interpolation was used to determine the correct heat partition. An example of two cases is shown in Figure 42. As seen in the first plot, the velocity for the modified tungsten armature with a hard compliance layer reached a velocity greater than 1000 m/s and was, therefore, given a heat partition value of 3%. The second plot shows the intersection of the velocity using different heat partitions with the linear interpolation. The lower velocity and heat partition is chosen in this case because the velocity before melting is desired and according to the data, the armature would first melt at the lower velocity. The calculations were completed for the lab-scale half-interference as well as the interference using the maximum contact pressure criterion.

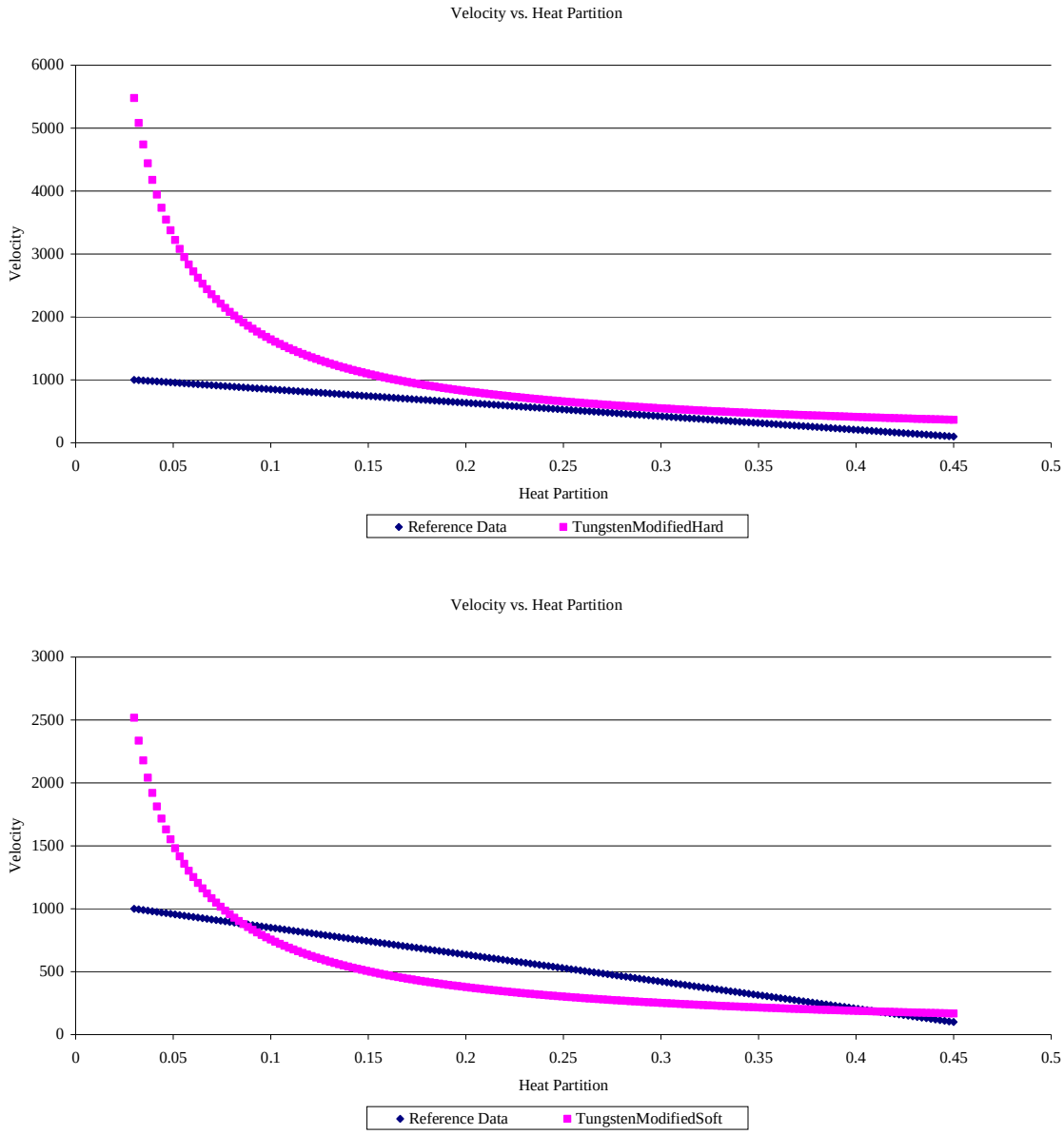

Figure 42. Plot of heat partition interpolation and determination for two cases

All results given in the following sections are for the macro-scale system and do not take into account any micro-scale mechanics.

5.2.1.1. Design Comparison

A summary of the melt-wear velocities for the lab-scale half-interference, along with the contact pressures, is shown in Table 11.

Table 11. Melt-wear velocities for the original and modified designs with the hard and soft compliances at the lab-scale half-interference

	Contact Pressure (GPa)	**Velocity (m/s)**	**Rank**
Original Hard	0.211	26.03	4
Original Soft	0.201	27.31	3
Modified Hard	0.0326	184.1	1
Modified Soft	0.0584	93.87	2

Table 11 shows that between designs, the modified design is more optimal as it increases the melt-wear velocity. There is an increase in melt velocities from the original design to the modified design for both compliance layers. The case with the harder compliance layer show a larger increase in speed where the velocities go from 26.03 m/s to 184.1 m/s. In this case, the increase is attributed more to the difference in heat partitions used. Because the modified design is capable of reaching higher speeds, the amount of heat entering the armature is lower. The low contact pressure also reduces the amount of friction acting between the armature and rail, which increases the capable speed before melting.

Table 11 shows that the best velocity result is the modified design with the hard compliance layer with a $V_m = 184.1$ m/s versus the worst velocity of $V_m = 26.03$ m/s for the original design with the hard compliance layer. For this situation, the difference in the velocities is a result of the contact pressure. The modified design had a much lower contact pressure as a result of the contact length being much higher. Since the contact

pressure is inversely proportional to the melting velocity according to Equation 5.9 it increased the melting velocity.

Between the compliance layers, for the original design, the better choice is the softer compliance layer but not by much. However, for the modified design, the better choice is the harder compliance layer. This was again due to the contact pressure for each case. For the original design, the hard compliance layer resulted in a higher contact pressure, while, for the modified design, the soft compliance layer resulted in a higher contact pressure.

5.2.1.2. Material Comparison

Table 12 expresses the results of both designs and compliance layers using the maximum contact pressure criterion interferences.

Table 12. Melt-wear velocities for the original and modified designs with the a) hard and b) soft compliance layers

a)

Armature Material	**Original Design**		**Modified Design**	
	Velocity (m/s)	***Rank***	***Velocity (m/s)***	***Rank***
Aluminum	25.43	4	68.25	3
Molybdenum	29.63	2	71.74	2
Niobium	26.39	3	64.15	4
Tantalum	19.86	5	47.06	5
Titanium	3.986	6	27.34	6
Tungsten	45.74	1	5478	1

b)

Armature Material	**Original Design**		**Modified Design**	
	Velocity (m/s)	***Rank***	***Velocity (m/s)***	***Rank***
Aluminum	24.38	4	75.27	2
Molybdenum	33.74	2	74.62	3
Niobium	25.77	3	65.10	4
Tantalum	20.55	5	46.19	5
Titanium	5.590	6	12.32	6
Tungsten	40.63	1	99.12	1

When comparing the materials to each other, the optimal choice is tungsten for all the designs and compliance layers. In all cases, titanium is the poorest choice in metal. In

general, the modified design resulted in higher melt-wear velocities than the original design. In most cases, between compliance layers, the velocities were approximately the same except for the modified design of the tungsten armature. The hard compliance layer with that armature had a $V_m = 5478$ m/s because it used a low heat partition of 0.03.

Overall the best result is the modified design of the tungsten armature using a harder compliance layer with a melt-wear velocity of $V_m = 5478$ m/s. The original design of the titanium armature using the harder compliance layer is the overall worst result with a value of $V_m = 3.986$ m/s. While it is known that a speed of 5478 m/s is unrealistic, the interpretation of the data is that tungsten is a better choice with regards to friction heating. These results are influenced by thermal conductance values. Tungsten has a high thermal conductance allowing for faster thermal distribution while titanium has the lowest thermal conductance

5.3. Joule Heating Analysis

As shown in the previous study done by Chen et al. [10], the most influential factor in melting is the Joule heating caused by the high current used in launching the armature. The high current values used must pass through the small contact area in armature-to-rail interface creating a very high current density which causes a large increase in the interface temperature. This analysis determines the time and location where the melting starts due to Joule heating and the effects of material choice, armature design, and compliance layer stiffness.

5.3.1. Geometry, Meshing, Boundary Condition, and Element

The analysis was completed for two different conditions as it was done in the structural analysis. The first condition is the lab-scale half-interference. These results represent what is currently happening in the lab-scale launcher in terms of Joule heating. The second condition is for the maximum contact pressure criterion interferences. This

allows a comparison of materials and designs. Both analyses conditions were completed for the hard and soft compliance layers. The Joule heating analysis does not take into account any structural properties or thermal dependent properties.

The FEA model was created by determining the contact length from the structural analysis. Then the amount of interference needed by displacing the rail in the downward direction, without deformation of the armature, to accomplish the contact length was calculated. The model was considered symmetric and only half of the launcher was modeled. Also, the analysis was quasi-static with the system being stationary and the current being the only time dependent loading. The same current curve used in the EMAG analysis was applied at the end of the top rail, while a voltage of zero was applied to the bottom of the armature to force the current to exit through the armature.

Because the temperature concentration was expected to occur at the interface, a fine mesh density was used there as evidenced in Figure 43.

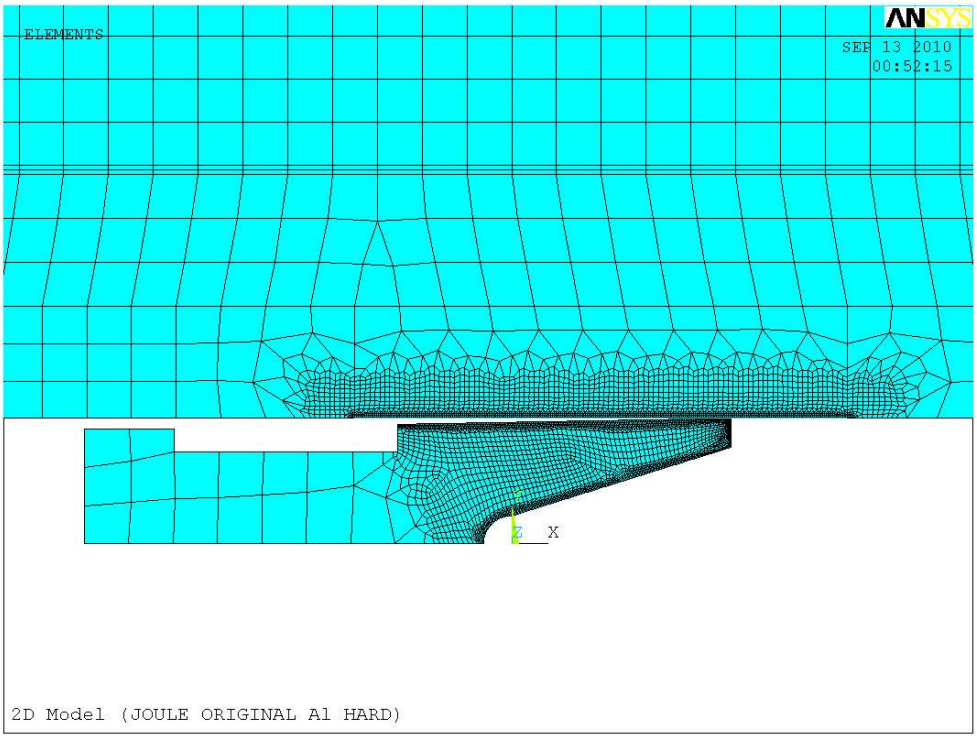

Figure 43. Mesh plot of the Joule heating FEA model for the original aluminum design with a hard compliance layer

A contact pair was applied at the contact interface using CONTACT 172 and TARGET 169 from Figure 19, which was where the TCC and ECC values estimated in the previous section, were input. The ambient temperature was set to 293°K with convection applied to the front of the armature and all the way around the outer edge of the rail system with a convective coefficient of 15 W/m-°K.

The element used in the analysis was Plane 67 shown in Figure 44, which has thermal and electrical conduction capabilities. The element has four nodes with temperature and voltage as its degrees of freedom at each node.

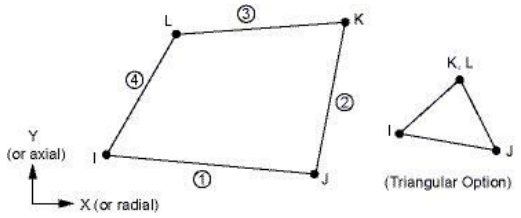

Figure 44. Diagram of the Plane 67 element [29]

5.3.2. Results and Discussion

As expected the high current concentration in the small contact area causes the temperatures to be extremely high. The results for the maximum temperatures reach values that are known to be unrealistically high and are acknowledged to be a limitation on the FEA model. Therefore, the time at which melting occurs due to Joule heating alone, and not the highest temperature that occurred in the transient simulation, was found.

5.3.2.1 Design Comparison

Again, to compare the designs to each other the Joule heating analysis is completed for both aluminum designs and compliance layers at the lab-scale half-interference. The results are summarized in Table 13.

Table 13. Times at which melting occurs from Joule heating for the original and modified designs with the hard and soft compliances at the lab-scale half-interference

	Melt Time (μs)	**Rank**
Original Hard	5.14	3
Original Soft	3.21	4
Modified Hard	47.4	1
Modified Soft	32.7	2

Between designs, the modified design is an improvement over the original design as it allows for a higher time before melting. There was a 922% and 1019% increase between the designs for the hard and soft compliance layers, respectively. More specifically, as with the melt-wear velocity, the modified design with the hard compliance layer results with a higher melting time making it the best choice. The worst choice is the original design with the soft compliance layer. The reason for the expected lower melting time than the original design with the hard compliance layer is that the contact length was smaller for the original design with the soft compliance layer. Therefore, there was less area for the heat to dissipate through. Also, between compliance layers, the best choice was the harder compliance layer. This was, again, due to the contact area.

Figure 45 and Figure 46 shows the thermal distribution at the armature-to-rail contact at a time of t = 25 μs with the loading conditions from the initial contact only. As shown in Figure 45 and Figure 46, the maximum temperature occurs closer to the leading edge of the armature for all designs and compliance layers. It is expected that this occurred because the material resistance is low relative to the contact resistance. Thus, the current is traveling further along the rail before it transfers through the contact resistance into the armature. It should be noted that cell death was not used in these simulations so temperatures rose above melting temperatures for materials.

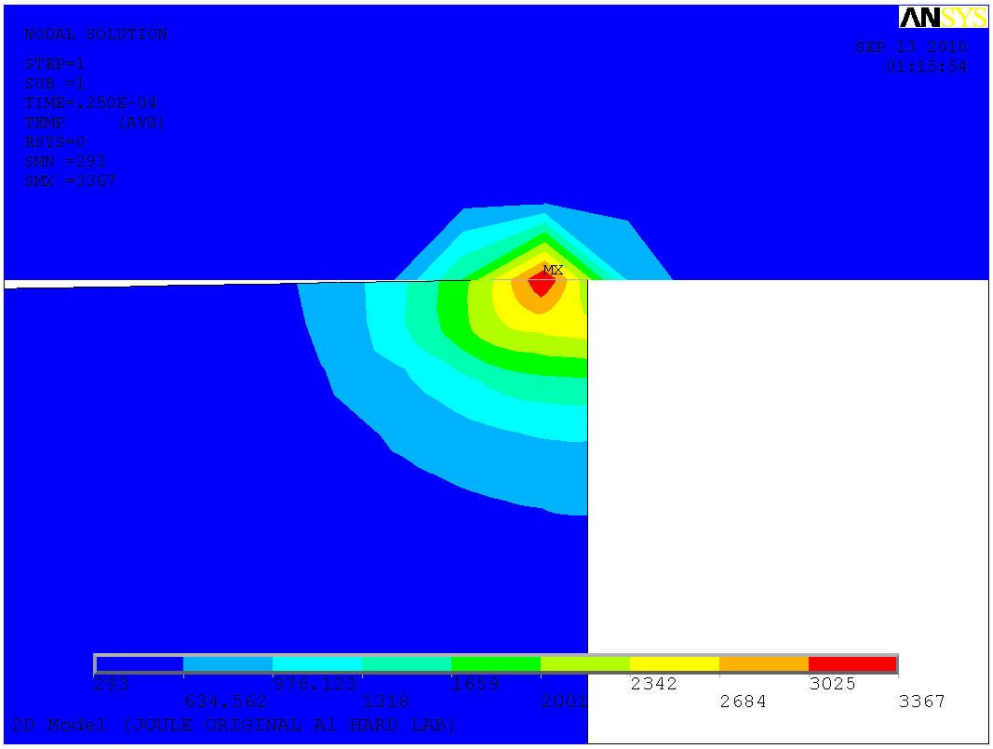

a)

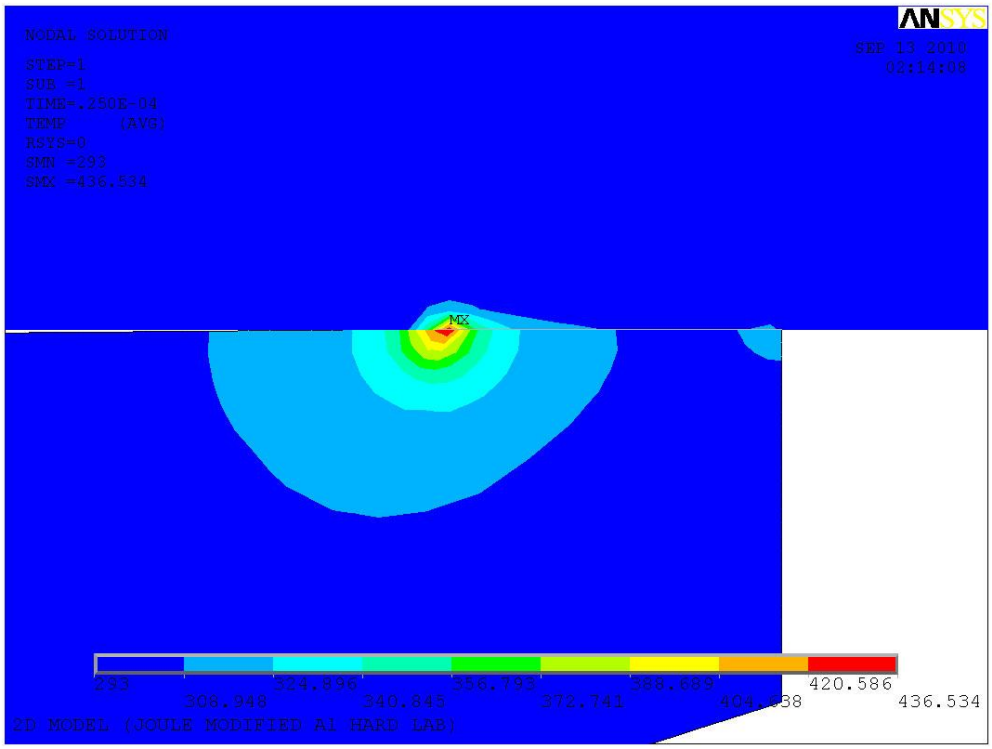

b)

Figure 45. The thermal distribution at a half-interference of 0.1232 mm for the a) original and modified b) designs with the hard compliance layer at a time of 25 μs

a)

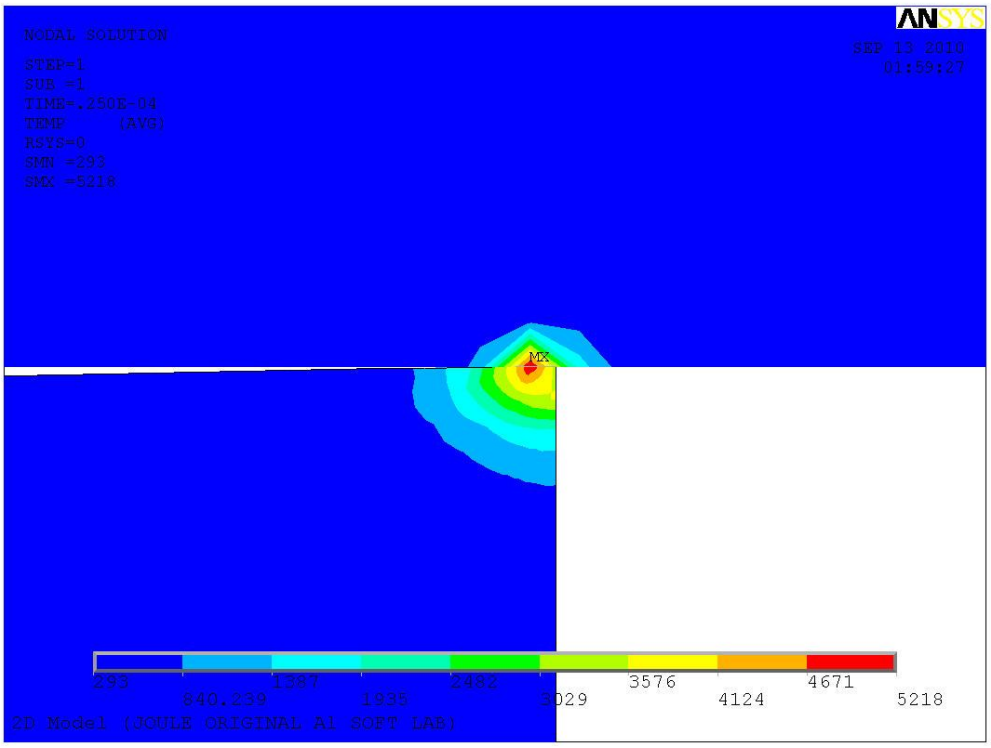

b)

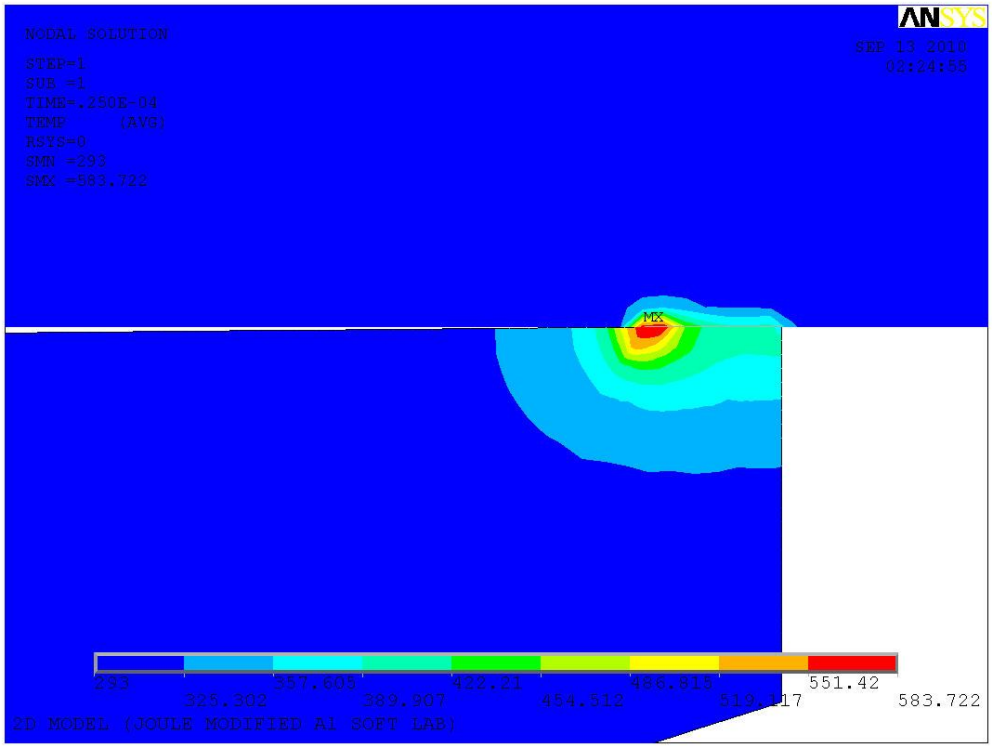

Figure 46. The thermal distribution at a half-interference of 0.1232 mm for the a) original and modified b) designs with the soft compliance layer at a time of 25 μs

5.3.2.2. Material Comparison

Table 14 shows the time at which melting occurs by Joule heating at the maximum contact pressure criterion interference that was solved for in the structural analysis.

Table 14. Times at which melting occurs from Joule heating for the original and modified designs with the a) hard and b) soft compliances at the maximum contact pressure criterion interference

a)

Armature Material	**Original Design**		**Modified Design**	
	Melt Time (μs)	***Rank***	***Melt Time (μs)***	***Rank***
Aluminum	4.64	5	2.42	5
Molybdenum	16.4	2	17.8	2
Niobium	9.35	4	2.97	4
Tantalum	15.3	3	14.7	3
Titanium	1.06	6	0.574	6
Tungsten	32.7	1	28.2	1

b)

Armature Material	**Original Design**		**Modified Design**	
	Melt Time (μs)	***Rank***	***Melt Time (μs)***	***Rank***
Aluminum	4.05	6	23.9	5
Molybdenum	48.0	2	49.7	2
Niobium	25.4	4	25.2	4
Tantalum	29.3	3	28.3	3
Titanium	8.05	5	3.76	6
Tungsten	94.6	1	56.7	1

When comparing materials tungsten was the optimal choice as it allowed for more time to pass before melting occurred for all designs and compliance layers. As with the melt-wear velocities, in all cases, titanium was the poorest choice in material. In general, the soft compliance layer was the optimal choice over the hard compliance layer. There was no determinable difference between the designs.

From Table 14, the best overall choice was the tungsten armature with an original design and soft compliance layer as it allowed for a melt time of t = 94.6 μs. The worst choice was titanium with a modified design and hard compliance layer with a melt time of t = 0.574 μs.

As stated before, it was previously determined that Joule heating would be the most important factor in melting. Therefore, the materials were ranked according to the results of the Joule heating analysis and those results are shown in Table 15. The results are an average ranking of the hard and soft compliance layer but the designs are ranked separately. Between the compliance layers and the designs, the results were generally consistent. However, it should be noted that tungsten is consistently the best material choice, while titanium is the poorest choice.

Table 15. Ranking of the materials based on the Joule heating analysis

Armature Material	**Original Design**	**Modified Design**
	Rank	***Rank***
Aluminum	5	5
Molybdenum	2	2
Niobium	4	4
Tantalum	3	3
Titanium	6	6
Tungsten	1	1

The following is a summary of results from the frictional and Joule heating analysis:

1. For friction heating, by calculating the velocity at which melting occurs, the optimal choice was the tungsten armature with a modified design and hard compliance layer. The melt-wear velocity that it could accomplish was V_m = 5478 m/s.

2. For Joule heating, by estimated the melting time using the current curve used on the current lab-scale EML, the optimal choice was the tungsten armature with an original design and soft compliance layer. The melt time was t = 94.6 μs.
3. For all cases in both analyses, titanium was the poorest material choice, while tungsten was the best.

CHAPTER 6: MODAL ANALYSIS

The focus of this chapter is on the vibration characteristics of the armature. The analysis determines the natural frequencies and mode shapes of free vibration and for a pre-stressed armature. The analysis is completed for the all the armature designs and material choices. For the pre-stressed armature, the analysis is performed for both designs, all material choices, and both compliance layers using the maximum contact pressure criterion from the structural analysis. The importance of the vibration characteristics is the behavior of the armature as it travels through the launcher. Constant contact between armature legs and rail is desired for constant current flow, but the magnitude of the mode shape can cause intermittent contact at the interface.

6.1. Vibration of the Armature without Pre-stress Conditions

A modal analysis was conducted on the armature without any added forces to determine the free vibration characteristics of the armature designs and materials.

6.1.1. Geometry, Meshing, Boundary Conditions, and Element

Figure 47 shows a 3-D plot of the meshed original armature design used in this analysis. Because it is free vibration, there are no boundary conditions applied to the model.

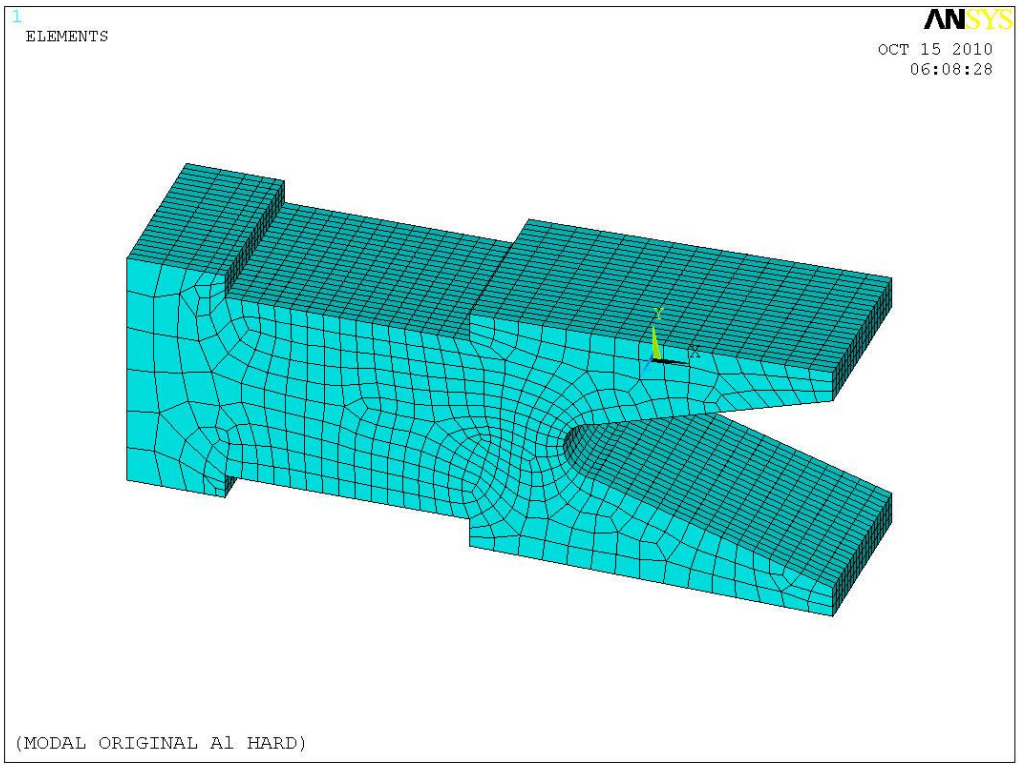

Figure 47. 3-D plot of the meshed original armature design used in the free vibration analysis

The element type used was the Solid 45 element which is an 8 node 3-D element with 3 degrees of freedom at each node: translations in the x-, y-, and z-directions. Figure 48 shows the schematic diagram of the Solid 45 element used in the analysis.

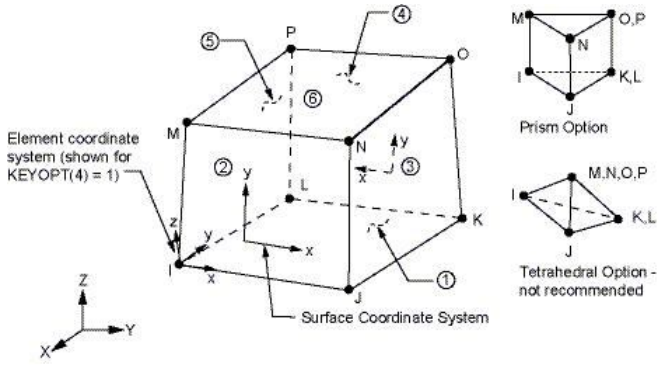

Figure 48. Diagram of the Solid 45 element [29]

6.1.2. Results and Discussion

The first six results of the modal analysis were six rigid body motions. The rigid body motions are translations in the x-, y-, and z-axes and rotations along the x-, y-, and z-axes. The six rigid body motions are shown in Figure 49.

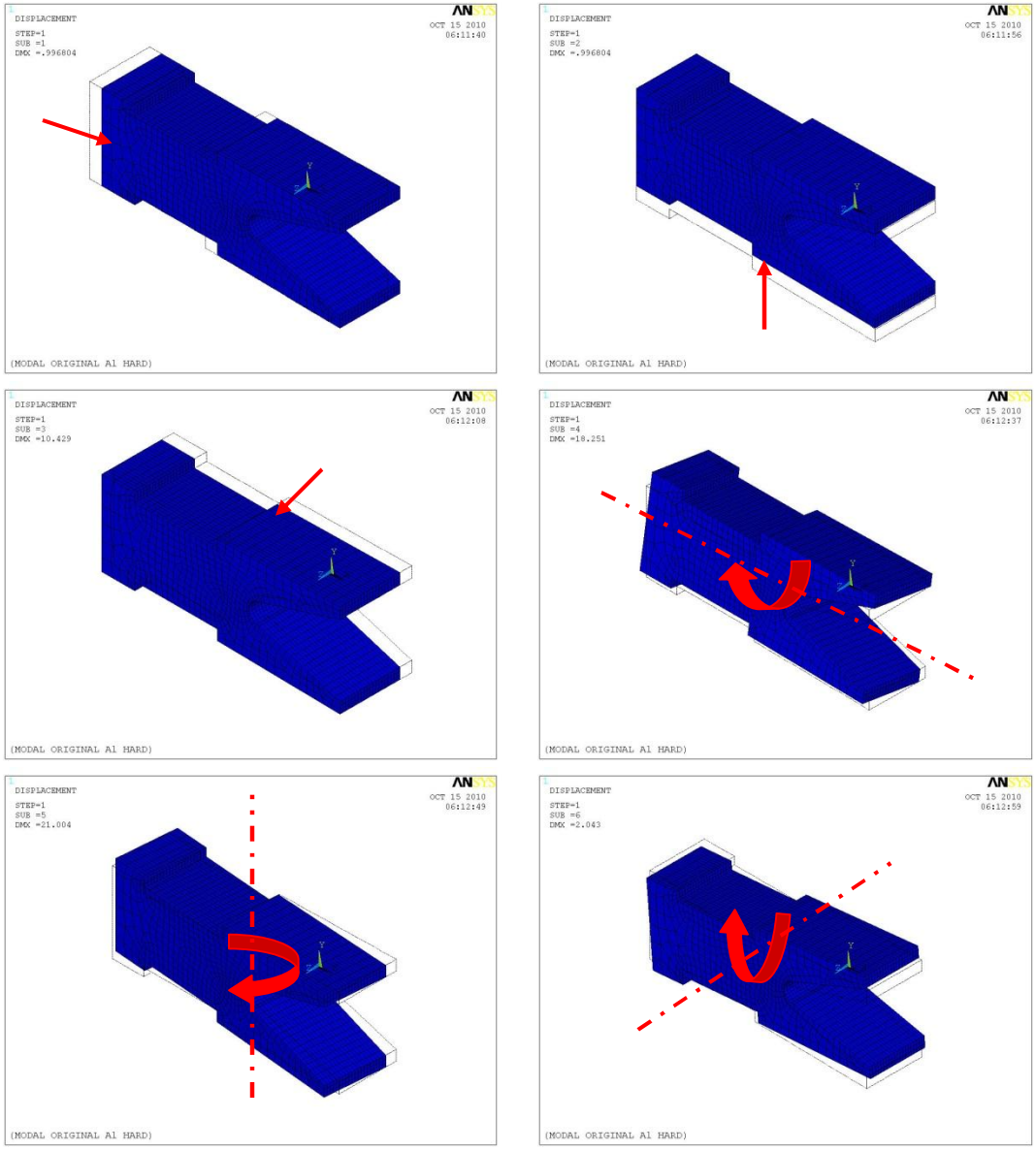

Figure 49. Six rigid body motions of the original aluminum armature

The first four mode shapes were found as well as the frequencies at which they occurred. Figure 50 shows the first mode shapes found using ANSYS for the aluminum

armature of the original design. Table 16 shows the periods for the first four mode shapes that were shown in Figure 50.

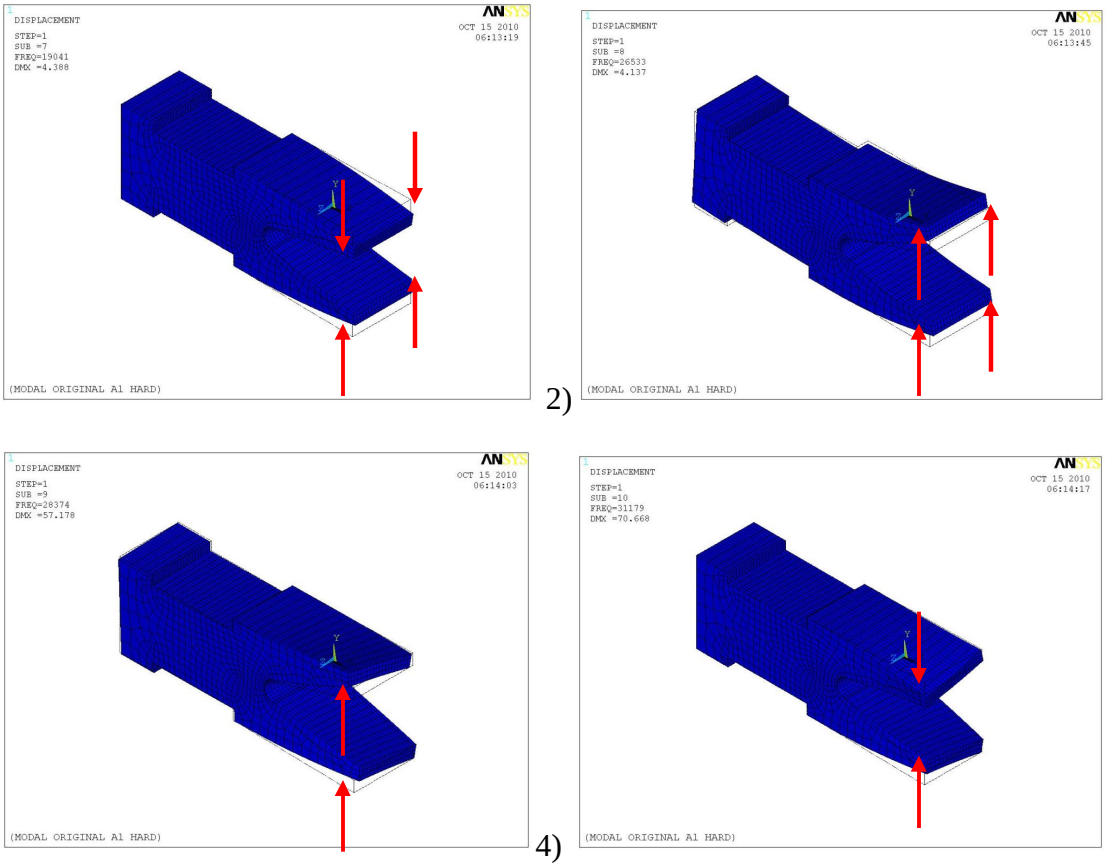

Figure 50. First four vibration mode shapes of the original aluminum armature

Table 16. Periods of first four vibration mode shapes for both armature designs and materials

Armature Material	Period of the Original Design (μs)				Period of the Modified Design (μs)			
	Mode Shape 1	*Mode Shape 2*	*Mode Shape 3*	*Mode Shape 4*	*Mode Shape 1*	*Mode Shape 2*	*Mode Shape 3*	*Mode Shape 4*
Aluminum	52.52	37.69	35.24	32.07	51.83	37.25	34.93	31.60
Molybdenum	46.68	33.52	31.54	28.63	46.07	33.13	31.26	28.22
Niobium	76.61	55.11	52.77	47.58	75.61	54.47	52.32	46.89
Tantalum	79.34	57.02	54.13	48.98	78.31	56.36	53.66	48.26
Titanium	52.24	37.53	35.52	32.18	51.56	37.09	35.21	31.71
Tungsten	58.29	41.80	38.85	35.43	57.53	41.32	38.51	34.91

6.1.2.1. Design Comparison

Between the designs, as expected, there was not much of a difference in the periods because the shape of the armature did not change significantly. For each material, the original design had a higher period than the modified design. The most significant

mode shape is the first mode shape. The legs flexing out-of-phase towards each other is an undesired displacement because it can lead to loss of contact between the armature and rails. The second mode shape is an in-phase motion of the legs moving towards the rails. The third mode shape is an in-phase rotation about the long axis of the armature, while the fourth mode shape is an out-of-phase motion moving transversely to the rails.

6.1.2.2. Material Comparison

The periods of the armature with respect to the material choice vary depending on the materials as shown in Table 16. The material of the original design armature with the longest period of 79.34 μs was tantalum while titanium had the shortest period of 52.24 μs. For the modified design tantalum had the longest period of 78.31 μs while titanium had the shortest period of 51.56 μs. However, since the expected exit time of the armature from the barrel is longer than the period, intermittent contact is still possible for all materials and designs.

6.2. Vibration of the Armature with Pre-stress Conditions

In the EML the armature is placed under an interference load as shown in the structural chapter of this paper. This section completes a modal analysis of the original and modified designs of the armature for each material. The analysis is completed for the original and modified design of the aluminum armature at the lab-scale interference using a pre-stress model of the hard and soft compliance layer. The analysis is then done for both designs, both compliance layers, and all materials using the maximum contact pressure criterion force load.

6.2.1. Geometry, Meshing, Boundary Conditions, and Element

The same 3-D model used in the free vibration analysis is employed for the pre-stressed model. However, in order to pre-stress the armature, a force is applied along the edge of the legs of the armature as shown in Figure 51. These forces are applied to estimate the load the armature receives from the interference of the rails. The magnitude of the forces applied to the legs is derived from the structural analysis at the lab-scale interference and the maximum contact pressure criterion interference. The same element is used in this analysis as well.

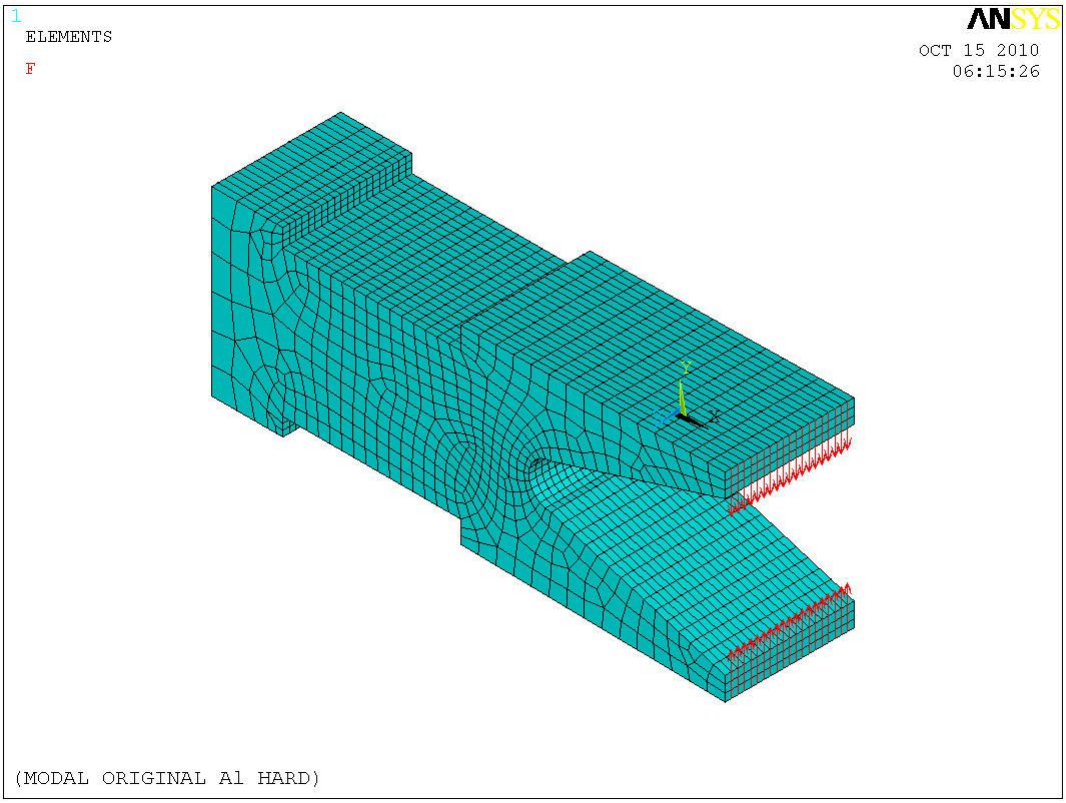

Figure 51. 3-D plot of the meshed original armature design used in the pre-stress modal analysis with a force boundary condition

6.2.2. Results and Discussion

The first portion of this section will compare the original design to the modified design for each compliance layer using the force from the lab-scale interference analysis and aluminum as the armature material. The following portion then compares the materials to each other by using the forces from the maximum pressure criterion interference analyses.

6.2.2.1. Design Comparison

As before, the first six results of each analysis were the rigid body motions. They were translations along the x-, y-, and z- axes and rotations along those same axes. After the six rigid body motions, the four vibration modes and their periods were found. The mode shapes were the same as the unstressed mode shapes as shown in Figure 52.

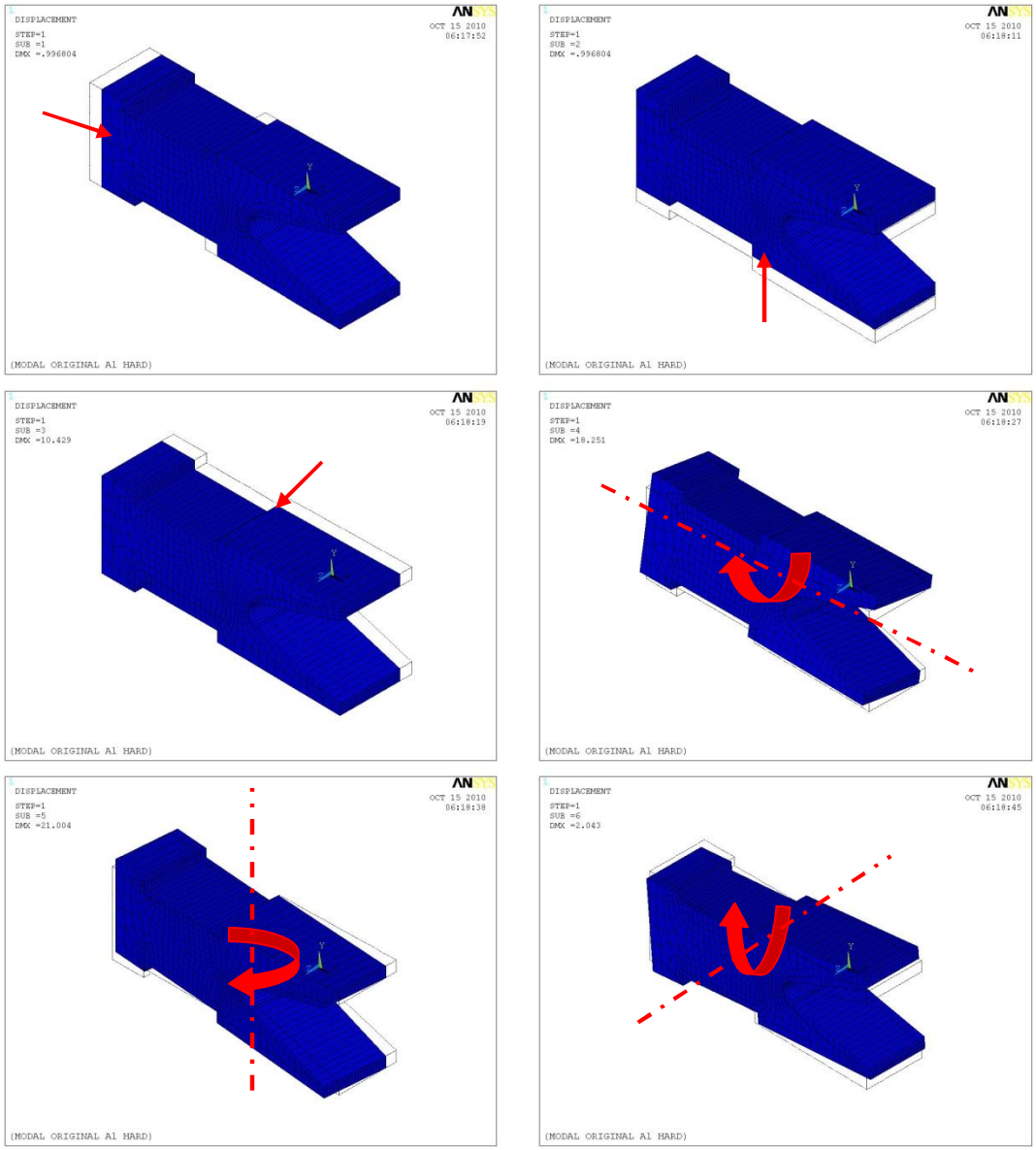

Figure 52. First six vibration mode shapes of the original aluminum armature with hard compliance layer under the lab-scale interference pre-stress conditions

Table 17 summarizes the periods of the first four vibration mode shapes for the original and modified aluminum designs with the hard and soft compliance layers at the lab-scale interference.

Table 17. Periods of first four vibration mode shapes for the original and modified design with the hard and soft compliance layer using the lab-scale interference pre-stress conditions

Aluminum	**Period (μs)**			
	Mode Shape 1	*Mode Shape 2*	*Mode Shape 3*	*Mode Shape 4*
Hard Original	52.52	37.69	35.25	32.09
Hard Modified	51.83	37.25	34.94	31.62
Soft Original	52.52	37.69	35.25	32.08
Soft Modified	51.83	37.25	34.94	31.61

The first vibration mode shape is the out-of-phase displacement of the legs towards each other. The second mode shape is an in-phase motion of the legs moving towards the rails. The third mode shape is an in-phase rotation about the long axis of the armature. Finally, the fourth mode shape is an out-of-phase motion moving transversely to the rails. These results are consistent with the previous model results without the pre-stress condition. Also, the periods do not vary much between the model without the pre-stress and with the pre-stress. This is expected because the amount of force required to displace the legs, is not very large and, therefore, not expected to change the periods very much. Also, intermittent contact is a possibility because the period of the first vibration mode shape is much shorter than the exit time calculated from the EMAG analysis.

6.2.2.2. Material Comparison

The first six results were, again, the same rigid body motions as the aluminum armature for all materials, designs, and compliance layers. The same vibration mode shapes as the previous results then follows for the next 4 mode shapes. The results are summarized in Table 18.

Table 18. Periods of first four vibration mode shapes for the original and modified design with the a) hard and b) soft compliance layer using the maximum contact pressure criterion interference pre-stress conditions

a)

Armature Material	Period of the Original Design (μs)				Period of the Modified Design (μs)			
	Mode Shape 1	*Mode Shape 2*	*Mode Shape 3*	*Mode Shape 4*	*Mode Shape 1*	*Mode Shape 2*	*Mode Shape 3*	*Mode Shape 4*
Aluminum	52.52	37.69	35.24	32.07	51.83	37.25	34.93	31.60
Molybdenum	46.68	33.52	31.54	28.63	46.07	33.13	31.26	28.22
Niobium	76.61	55.11	52.77	47.58	75.61	54.47	52.32	46.89
Tantalum	79.34	57.02	54.13	48.98	78.31	56.36	53.66	48.26
Titanium	52.24	37.53	35.52	32.18	51.56	37.09	35.21	31.71
Tungsten	58.29	41.80	38.85	35.43	57.53	41.32	38.51	34.91

b)

Armature Material	Period of the Original Design (μs)				Period of the Modified Design (μs)			
	Mode Shape 1	*Mode Shape 2*	*Mode Shape 3*	*Mode Shape 4*	*Mode Shape 1*	*Mode Shape 2*	*Mode Shape 3*	*Mode Shape 4*
Aluminum	52.52	37.69	35.25	32.09	51.83	37.25	34.94	31.61
Molybdenum	46.68	33.52	31.54	28.65	46.07	33.13	31.26	28.22
Niobium	76.61	55.11	52.78	47.59	75.61	54.47	52.32	46.90
Tantalum	79.35	57.02	54.14	49.00	78.31	56.36	53.66	48.26
Titanium	52.24	37.53	35.53	32.18	51.56	37.09	35.22	31.72
Tungsten	58.29	41.80	38.86	35.45	57.53	41.32	38.51	34.92

As shown in Table 18, the periods are very similar to the results of the model without the pre-stress condition. Again, this is expected to occur because the force required to create the pre-stress condition is not very high. Intermittent contact would be expected in all of these scenarios as well.

The following is a summary of results from the modal analysis:

1. The periods of the armatures are much smaller than any exit time calculated in the EMAG analysis. Therefore, intermittent contact is a possibility.
2. Between designs, the periods differed from each other but not by a significant amount relative to the exit times of the armatures.
3. There was not a significant different between the analysis without the pre-stress and the models with the pre-stress.

CHAPTER 7: CONCLUSIONS AND FUTURE WORK

This section presents the results and conclusions obtained from the different cases studied. It also proposes potential future areas of study with regard to the EML and wear reduction.

7.1. Conclusions

Using FEA, different aspects of the EML were studied to better understand the influences of melt-wear. By varying the different parameters of the current lab-scale EML design, more options can be considered when optimizing the EML.

7.1.1. Structural Analysis

The structural analysis takes displacement of the rails as an input and calculates the von Mises stresses, contact pressure, and contact area as an interference is created with the armature. It also takes into account a compliance layer which simulates any stiffness in the EML system. For the structural analysis, the armature material, compliance layer stiffness, and armature design is varied.

From the analysis, the magnitude of the maximum von Mises stress for both models and compliance layers did not reach the yield strength of aluminum at the lab-scale half-interference, or for either compliance layer. When comparing designs, either is acceptable because neither design for both compliance layers yielded before the lab-scale half-interference. The contact pressure for the original design and both compliance layers is ~4.5 MPa while it was ~1 MPa for the modified design and both compliance layers. Between compliance layers, the softer compliance layer gave lower von Mises stresses at the bend than the harder compliance layer. However, for the contact von Mises stresses, it

was the opposite case. The maximum contact pressure criterion described in the structural section gives vital information, such as the contact length, to be used in later analyses.

7.1.2. Electromagnetic Analysis

The electromagnetic analysis determines the EMAG forces experienced by the armature due to the lab-scale experimental current curve. Using the current curve as an input, the EMAG forces are calculated in the x-, y-, and z-directions of the armature for the two armature designs (original and modified) and two armature materials (aluminum and molybdenum). Also, using the EMAG forces, an exit time from the launcher is estimated for each design and material.

The analysis showed that the forces in the x-direction are higher for the original aluminum armature than the forces experienced by the modified design, which is likely due to the slightly increased volume of the modified design. The difference in force, causes an estimated exit time of $t = 0.9099$ ms for the original design armature and $t = 0.9418$ ms for the modified design armature. Between materials, there is not a significant difference in the forces. The maximum speed approximated by the results and calculations is approximately 2500 m/s which is similar to lab-scale results. Also, the friction forces that would occur at the lab-scale interference are very low compared to the EMAG forces the armature experiences.

7.1.3. Thermal Analysis

The thermal analysis focuses on frictional heating and Joule heating. For frictional heating, an equation is used to estimate the velocity obtainable at the melting point based solely on friction. For Joule heating, the armature is stationary and the current is used as an input to calculate the rise in temperature of the system.

Based on the friction heating calculations and inputs used from the contact pressure criterion of the structural analysis, the optimal choice was the tungsten armature with a modified design and hard compliance layer. The velocity estimated that could be reached was $V_m = 5478$ m/s. For Joule heating, based on estimated melting times, the optimal choice was the tungsten armature with an original design and soft compliance layer. The melting time estimated was $t = 94.6$ μs. For all cases in both analyses, titanium was the poorest choice.

7.1.4. Modal Analysis

The modal analysis finds the vibration periods and mode shapes. This helps determine if intermittent contact can occur before the armature leaves the barrel of the EML. The analyses performed were for all materials, both designs, and both compliance layers. Also, the model could use an unstressed condition and a pre-stressed condition. The pre-stress inputs were based on the structural contact pressure criterion and lab-scale interference data.

Based on the exit times calculated in the EMAG analysis and the periods from the modal analysis, intermittent contact is a possibility. Between designs, the periods did not differ significantly relative to the exit times of the armatures. There was also not a significant difference between the unstressed condition and pre-stress conditioned.

7.2 Discussion and Future Work

While the FEA program, ANSYS, is very powerful, there are many intricacies that need to be understood to run the simulations. Without a firm grasp of those details, many errors can be introduced into the simulations which greatly affect the end results.

However, once the details are understood, the program can be used to calculate

many important factors with regards to melt-wear in the EML. Using the program, contact area between the armature and rail can be optimized to potentially reduce current crowding by creating more area for the current to travel though thus reducing maximum temperatures. Another possibility is to compare material properties to see the varying effects on EMAG forces or Joule heating.

The analyses completed in this work were all uncoupled. However, the program has coupling capabilities. Future work can focus on coupling the results more. For example, instead of estimating contact length and pressures at the end of the structural analysis and using those as inputs for a separate thermal analysis, having a two step analysis. The first analysis would create the interference followed by an analysis that accounted for Joule heating. Using a coupled analysis can be more computing time intensive but can possibly account for thermal dependent properties.

Another possibility for coupled analysis is using an EMAG analysis that accounts for friction and Joule heating as the armature moves and the current is input. This would give a more accurate description of the temperature and displacement profile of the armature.

From this work, it was found that tungsten had a high melt-wear velocity as well as time at melting. Using this knowledge and the fact that tungsten is a very dense metal, different armature designs can be proposed. For example, using an aluminum body armature with a layer of tungsten on the legs at the contact point between the armature and rail. This allows the armature to remain lighter than a solid body tungsten armature, while maintaining its potentially higher melt resistant capabilities.

In this study, the only material that was varied was the armature. However, different alloys can be used for the armature or focus can be given to the rails. Also, the melted material was not taken into account during this analysis. Melted material can be examined in future work by using the birth and death feature of ANSYS. Modeling melted material can be incorporated into the coupled analyses described above.

APPENDIX A

MATERIAL PROPERTIES

Material	Density (kg/m^3)	Hardness (Gpa)	Yield Strength (Mpa)	Resistivity (Ω-m)	Heat Capacity (J/kg-°C)	Thermal Conductivity (W/m-°K)	Modulus of Elasticity (Gpa)	Poissons Ratio	Melting Temp (°K)
Aluminum (6061-T6)	2700	1.049	276	4.00E-08	896	167	68.9	0.33	925
Molybdenum (stress relieved)	10220	2.256	415	5.70E-08	255	138	330	0.32	2883
Niobium (wrought)	8600	1.569	207	1.51E-07	272	52.3	103	0.38	2741
Tantalum (annealed)	16650	0.981	170	1.25E-07	153	54.4	186	0.35	3269
Titanium	4500	0.588	140	5.54E-07	528	17	116	0.34	1941
Tungsten	19300	3.040	750	5.65E-08	134	163.3	400	0.28	3695
Copper (C110 H08)	8900	0.961	217	1.71E-08	385	387	122.5	0.31	1356
g10	1500			6.00E+10	2500	0.288	18.6	0.1	
Mylar	1400			1.00E-01	1	1	4	0.1	
Stainless Steel (UNS S30100)	8030			7.20E-05	500	16.3	185	0.31	

REFERENCES

1. Bolonkin, A. and M. Krinker, *Railgun Space Launcher.* Journal of Aerospace Engineering, 2010. **23**(4): p. 293-299.
2. Wetz, D., et al., *Electromagnetic Launch to Space.* Acta Physica Polonica A, 2009. **115**(6): p. 1066-1068.
3. Merrill, R. and F. Stefani, *Electrodynamics of the Current Melt-Wave Erosion Boundary in a Conducting Half-Space.* IEEE Transactions on Magnetics, 2003. **39**(1): p. 66-71.
4. Stefani, F. and J.V. Parker, *Experiments to Measure Wear in Aluminum Armatures.* IEEE Transactions on Magnetics, 1999. **35**(1): p. 100-106.
5. Watt, T. and F. Stefani, *The Effect of Current and Speed on Perimeter Erosion in Recovered Armatures.* IEEE Transactions on Magnetics, 2005. **41**(1): p. 448-452.
6. Marco Angeli, E.C., *Electro-Thermal Behavior of Solid Armatures.* IEEE Transactions on Magnetics, 1999. **35**(1): p. 47-52.
7. E.M. Drobyshevskii, E.N.K., V.S. Yuferev, *Thermoelectrodynamic Loss of Material by a Solid Armature in a Railgun as a Cause of Velocity Limitation.* Technical Physics Letters, 1999. **25**(4): p. 260-262.
8. Dutta, I., et al., *Electric-Current-Induced Liquid Al Deposition, Reaction, and Flow on Cu Rails at Rail-Armature Contacts in Railguns.* IEEE Transactions on Magnetics, 2009. **45**(1): p. 272-277.
9. He, L. and T.C. Ovaert, *Heat Partitioning Coefficient for Sliding Contacts with Friction.* Tribology Transactions, 2008. **51**(1): p. 12-18.
10. T. Chen, X.L., I. Dutta, C. Persad, *Effect of Current Crowding on Microstructural Evolution at Rail-Armature Contacts in Railguns.* IEEE Transactions on Magnetics, 2007. **43**(7): p. 3278-3286.
11. Laura Rip, S.S., Kuo-Ta Hsieh, *Effect of Geometry Change on teh Current Density Distribution in C-Shaped Armatures.* IEEE Transactions on Magnetics, 2003. **39**(1): p. 72-75.
12. Sikhanda Satapathy, T.W., Chadee Persad, *Effect of Geometry Change on Armature Behavior.* IEEE Transactions on Magnetics, 2007. **43**(1): p. 408-412.
13. James, T., *Why Solid Armatures Fail and How They can be Improved.* IEEE Transactions on Magnetics, 2003. **39**(1): p. 56-61.
14. James, T., *A Transitioning Hybrid Armature Concept.* IEEE Transactions on Magnetics, 2001. **37**(1): p. 77-80.
15. Merrill, R. and F. Stefani, *A Turbulent Melt-Lubrication Model of Surface Wear in Railgun Armatures.* IEEE Transactions on Magnetics, 2005. **41**(1): p. 414-419.
16. Ghassemi, M. and Y.M. Barsi, *Effect of Liquid Film (Indium) on Thermal and Electromagnetic Distribution of an Electromagnetic Launcher With a New Armature.* IEEE Transactions on Magnetics, 2005. **41**(1): p. 408-413.
17. Irwin Singer, M.V., Craig Boyer, Jesse Neri, *Wear Behavior of Lubricant-Conditioned Copper Rails and Armatures in a Railgun.* IEEE Transactions on Magnetics, 2010. **38**(10).

18. Watt, T., et al., *Investigation of Damage to Solid-Armature Railguns at Startup.* IEEE Transactions on Magnetics, 2007. **43**(1): p. 214-218.
19. Watt, T. and S. Fish, *Examination of High Frequency Contact Chatter in Trailing Arm Armatures.* IEEE Transactions on Magnetics, 2001. **37**(1): p. 106-110.
20. Hopkins, D., et al., *Analysis of Startup Behavior in a "C-Shaped" Armature Using Linked EMAP3D/DYNA3D Finite Element Codes.* IEEE Transactions on Magnetics, 1999. **35**(1): p. 59-64.
21. Newill, J., J. Powell, and A. Zielinski, *Coupled Finite-Element Codes for Armature Design.* IEEE Transactions on Magnetics, 2003. **39**(1): p. 148-152.
22. Liu, H.-P. and M.C. Lewis, *3-D Electromagnetic Analysis of Armatures and Rails for High Launch Energy Applications.* IEEE Transactions on Magnetics, 2009. **45**(1): p. 322-326.
23. Stankevich, S.V. and G.A. Shvetsov, *Effect of the Shape of Metal Solids on the Rate of Their Joule Heating in Electromagnetic Rail Launchers.* Journal of Applied Mechanics and Technical Physics, 2009. **50**(2): p. 342-351.
24. Powell, J.D. and A.E. Zielinski, *Ohmic Heating in a Double-Taper Sabot-Armature.* IEEE Transactions on Magnetics, 2003. **39**(1): p. 153-157.
25. Watt, T.J. and M.D. Bryant, *Cracking and Dominant Stresses in the Throat Region of C-Shaped Solid Armatures.* IEEE Transactions on Magnetics, 2007. **43**(1): p. 418-421.
26. Hsieh, K.T., S. Satapathy, and M.T. Hsieh, *Effects of Pressure-Dependent Contact Resistivity on Contact Interfacial Conditions.* IEEE Transactions on Magnetics, 2009. **45**(1): p. 313-318.
27. Merrill, R., F. Stefani, and T. Watt, *Magnetic Repulsive Forces on Armature Contacts.* IEEE Transactions on Magnetics, 2007. **43**(1): p. 384-387.
28. Chung, B., *Finite-Element Analysis of Physical Phenomena of a Lab-Scale Electromagnetic Launcher (MS Thesis)*, in *Mechanical Engineering*. 2007, Georgia Institute of Technology: Atlanta.
29. ANSYS, I., *ANSYS Release 9.0 Documentation*. 2004.
30. C.L. Yeh, C.T.L., *Thermal Contact Resistance Correlation for Metals Across Bolted Joints.* Int. Comm. Heat Masst Transfer, 2003. **30**(7): p. 987-996.
31. McGill, D.J. and W.W. King, *An Introduction to Dynamics*. Fourth ed. 2003, Bloomington: Tichenor Publishing.
32. Bansal, D. and J. Streator, *Transitions in Contact Resistance Between a Pin and Flat During Sliding at High Current Densities.* Proceedings of STLE/ASME International Joint Tribology Conference, 2006.
33. Incropera, F.P. and D.P. DeWitt, *Fundamentals of Heat and Mass Transfer*. 5 ed. 2002: John Wiley & Sons Inc.
34. Jaegar, J.C., *Moving Sources of Heaet and the Temperature at Sliding Contacts.* J of the Royal Society of New South Wales, 1942. **76**: p. 203.224.